Measurement of the two photon exchange asymmetry in the quasielastic scattering of transversely polarized electrons off unpolarized deuterium

Diploma thesis by David Balaguer Ríos
born in 1979 in Valencia (Spain)

Contents

Introduction

The A4 collaboration carries out a program of measurements of the beam transverse spin asymmetry in the electron-nucleon scattering. A beam of electrons is polarized transversely to the direction of the beam. The electrons are scattered off a nucleon target and counted by a Cherenkov-detector. The asymmetry is calculated from the count rates for both opposite polarization states. The transverse spin asymmetry allows the access to the imaginary part of the two photon exchange amplitude of the electromagnetic elastic scattering process. The A4 collaboration has already measured and published the transverse spin asymmetries at two different momentum transfers $Q^2 = 0.106$ (GeV/c)^2 and $Q^2 = 0.230$ (GeV/c)^2 at forward scattering angles $30° < \theta_e < 40°$ using liquid hydrogen as target [1]. The two photon exchange amplitude is of special interest because it might explain the discrepancies observed between different methods of determination of the electromagnetic nucleon form factors. The measurements show that excited intermediate hadronic states contribute substantially to the asymmetry.

Recently the detector has been rearranged to operate at backward scattering angles, $140° < \theta_e < 150°$. Measurements of the transverse spin asymmetry have been performed for the momentum transfer $Q^2 = 0.230$ (GeV/c)^2 on both liquid hydrogen ℓH_2 and liquid deuterium ℓD_2 targets. The focus of this works lies on the deuterium data. The measured observable is the asymmetry in the cross section of the quasielastic scattering of transversely polarized electrons off unpolarized deuterium. The deuterium is the natural target to access information about the structure of the neutron since in the quasielastic scattering both nucleons behave as quasifree particles. Nevertheless the nuclear binding of both nucleons still represents a problem both in the theory framework and in the experimental realization. In the theory the problems arise from the nuclear model dependencies to extract information about the neutron from the deuterium data. From the experimental point of view the Fermi motion of the nucleons inside the deuteron make the quasielastic peak in the energy spectrum broader than the elastic electron-proton scattering peak. This makes the separation of the quasielastic peak from the experimentally observed spectra more complicated.

The second chapter gives an overview of the discussions about the two pho-

ton exchange and about the model calculation that provides results for both the transverse spin asymmetry on proton and neutron. Then in the third chapter we say some words about the different nuclear models of the deuteron used to explain the scattering process. Actually the nuclear model calculation have been applied to the parity violating asymmetry but not yet to the transverse spin asymmetry related to the two photon exchange.

The fourth chapter presents an overview of the experimental set up of the A4 collaboration and of the MAMI accelerator facility. We focus on the aspects relevant to the measurement of the asymmetry and on the characteristics of the A4 detector at backward angles.

The fifth chapter presents the data measured with the PbF_2 calorimeter for the deuterium and compares them with the data corresponding to the hydrogen measurements. The procedure to extract the quasielastic events from the experimentally observed energy spectra of all recorded events is discussed.

The sixth chapter is devoted to the extraction of the asymmetry from the data. The main topics of the data analysis are:

- The procedure to optimize the determination of the asymmetry from the experimentally observed energy spectra. This optimization is necessary because the quasielastic events are mixed with neutral background processes that are not completely separated by the detector and present a different physical asymmetry. The procedure makes use of Monte Carlo simulations that were performed for the actual experimental set up.

- The correction of the instrumental asymmetries arising from helicity correlated beam fluctuations by means of a multilinear regression method.

In the seventh chapter we present the results for the asymmetry in the signal, applying the methods introduced in the chapter six, and we apply them also to extract the asymmetry in the background. Finally in the chapter eighth the multilinear regression method is applied to obtain the transverse spin asymmetry in the Møller scattering from the asymmetry in the luminosity monitors. The work leads finally to a conclusion on the model used to extract the asymmetry from the data, separating the background, and about the dominant contributions to the systematic error of the asymmetry. We mention also the results of the existing theoretical calculations of the asymmetry in the deuterium data and make an outlook of the future work of both the experiment and the theory in this field of research.

Chapter 1

The two photon exchange and the elastic electron-nucleon scattering

The Quantum Chromodynamics QCD is the accepted theory at the present to explain the strong interaction. The QCD succeeds in making predictions at high energies where the running coupling constant of the strong interaction is small and perturbation methods can be applied. At medium energies, however, the running coupling constant becomes large and using models about nucleon structure becomes necessary.

This is the theoretical framework where scattering experiments to measure the nucleons form factors make sense to access information about their structure.

The electron scattering is used as a useful tool to investigate the nucleon structure because one side of the interaction, the leptonic current, can be described reliably by QED. Moreover, the Born approximation that uses only the leading term in the perturbation theory, that is, the exchange of one virtual photon, has been enough so far to describe reliably the interaction. The elastic electron-nucleons scattering is used thus to get information about the nucleon form factors.

1.1 The electromagnetic scattering: The Born approximation (one photon exchange)

The elastic scattering is treated through the Born approximation (or one photon exchange), that is, the leading term in perturbation theory. The leptonic current of the interaction can be expressed according to QED as:

$$j^\mu = -ie\overline{u}(k')\gamma^\mu u(k) \tag{1.1}$$

where $u(k)$ is the Dirac-spinor corresponding to the incoming electron with momentum k. The $\overline{u}(k')$ is the Dirac-spinor associated with the outgoing electron
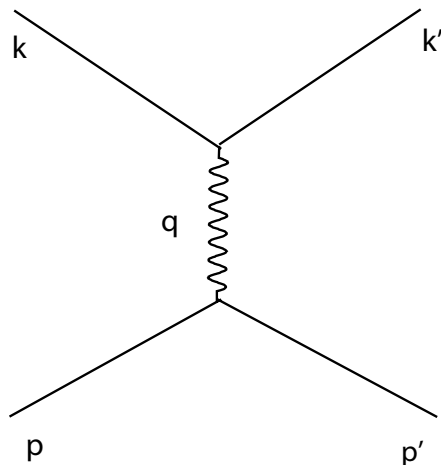
Figure 1.1. The one photon exchange diagram of the elastic electron-nucleon scattering.

of momentum k'. The γ^μ is the Dirac matrix. The interaction of the nucleon is unknown but the nucleon current can be written by imposing without loss of generality some basic principles: Lorentz invariance, current conservation and parity conservation. The most general form of the nucleon current is then [2]:

$$J^\mu = ie\overline{u}(p')\Gamma^\mu u(p) \tag{1.2}$$

where $u(p)$ is the Dirac-spinor of the incoming nucleon of momentum p, $\overline{u}(p')$ is the Dirac-spinor of the outgoing nucleon of momentum p' and the matrix Γ^μ is given by:

$$\Gamma^\mu = F_1(q^2)\gamma^\mu + \frac{1}{2M}F_2(q^2)i\sigma^{\mu\nu}q_\nu = \tag{1.3}$$

$$= G_M(q^2)\gamma^\mu + \frac{1}{2M}F_2(q^2)(p+p')^\mu \tag{1.4}$$

$F_1(q^2)$ and $F_2(q^2)$ are functions only of the squared four-momentum transfer q^2. They are known as the electromagnetic elastic nucleon form factors (or Pauli and Dirac form factors, respectively). G_M is a linear combination of the Pauli form factors. G_E can be defined also as a linear combination of the Pauli form factors. Both are known as magnetic and electric Sachs form factors, respectively.

$$G_E = F_1 - \tau F_2 \qquad (1.5)$$
$$G_M = F_1 + F_2 \qquad (1.6)$$

The electric and magnetic Sachs form factors G_E and G_M are closely related to the nucleon charge distribution and the nucleon current distribution, respectively. In the Breit reference frame, defined by the condition $\vec{p}' = -\vec{p}$, the Sachs form factors can be expressed formally as the Fourier transform of the nucleon charge density and the nucleon current density.

The invariant amplitude is written in terms of the leptonic current, the nucleon current and the virtual photon propagator $(\sim 1/q^2)$.

$$T = j_\mu \frac{1}{q^2} J^\mu \qquad (1.7)$$

In order to calculate the cross section the invariant amplitude must be squared

$$|T|^2 = \frac{e^2}{q^4} \eta_{\mu\nu} W^{\mu\nu} \qquad (1.8)$$

where $\eta_{\mu\nu}$ and $W^{\mu\nu}$ are the second rank Lorentz leptonic tensor and the hadronic tensor respectively.

Finally, applying current conservation and taking into account the density of final states and the initial flux we arrive to the Rosenbluth differential cross section for the elastic scattering of unpolarized electrons off nucleons.

$$\left(\frac{d\sigma}{d\Omega}\right) = \frac{\alpha^2}{4E^2 \sin^4(\theta_e/2)} \frac{E'}{E} \cos^2\frac{\theta_e}{2} \left\{ \frac{\left(G_E\right)^2 + \tau\left(G_M\right)^2}{1+\tau} + 2\tau\left(G_M\right)^2 \tan^2\frac{\theta_e}{2} \right\} \quad (1.9)$$

where

τ	$= -q^2/4M^2$	is the reduced transferred momentum.
E'	$= \frac{E}{1+2E/M \sin^2(\theta_e/2)}$	is the elastic scattered electron energy.
θ_e		is the polar scattering angle.
α	$= 1/137.03599911(46)$	is the fine structure constant.

The elastic scattering in the Born approximation occurs through exchange of a spacelike virtual photon $(q^2 < 0)$ [1] therefore it is usual to work with the variable $Q^2 = -q^2$.

---

[1] The squared four-momentum transfer is spacelike because in the elastic scattering we can always think of a reference frame, the center of mass frame, where there is no energy transference, that is $\omega = 0$ so $q^2 = \omega^2 - |\vec{q}|^2 = -|\vec{q}|^2 < 0$. Where $\omega = E - E'$. In the laboratory frame $\omega > 0$.
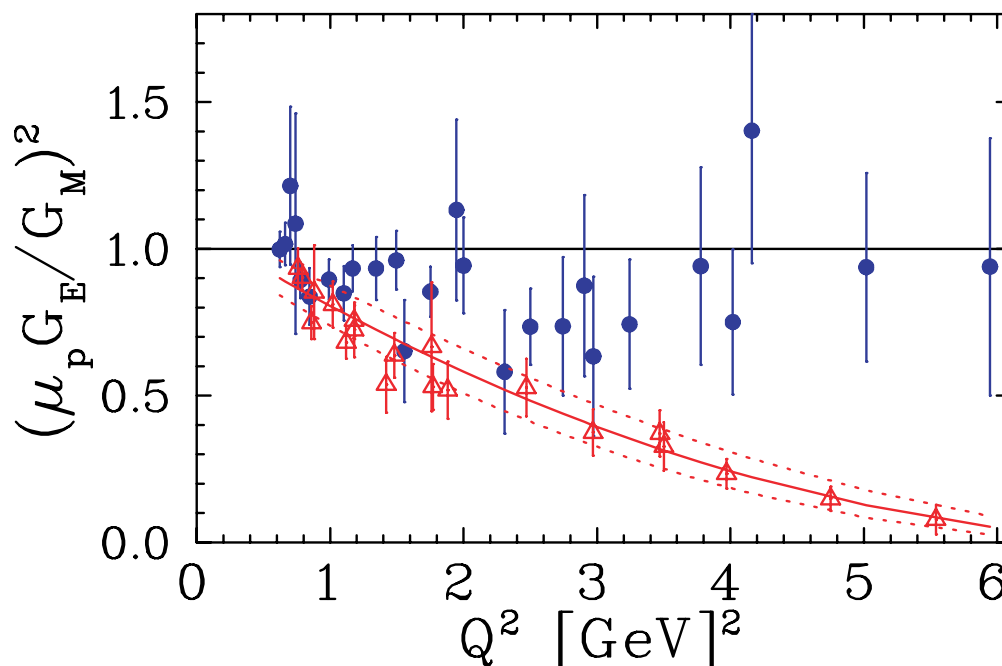
Figure 1.2. Here is shown the discrepancy in the measurement of the ratio G_E/G_M between the Rosenbluth method (blue circles) and the Polarization technique (red triangles). It can be seen that the discrepancy becomes larger for higher transferred momentum. Figure taken from [3]

The square four-momentum transfer can be expressed in terms of the kinematic variables as:

$$Q^2 = 4EE' \sin^2 \frac{\theta_e}{2} \tag{1.10}$$

where the electron mass m_e has been neglected since we are dealing with ultrarelativistic electrons.

Determination of form factors

There are two methods to measure the elastic nucleon form factors:

- The Rosenbluth separation technique

- and the Polarization transfer technique

Both methods are based on the Born approximation.

In the Rosenbluth separation technique one uses an unpolarized beam of electrons and an unpolarized target. The cross section for the elastic electron-nucleon

scattering is measured for different kinematic conditions (E,θ) such that Q^2 is kept fixed [5].

$$\frac{d\sigma}{d\Omega} \propto G_M^2 + \frac{\epsilon}{\tau}G_E^2 \qquad (1.11)$$

where

$$\epsilon = \frac{1}{1 + 2(1 + \tau)\tan^2(\frac{\theta_e}{2})} \qquad (1.12)$$

and τ is the reduced momentum transfer.

The polarization transfer technique uses a polarized electron beam. The beam polarization is transferred to the recoiling nucleon. In the Born approximation the proton polarization along the direction of the momentum transfer P_l is proportional to G_M^2 and the proton polarization in the direction perpendicular to the momentum transfer P_t is proportional to $G_M G_E$. Then one measures the ratio of polarization and therefore one obtains the ratio G_E/G_M [5].

$$\frac{P_t}{P_l} = -\sqrt{\frac{2\epsilon}{\tau(1 + \epsilon)}}\frac{G_E}{G_M} \qquad (1.13)$$

Limits of Born approximation

A discrepancy arises between the measurements done using the Rosenbluth separation and the Polarization transfer technique.

The results of the Rosenbluth separation measurement of the form factors are consistent with $R = \mu_p G_E/G_M \approx 1$ in a Q^2 range < 6 (GeV/c)^2 [1]. The measurement of the ratio R made using the Polarization technique, that is by measuring the ratio of the transverse to longitudinal polarization of the recoil proton can be represented by $R \approx 1 - 0.135(Q^2 - 0.24)$ where Q^2 is in units of (GeV/c)^2 [1]. The results of the measurement can be seen in the figure 1.2. It can be clearly seen the discrepancy becomes greater for increasing values of the four-momentum transfer Q^2.

1.2 Two photon exchange

It has been suggested that the discrepancy between both methods can be explained when taking into account the two photon exchange [6].

The radiative corrections to the elastic electron-nucleon scattering of order α with respect to the Born approximation are used in the analysis of scattering experimental data. But this radiative corrections do not include the exchange of a pair of hard virtual photons (whose momentum transfer is large) because the two photon exchange (TPE) involves unknown hadronic intermediate states.

The investigation of the two photon exchange contribution is motivated by the recent knowledge of the hadronic structure and the discrepancy in the measurements of the nucleon form factors. This investigation allows to solve the discrepancy and also permits the access to information about the nucleon structure beyond that provided by the nucleon form factors.

The two photon exchange contribution can be parametrized through six complex structure functions [6] that appear in the scattering amplitude T. The scattering amplitude can be splitted in two parts: one that contains terms that do not flip the helicity $T_{non-flip}$ and another one that contains terms that flip the helicity T_{flip}.

$$T_{non-flip} = \frac{e^2}{Q^2} \bar{u}(k')\gamma_\mu u(k) \cdot \bar{u}(p')\Big(\tilde{G}_M \gamma_\mu - \tilde{F}_2 \frac{P^\mu}{M} + \tilde{F}_3 \frac{\gamma K P^\mu}{M^2}\Big) u(p) \qquad (1.14)$$

$$T_{flip} = \frac{e^2}{Q^2} \frac{m_e}{M} \Big[\bar{u}(k'u(k) \cdot \bar{u}(p')\Big(\tilde{F}_4 + \tilde{F}_5 \frac{\gamma K}{M}\Big) u(p) + \tilde{F}_6 \bar{u}(p')\gamma_5 u(p) \cdot \bar{u}(p')\gamma_5 u(p) \Big]$$
$$(1.15)$$

where $P = \frac{p+p'}{2}$ being $p(p')$ the nucleon initial(final) momentum, and $K = \frac{k+k'}{2}$ where $k(k')$ is the electron initial(final) momentum, m_e is the electron mass, M is the mass of the nucleon, $\tilde{G}_M$, $\tilde{F}_2$, $\tilde{F}_3$, $\tilde{F}_4$, $\tilde{F}_5$, $\tilde{F}_6$ are complex functions of the kinematic invariant variables ν, Q^2. In the Born approximation they reduce to

$$\tilde{G}_E^{Born}(\nu,\ Q^2) = G_E(Q^2) \qquad (1.16)$$

$$\tilde{F}_2^{Born}(\nu,\ Q^2) = F_2(Q^2) \qquad (1.17)$$

$$\tilde{F}_i^{Born}(\nu,\ Q^2) = 0 \quad i = 3, 4, 5, 6 \qquad (1.18)$$

1.2.1 Cross section of the elastic $e-p$ scattering

The cross section of the elastic $e-p$ scattering can be described with the Born approximation and adding the radiative corrections and the two photon exchange, both of order α with respect to the Born approximation.

$$d\sigma = d\sigma_0(1+\delta) \qquad (1.19)$$

where $d\sigma_0$ is the cross section in the Born approximation and δ includes the radiative corrections and the two photon exchange contribution. The amplitude M_1 of the one-loop corrections of order α relative to the Born approximation includes a term proportional to the Born amplitude $f(Q^2, \epsilon)M_0$ that includes the radiative
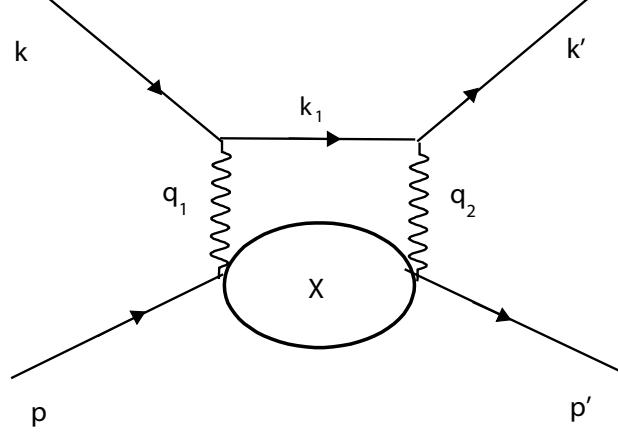
Figure 1.3. The two photon exchange diagram. The electron interacts through two virtual photons with the nucleon. The bubble X in the middle represents any excited intermediate state of the nucleon that is compatible with the kinematic conditions.

corrections independent of the hadronic structure and a term $\bar{M}_1$ that includes the two photon exchange amplitude dependent on the hadronic structure [7]. That is:

$$M_1 = f(Q^2, \epsilon) M_0 + \bar{M}_1 \tag{1.20}$$

The two photon exchange contribution appears through the interference of the term proportional to the Born amplitude M_0 and the amplitude that accounts for the two photon exchange $\bar{M}_1$ [7].

$$\delta = f(Q^2, \epsilon) + \frac{2 Re(M_0 \bar{M}_1)}{|M_0|^2} \tag{1.21}$$

The two photon exchange contribution arises in the cross section through the real part of the structure function $\tilde{F}_3$ [1].

$$\frac{d\sigma}{d\Omega} = \sigma_0 \left\{ |\tilde{G}_M|^2 + \frac{\epsilon}{\tau} |\tilde{G}_E|^2 \right. \tag{1.22}$$

$$\left. + 2\epsilon \sqrt{\tau(1+\tau) \frac{1+\epsilon}{1-\epsilon}} \left(\frac{1}{\tau} |\tilde{G}_E| + \tilde{G}_M| \right) Re\left(\tilde{F}_3(s, Q^2) \right) \right\} + O(\alpha^2) \tag{1.23}$$

The difficulties to investigate the two photon exchange contribution through the cross section measurement are:

1. Theoretical difficulties: To calculate the real part of the structure function $Re\{\tilde{F}_3\}$ one should use the one-loop diagram where all particles are off-shell.

Therefore we need the knowledge of the off-shell form factors of the nucleon in the intermediate state and the amplitudes for all the intermediate states and their off-shell transition form factors [1].

2. Experimental difficulties: The two photon exchange contribution is suppressed by a factor α with respect to the one photon exchange cross section.

Another observable, the normal spin asymmetry, that is proportional to the imaginary part of the two photon exchange provides another way to access the 2γ contribution.

1.2.2 Normal spin asymmetry

With transverse spin polarization there are two observables that allow the access to the imaginary part of the two photon exchange amplitudes [8]:

1. **Target normal spin asymmetry**. The beam is unpolarized and it is scattered by a polarized target transversely to the beam direction.

2. **Beam normal spin asymmetry**. The beam is transversely polarized and the target is unpolarized.

The A4 collaboration experiment works with a polarized electron beam. So we treat in detail the beam normal spin asymmetry.

Beam normal spin asymmetry definition If we consider a beam of transversely polarized electrons, that is electrons whose spin direction is perpendicular to their momentum, the cross section of the elastic scattering off unpolarized nucleons presents an asymmetry for opposite spin states. This asymmetry is originated only by the electromagnetic interaction. The theory predicts a zero normal spin asymmetry if we consider only the one photon exchange approximation, due to the time reversal invariance [8]. The beam normal spin asymmetry is originated at leading order by the two photon exchange amplitude. The normal spin asymmetry is defined as:

$$A_\perp^m = \frac{\sigma^+ - \sigma^-}{\sigma^+ + \sigma^-} \tag{1.24}$$

where $\sigma^+(\sigma^-)$ denote the cross section of the elastic electron-nucleon scattering for an unpolarized nucleon and a electron spin parallel (antiparallel) to the normal polarization vector $\vec{P}$ shown in the picture below.

The normal spin asymmetry has a maximum if the spin direction $\vec{P}$ is perpendicular to the scattering plane and it cancels when the spin is contained in the scattering plane. The normal vector to the scattering plane is defined by:

$$\vec{S}_\perp = \frac{\vec{k} \times \vec{k}'}{|\vec{k} \times \vec{k}'|} \qquad (1.25)$$

If the angle between the spin direction and the normal to the scattering plane is ϕ the normal spin asymmetry is given by

$$A_\perp^m = A_\perp \vec{P} \cdot \vec{S}_\perp = A_\perp \cos\phi \qquad (1.26)$$
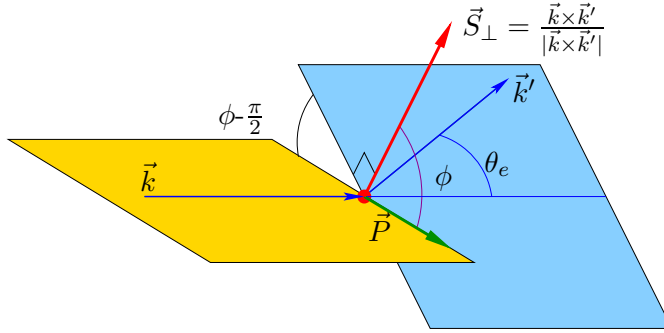
The momentum of the incident electron $\vec{k}$ and the momentum of the scattered electron $\vec{k}'$ define the scattering plane represented in the picture above in blue. θ_e is the scattering angle and ϕ is the azimuthal angle. The plane of the spin is defined by the spin direction $\vec{P}$ and the momentum of the incident electron. The normal vector to the scattering plane $\vec{S}_\perp$ is represented by a red arrow.

Order of magnitude   As it vanishes for one photon exchange it is of order α. Moreover as the electromagnetic interaction is of vector type the helicity is conserved for ultrarelativistic electrons. Therefore a transversely polarized electron interaction suffers a suppression of order m_e/E. The beam normal spin asymmetry is thus of order $\sim \alpha \cdot m_e/E \sim 10^{-2} \cdot 10^{-3} = 10^{-5}$

T-odd observable   Details of the following discussion can be found in [8] or in [9] . It turns out that this asymmetry depends on the absorptive part of two photon exchange amplitude, that is $AbsT_{2\gamma}$. From unitarity of scattering matrix it is proved:

$$i(T_{fi} - T_{fi}^\dagger) = \sum_\Gamma T_{f\Gamma}^\dagger T_{\Gamma i} \qquad (1.27)$$

That means that to calculate asymmetry all intermediate hadronic states must be taken into account. To arrive to the asymmetry expression in terms of two photon exchange amplitude time reversal invariance is applied. Approximating to the leading order term in α:

$$A_\perp = \frac{Im(T_{1\gamma}^* Abs T_{2\gamma})}{|T_{1\gamma}|^2} \tag{1.28}$$

The two photon exchange amplitude is necessary since the scattering amplitude is real at Born approximation.

Note that the asymmetry depends on the imaginary part of the interference term. That is the reason why the asymmetry depends on the imaginary part of the structure functions.

Dependence on the structure functions. The asymmetry $A_\perp$ is given by the imaginary part of the interference term between the one photon exchange amplitude and the absorptive part of the two photon exchange amplitude. Therefore the asymmetry depends on the imaginary part of the structure functions $\tilde{F}_3$, $\tilde{F}_4$, $\tilde{F}_5$ [10].

$$A_\perp = \frac{2m_e}{Q} \sqrt{2\epsilon(1-\epsilon)} \sqrt{1 + \frac{1}{\tau}} \left(G_M^2 + \frac{\epsilon}{\tau}\right)^{-1}$$
$$\left\{ -\tau G_M \mathfrak{Im}\left(\tilde{F}_3 + \frac{1}{1+\tau}\frac{\nu}{M^2}\tilde{F}_5\right) - G_E \mathfrak{Im}\left(\tilde{F}_4 + \frac{1}{1+\tau}\frac{\nu}{M^2}\tilde{F}_5\right) \right\} + \mathcal{O}(\alpha^2) \tag{1.29}$$

Relation to the cross section The imaginary part of the structure functions $Im\{\tilde{F}_3\}$, $Im\{\tilde{F}_4\}$, $Im\{\tilde{F}_5\}$ can be extracted if we measure the asymmetry $A_\perp$. The knowledge of $Im\{\tilde{F}_3\}$ may help to calculate the real part of this structure function $Re\{\tilde{F}_3\}$ by applying dispersion relations [1].

Model calculation

There is a model calculation [10] of the absorptive part of the two photon exchange amplitude through the absorptive part of the doubly virtual Compton scattering tensor on the nucleon. That is the tensor that describes the interaction of nucleon with the virtual photons (the electron electromagnetic field). But since the nucleon is a composite state we must carry out a sum over the amplitudes of all possible intermediate excited states.

$$AbsT_{2\gamma} = e^4 \int \frac{d^3\vec{k_1}}{(2\pi)^3 2E_{k_1}} \bar{u}(k',h')\gamma_\mu(\gamma \cdot k_1 + m_e)\gamma_\nu u(k,h)\frac{1}{Q_1^2 Q_2^2}W^{\mu\nu}(p',\lambda';p,\lambda)$$
(1.30)

Where the integral is carried out over all momenta of the intermediate electron. The first factor is the Lorentz invariant phase space volume of integration. The following factors are the Dirac spinors for incoming and outgoing electron and the free propagator for intermediate electron with momentum k_1. The factor $\frac{1}{Q_1^2 Q_2^2}$ relates to the virtual photon propagators. It plays an important role since any pole in virtualities correspond to a leading contribution of some intermediate states. This is especially relevant at backward angles.

And the absorptive part of the doubly virtual Compton scattering tensor with two space-like photons:

$$W^{\mu\nu}(p',\lambda';p,\lambda) = \sum_X (2\pi)^4\delta^4(p + q_1 - p_X) < p',\lambda'|J^{\dagger\mu}(0)|X><X\lambda|J^\nu(0)|p,\lambda >$$
(1.31)

The sum is over all intermediate on-shell hadronic states.

From the expression for $AbsT_{2\gamma}$ eq. 1.30 and using eq. 1.28 the asymmetry can be expressed by the expression [10]:

$$A_\perp = \frac{1}{(2\pi)^3}\frac{e^2 Q^2}{D(s,Q^2)}\int_{M^2}^{(\sqrt{s}-m_e)^2} dW^2 \frac{|\vec{k_1}|}{4\sqrt{s}}\int d\Omega_{k_1}\frac{1}{Q_1^2 Q_2^2}Im\{L_{\alpha\mu\nu}H^{\alpha\mu\nu}\}$$ (1.32)

The denominator is given through the one photon exchange:

$$D(s,Q^2) = \frac{Q^4}{e^4}\sum_{spins}|T_{1\gamma}|^2 = 8\frac{(4M^2\tau)^2}{1-\epsilon}\left(G_M^2 + \frac{\epsilon}{\tau}G_E^2\right)$$ (1.33)

Note that the integral over intermediate electron momentum $\frac{d^3\vec{k_1}}{(2\pi)^3 2E_{k_1}}$ is written as an integral over the solid angle of the intermediate electron and an integral over the invariant mass of the nucleon intermediate state that goes from $W^2 = M^2$ when the intermediate state is the nucleon itself up to $W_{max} = \sqrt{s} - m_e$, since $s = E_{CM}^2 = (m_e + W_{max}^2)$.
Where

$$L_{\alpha\mu\nu} = \bar{u}(k',h')\gamma_\mu(\gamma \cdot k_1 + m_e)\gamma_\nu u(k,h) \cdot [\bar{u}(k',h')\gamma_\alpha u(k,h)]^*$$ (1.34)

and
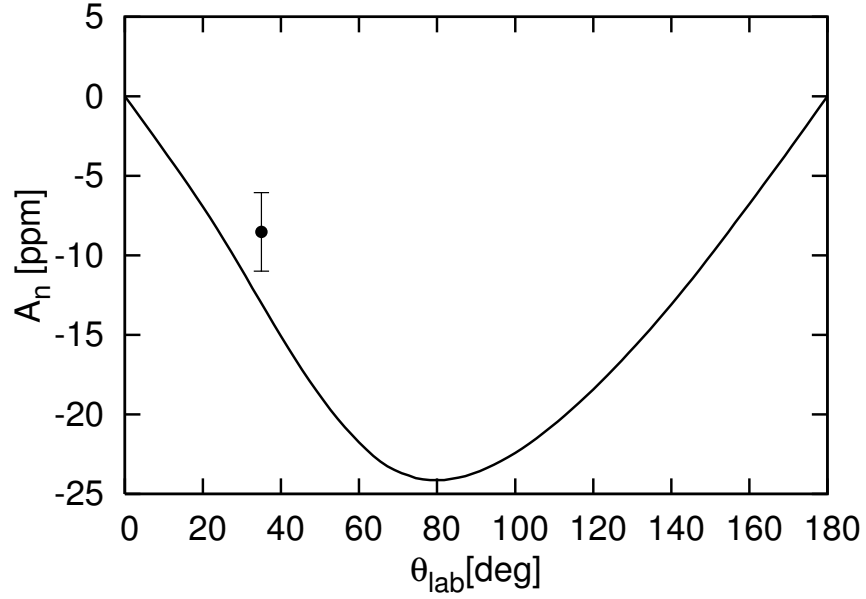
Figure 1.4. Model calculation of beam normal spin asymmetry in the process $e^{-\uparrow}p \rightarrow$ $e^- p$ at 855 MeV and forward angles configuration as function of laboratory polar angle. It corresponds to the transferred momentum $Q^2 = 0.23$ GeV^2. The data point from A4 is shown [1]

Figure 1.5. Model calculation of beam normal spin asymmetry in the process $e^{-\uparrow}p \rightarrow$ $e^- p$ at 570 MeV beam energy and forward angles configuration as function of laboratory polar angle. It corresponds to the transferred momentum $Q^2 = 0.11$ GeV^2. The data point from A4 is shown [1]
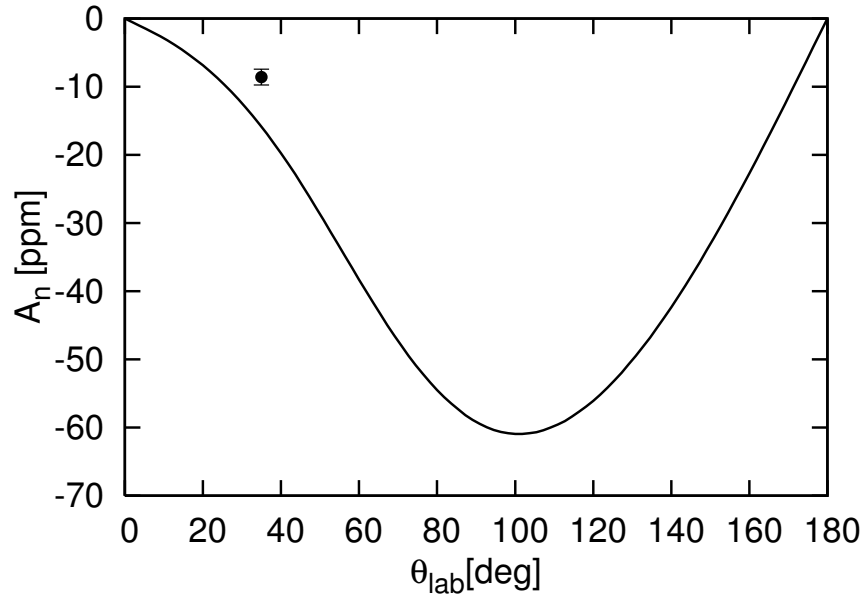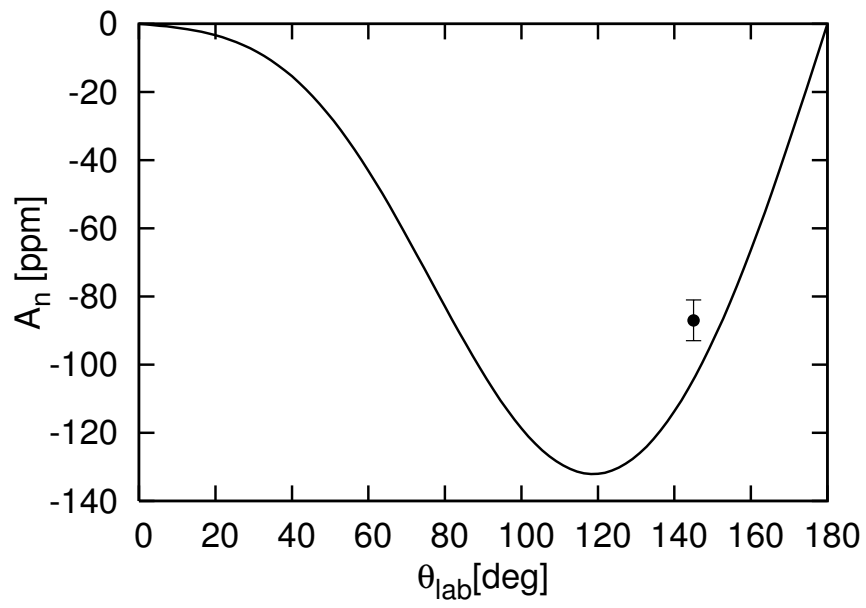
Figure 1.6.   Model calculation of beam normal spin asymmetry in the process $e^{-\uparrow}p \to e^{-}p$ at 315 MeV beam energy and backward angles configuration as function of laboratory polar angle. It corresponds to the transferred momentum $Q^2 = 0.23$ GeV^2. A very preliminary analysis data point is shown [11]

$$H^{\alpha\mu\nu} = W^{\mu\nu} \cdot [\bar{u}(p', \lambda_N')\Gamma^\alpha u(p, \lambda_N)]^* \qquad (1.35)$$

The model for the hadronic tensor $W^{\mu\nu}$ includes an elastic contribution, corresponding with the nucleon as the intermediate state, and the inelastic contribution, corresponding to πN intermediate states [10].

The elastic contribution is calculated using the on-shell nucleon electromagnetic from factors. On the other hand, the pion electroproduction currents (that describe excitation and deexcitation of the πN intermediate state) are calculated by means of the invariant amplitudes provided by MAID. The calculation takes into account both resonant and nonresonant pion production.

One interesting fact is that when the momentum of the intermediate electron goes to zero $k_1 \to 0$, that corresponds to a maximal value of the hadronic intermediate state mass $W_{max} = \sqrt{s} - m_e$, then the virtualities of the intermediate photons present a singularity of order of electron mass m_e. As the photons are quasireal this kinematic situation is known as quasireal Compton scattering.

$$Q_1^2 = (k - k_1)^2 \approx k^2 = m_e^2 \qquad (1.36)$$

As a consequence, under some kinematic conditions these singularities will give important contributions. In figures 2.1,1.5,1.6 we show the model calculated beam normal spin asymmetry for scattering off proton $e^{-\uparrow}p \to e^- p$ as a function of the lab scattering angle for the energies 855 MeV, 570 MeV, 315 MeV respectively. The first two energies have been employed in the A4 experiment in the forward angle configuration corresponding to $Q^2 = 0.23 GeV^2$ and $Q^2 = 0.11 GeV^2$ respectively. The asymmetry data points are also plotted. The plots show a slight overprediction of model. The third energy 315 MeV corresponds to $Q^2 = 0.23 GeV^2$ at backwards angles. The point plotted comes from a very preliminary analysis. But it also shows a small overprediction of model.

Model calculation for neutron   The model calculation has been also applied to the process $e^{-\uparrow}n \to e^- n$. We can see in the figure 1.7 a comparison of the beam normal spin asymmetry as function of the CM polar scattering angle for both processes: scattering off the proton (left panel) and scattering off the neutron (right panel). The asymmetries for neutron and proton are of opposite sign and of similar magnitude [10]. As we are measuring the asymmetry in the quasielastic scattering off the deuteron this result is the more significant for us. The calculations have been done for the free nucleons. The calculation for the deuteron as a bound state of proton and neutron has not been carried out yet. According to the very naïve static model in which the nucleus is represented as a collection of free nointeracting nucleons at rest the measured asymmetry with the deuterium target should be near zero.
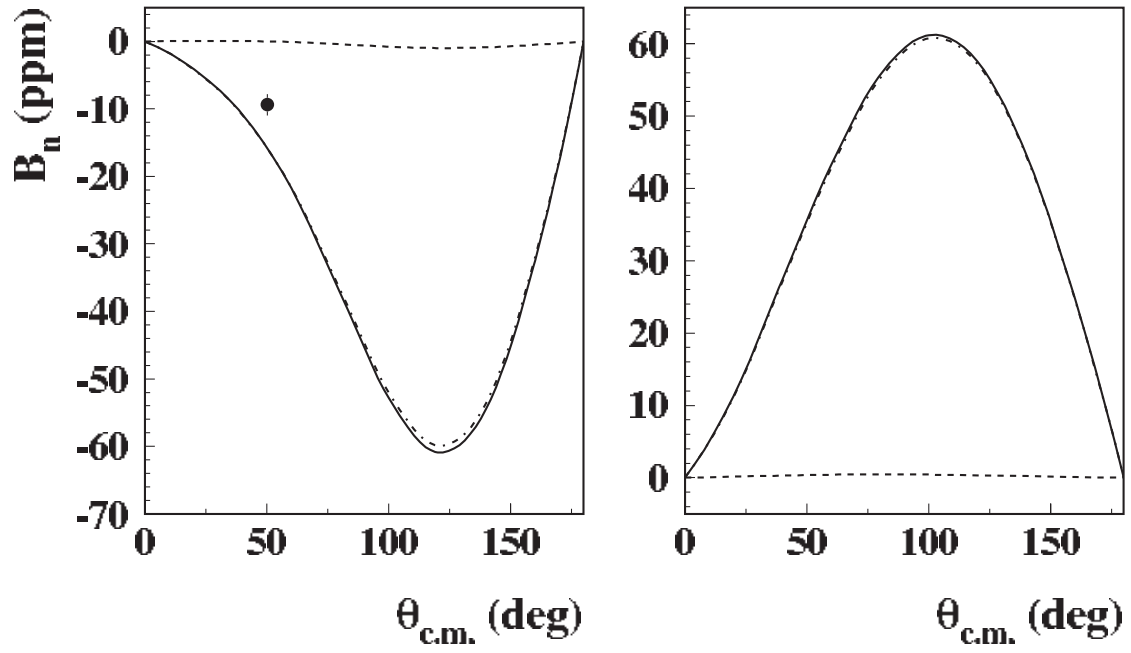
Figure 1.7. Comparisons fo the beam normal spin asymmetry for the processes at beam energy 570 MeV as a function of CM scattering angle for different hadronic intermediate states.

Chapter 2

Quasielastic *e-d* scattering

2.1 Quasielastic electron-nucleus scattering

The scattering of high energy electrons off nuclei present some features in the energy spectrum depending on the energy loss. For low energy loss one can see a peak corresponding to the elastic scattering of the electron from the nucleus as a whole. Other peaks appear that are associated with inelastic processes of excitation of nuclear bound states.

When a larger amount energy is lost by the electron a broad peak arises due to the quasielastic scattering on the bound nucleons of the nucleus. As the nucleons are confined in nucleus whose size is of the order of 1 fm the wave function in the momentum space is spread over some distribution of momenta whose size is of order of 100 MeV. It is said the bound nucleons undergo Fermi motion. The quasielastic scattering is therefore the scattering of the electron from an individual moving nucleon. The Fermi motion is the cause of being the quasielastic peak broader. The knock-out nucleon is ejected from the nucleus after interacting with the other nucleons [12].

At larger energy losses some peaks appear that correspond to the excitation on the nucleon of different resonances. At very large energy losses a structureless continuum due to the Deep Inelastic Scattering on quarks of the bound nucleons appears.

Some general features of the quasielastic scattering are:

- The quasielastic cross section integrated over electron energy loss is proportional to the sum of electron-nucleon cross section.

- The quasielastic peak width is a measure of the average momentum of the nucleons in nuclei and can be used to determine the nuclear Fermi momentum.
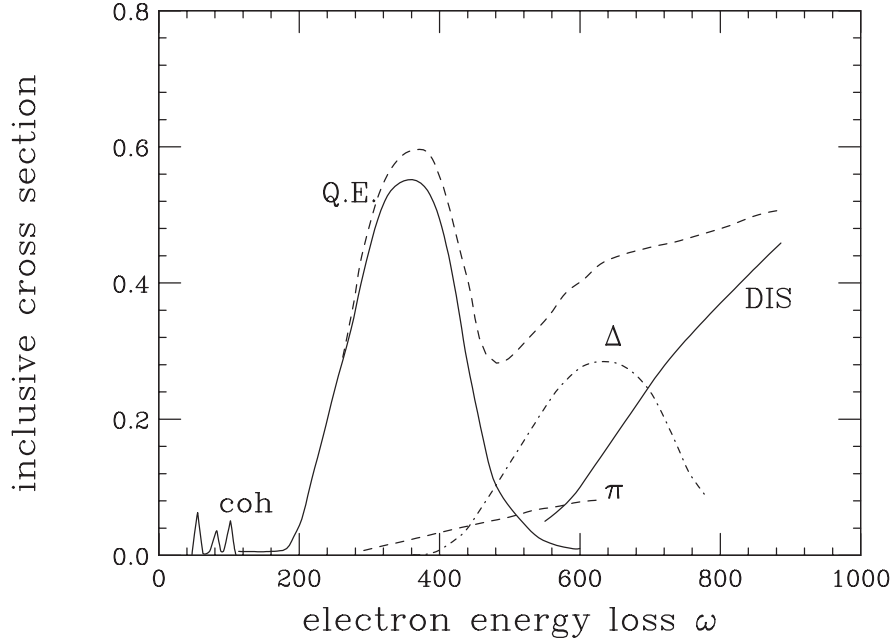
Figure 2.1. Schematic representation of inclusive cross section as function of energy loss. Taken from [12]

- The shape of the quasielastic peak depends on the distribution in energy E and momentum k of the initial bound nucleons. The nuclear structure function $S(E, k)$ describes the momentum distribution.

2.2   Quasielastic electron-deuteron scattering

The deuteron is a very weakly bound system composed of a neutron and a proton. The deuteron binding energy is only $\varepsilon = 2.2$ MeV. On the other hand the kinetic energy of the deuteron's bound nucleons, the Fermi motion, is not negligible since the potential is about 20 MeV deep. Several models and approximations of the nuclear aspects of the interaction with the electron are unavoidable to extract information about the nucleon structure functions even when treating with such a simple nuclear system as the deuteron.

The scattering process of the electron can be a coherent elastic scattering off the deuteron as a whole remaining the deuteron in the ground state after the collision, or it can be an incoherent quasielastic scattering with electrodisintegration of the deuteron, that is an unbound neutron and proton in the final state. The scattering occurs from one of the bound nucleons as a quasifree process while the other

nucleon acts as a spectator. For momentum transfers which are large compared to the deuteron size we expect the quasielastic scattering to be the dominating [13].

Investigations of the nuclear model dependences of the two photon exchange asymmetry in the quasielastic scattering are not available so far. Nevertheless some examinations have been done for the nuclear physics aspects of the parity violating asymmetry in the quasielastic e-d scattering [15] which is also an objective of the A4 collaboration experiment. Despite the parity violating asymmetry is due to a different physical process, the interference of the one photon exchange and the Z^0 boson exchange, the nuclear models employed to understand the asymmetry in the quasielastic scattering might be useful to have some hints about the existing nuclear models and the path to follow in the investigation of the two photon exchange asymmetry in the quasielastic e-d scattering. Therefore we present the descriptions of the nuclear models and the results corresponding to the parity violating asymmetry given by [15].

- **The static approximation** It is the simplest of the models. The nucleons are supposed to be free nucleons at rest so that the nuclear matrix elements are incoherent sums of matrix elements of the single-nucleon at rest.

- **Nonrelativistic calculation with final-state interactions (FSI)** The system np is treated in terms of nonrelativistic solutions of the Schrödinger equation with realistic NN potentials. The matrix elements of the nuclear charge density and the nuclear current are taken between the deuteron ground state and the np final state expanded in partial waves. Some partial waves are considered and those with lower angular momentum are solutions of the Schrödinger equation while the rest are plane-wave solutions.

- **Plane-wave Born approximation (PWBA)** The PWBA is obtained from the FSI model by replacing the final interacting np state by a plane-wave state.

- **Plane-wave impulse approximation (PWIA)** The factorized relativistic plane-wave impulse approximation is the model used at high momentum transfer when the relativistic effects become important. In this model the interaction occurs with a bound nucleon assumed to be quasifree and the other nucleon acts as a spectator. The bound nucleons have a Fermi motion due to the nuclear binding. Therefore the scattering is not with a nucleon at rest but with a moving nucleon. The nucleon motion is described through the deuteron wave-function in the momentum space that is related to the probability of finding a the nucleon with determined energy and momentum. Since the deuteron binding energy is small compared to the free nucleon mass (939 MeV) the bound nucleon masses receive small binding corrections. The

cross section of the quasielastic scattering in the PWIA can be factored in
two terms:

- the spectral function that represents the probability to found a bound
  nucleon with a given momentum and energy

- and the half-off-shell single nucleon cross section, using for example the
  parametrization of de Forest [14].

2.2.1   Nuclear model dependencies for the parity violating asymmetry

In the work [15] they have calculated the parity violating asymmetry in the
quasielastic *e-d* scattering using the static approximation, the FSI model with two
different models for the NN interaction, the PWBA and the PWIA. They show
the results at two different angles: at forward angle 35° and an extreme backward
angle 170°. The asymmetry is in function of the energy loss ω for a wide range of
momentum transfers $q = 150, 300, 500, 1000$ and 1500 MeV/c. See figures [?] and
[?].

The results of [15] show significant model dependencies at low momentum
transfers. On the other hand, the model dependencies disappear at sufficiently
high momentum transfers q. In the regions away from the QE peak the model
differences are more important that in the QE peak itself. At the QE peak the
model calculations converge as the momentum transfer increases. The convergence
is slower for forward angles 35° and faster for backward angles 170°.
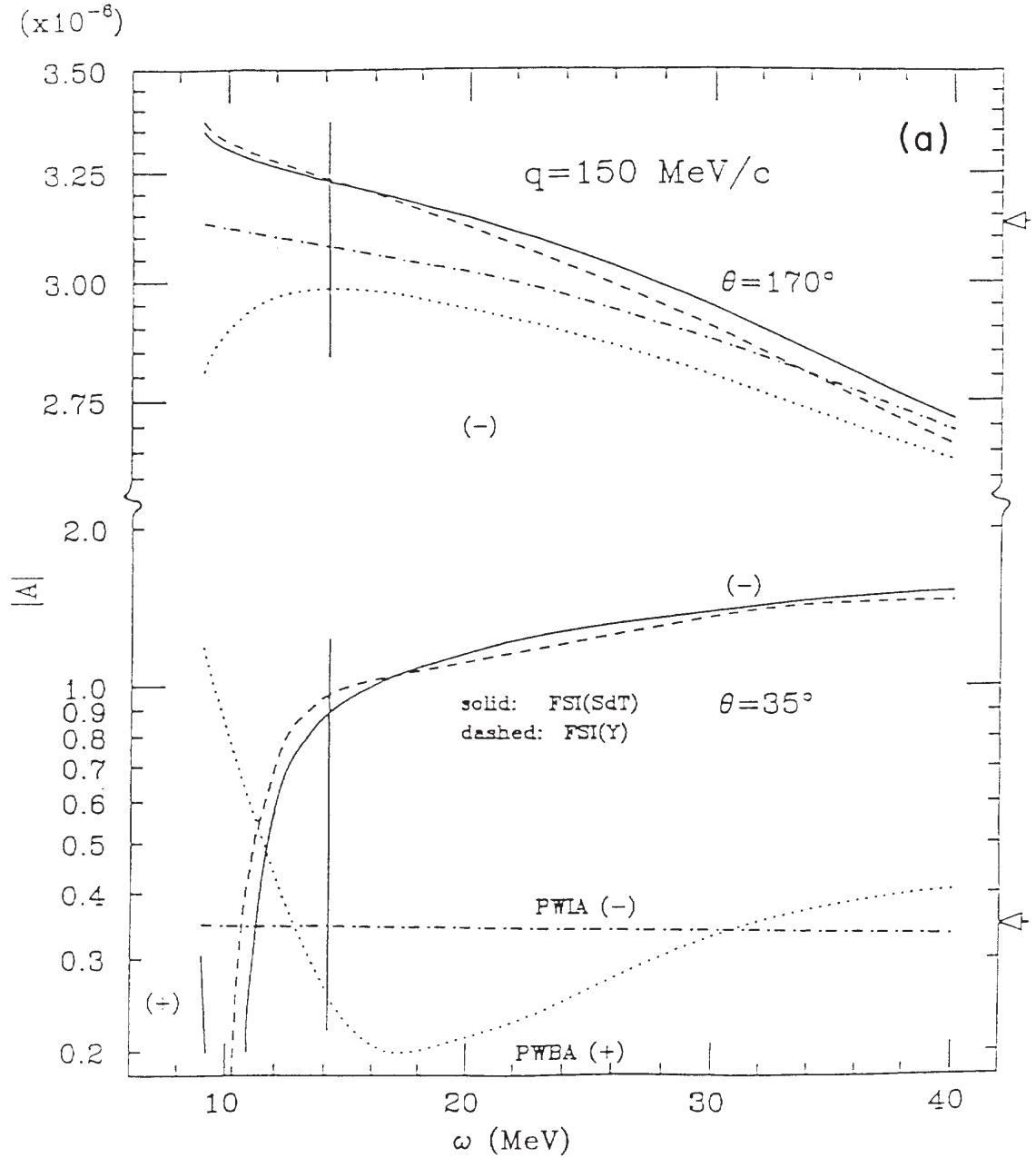
Figure 2.2. The magnitude of the PVA as a function of the energy transfer ω, at $q = 150$ MeV/c for two values of the electron scattering angle. Results of different nuclear models are shown: FSI with SdT potential with solid line, FSI with the Yale potential (dashed), PWBA (dashed), and PWIA (dot-dashed). The (+) and (-) signs indicate positive and negative values of the asymmetry. The vertical line indicates the position of the quasielastic peak and the arrows at right vertical axis indicate the value of the absolute PVA at the QE peak in the static approximation.
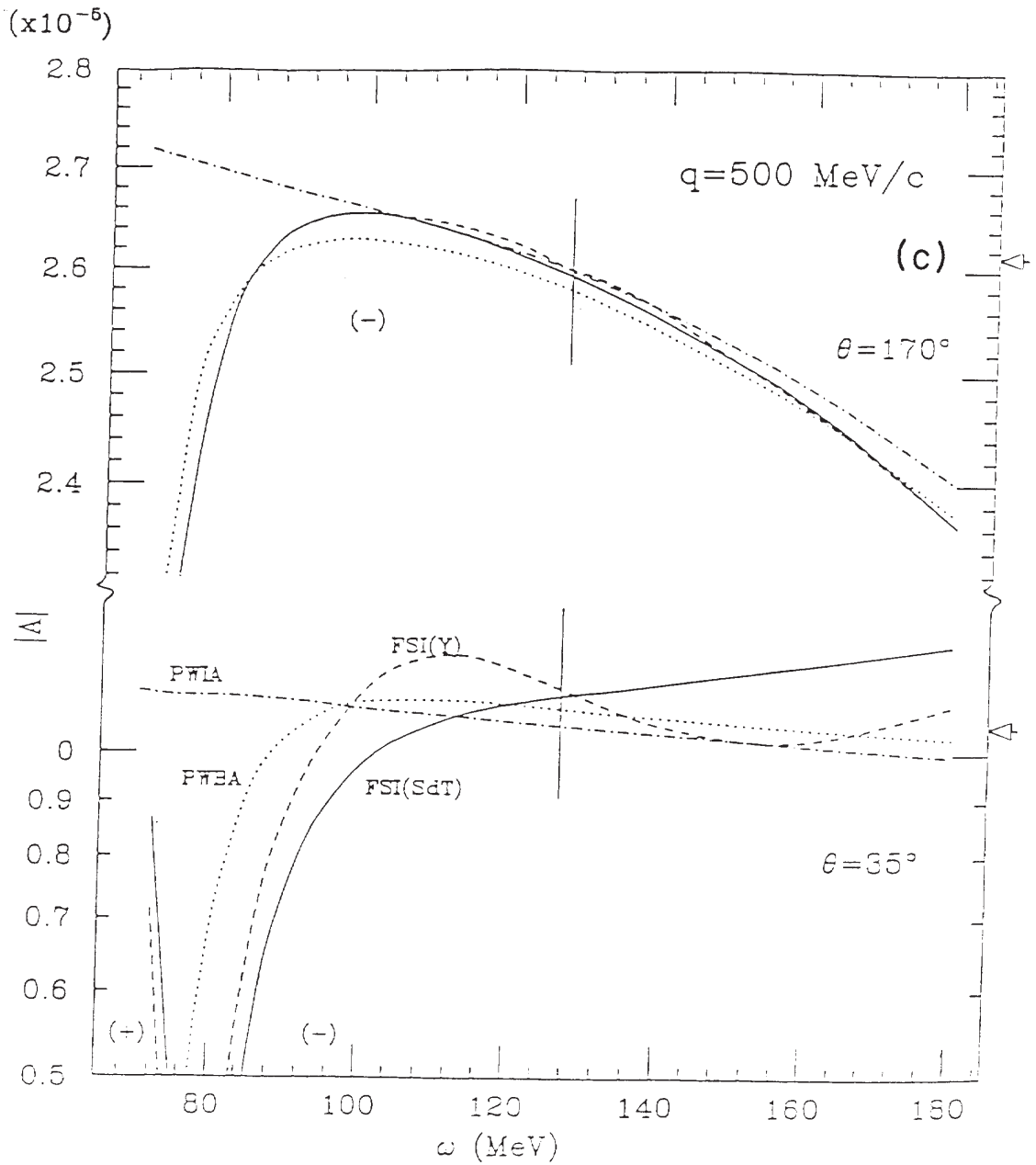
Figure 2.3. The magnitude of the PVA as a function of the energy transfer ω, at $q = 500$ MeV/c for two values of the electron scattering angle. Results of different nuclear models are shown: FSI with SdT potential with solid line, FSI with the Yale potential (dashed), PWBA (dashed), and PWIA (dot-dashed). The (+) and (-) signs indicate positive and negative values of the asymmetry. The vertical line indicates the position of the quasielastic peak and the arrows at right vertical axis indicate the value of the absolute PVA at the QE peak in the static approximation

Chapter 3

The A4 experiment

3.1 Measurement principle

The objective of this work is the measurement of an asymmetry in the cross section of transversely polarized quasielastic scattered electrons off an unpolarized deuterium target. The asymmetry in the cross section is defined as:

$$A = \frac{d\sigma^+ - d\sigma^-}{d\sigma^+ + d\sigma^-} \qquad (3.1)$$

A beam of transversely polarized electrons arrives to the unpolarized deuterium target. A detector counts the number of quasielastically scattered electrons corresponding to both polarization states N^+ and N^-. From these counts a raw asymmetry can be obtained:

$$A = \frac{N^+ - N^-}{N^+ + N^-} \qquad (3.2)$$

The raw asymmetry is a first good approximation to the asymmetry in the cross section σ, because the cross section is the quotient between the count rate R and the luminosity L, $\sigma = R/L$ and the absolute value of the luminosity is equal for both polarization states.

3.2 an overview of the set up

The A4 experiment is carried out at the MAMI accelerator facility. There is a source of a polarized electron beam. The beam is accelerated up to the desired energy and the spin orientation of the electrons is selected. In this work the spin orientation is perpendicular to the beam direction and contained in the accelerator horizontal plane. The beam is transported to the A4 experimental hall
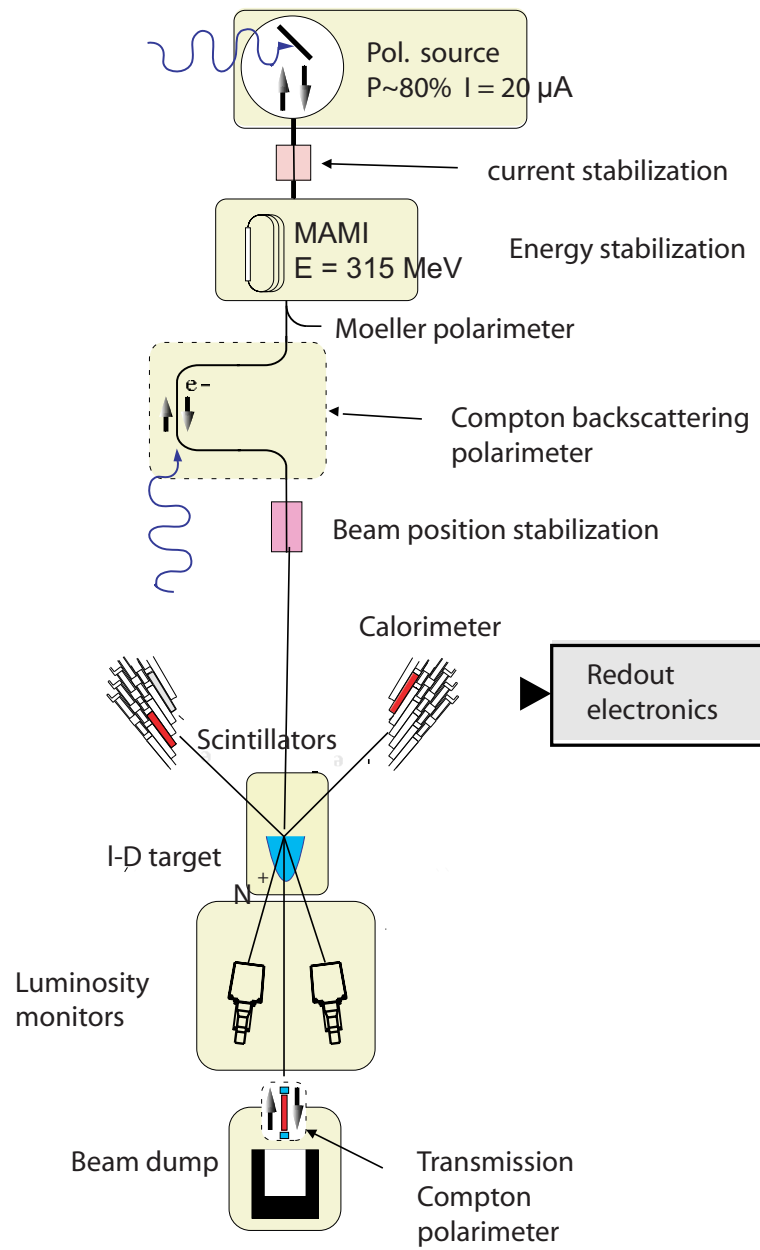
Figure 3.1. Schema of the experimental concept.

where the target is. In the target the electrons are scattered. A detector counts the number of the scattered electrons. Before the target several beam monitors control the fluctuations in the beam properties like position, angle, energy and current intensity since any helicity correlated differences in these properties will produce false asymmetries. The analysis and the correction of these false asymmetries are a central topic of this thesis. In the A4 experiment several polarimeters are used to measure the beam polarization degree P_e that is also a crucial point of the asymmetry measurement, since P_e reduces the value of the measured asymmetry A_m with respect to the physical asymmetry A_{ph} by the relation:

$$A_m = P_e \cdot A_{ph} \tag{3.3}$$

The beam source is also relevant for the asymmetry measurement, because it may be the source of the helicity correlated beam properties differences, which are mentioned before.

3.3   The source of polarized electrons

The source consists of a photocathode "strained layer" GaAs crystal that emits longitudinally polarized electrons when it is illuminated by a circularly polarized laser light. The electron beam has a current intensity for our experiment of 20 μA and a polarization degree of around 80 %. The helicity of the laser is switched every 20 ms so that the helicity of the emitted electrons is switched in the same period.

Basic optical components

The laser light is produced in pulses of 100 ps of width by a semiconductor-laser whose frequency is synchronized with master frequency of MAMI that is 2.45 GHz. The laser light is collimated and it crosses a polarizer emerging with an optimum linear polarization.

The linear polarized light goes through a Pockels cell that acts as a $\lambda/4$ plate. The Pockels cell converts the input linear polarized light into circularly polarized light. The optical properties of the Pockels cell can be changed applying an electric field. A control device generates a sequence of states that change the sign of the voltage in the Pockels cell and therefore its optical axis so that the Pockels cell can be used to switch the helicity of the circularly polarized light. The Pockels cell allows a fast reverse of the polarization states. The circularly polarized laser light illuminates the photocathode.
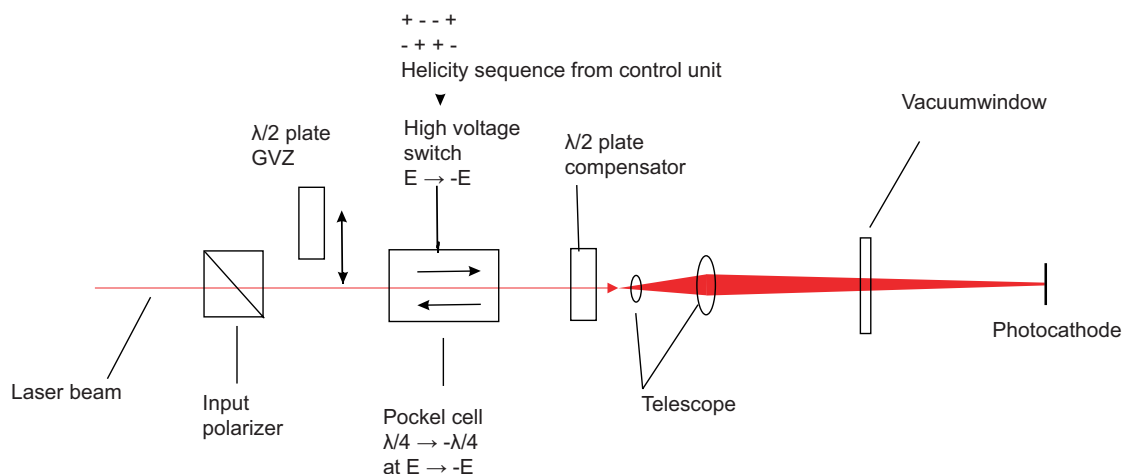
Figure 3.2. Schematic picture of the polarized beam source. Picture taken from [16].

Control of false asymmetries at source

Helicity sequence   The A4 electronic system specifies the spin state change every 20 ms. It is synchronized with the electrical network frequency of 50 Hz. The reason is that if these frequencies do not match the electrical network becomes a source of electronic noise that one wants to avoid. The polarization pattern is generated in a set of four 20 ms long states. The first period is chosen randomly; the second period is the complementary of the first one. The third and the fourth periods are the complementary of the first two. That is, patterns of the type $+--+$ or $-++-$, where $+$ and $-$ denote the helicity states, are randomly generated. This ensures that the polarization states and their transitions are produced with the same probability and it allows to avoid any correlation between the measured asymmetry and the polarization switching frequency. Finally the state sequence is transmitted to the A4 data acquisition system.

Optical devices   Due to either optical imperfections or deviations in the applied voltage in the Pockels cell, a small degree of linear polarization components appears [16]. These linear components might be helicity correlated because of their dependence on the applied voltage to the Pockels cell. Since the photocathode is also sensitive to these linear polarized light components, a non-vanishing asymmetry in current intensity will arise. That asymmetry will be high enough to dominate the physical asymmetry and for that reason its dependence on the source parameters must be investigated in order to reduce it.

A rotable half wave plate, which is located between the Pockels cell and the

photocathode, is used to minimize the current asymmetry. The minimization is based in the fact that the photocathode behaves as an imperfect dichroic polarizer since it is an asymmetric crystal [16]. That means that the abortion depends on the orientation of the incoming linear polarized light. As the emission current is proportional to the absorbed light there is a modulation of the emitted current with respect to a rotation of the polarization. The switch of helicity generates a 90° rotation of the residual linear components. This gives rise to a nonzero helicity correlated beam intensity asymmetry. The half wave plate can be rotated in a way that this asymmetry is minimized.

A telescope is also used to focus the laser beam onto the photocathode. It reduces the angular deviations.

An additional half wave plate is introduced before the Pockels cell so that the helicity is switched independently of the action of the Pockels cell. This half wave plate is known as GVZ (general sign changer). The duration of GVZ changes is much longer than the Pockels cell switching. It is changed during the A4 data taking in periods between 25-100 hours of effective measurement. All devices are in principle unaware of the actual GVZ state. It allows the experimenter an independent way of checking the correct change in sign of asymmetries. Some false asymmetries probably depend on voltages states of Pockels cell so they will not change sign when changing this GVZ status. On the other hand the physical asymmetry should change sign. This has a crucial role in correcting the physical asymmetry from false asymmetries via the multilinear regression method as we will discuss later. In addition, some false asymmetries that do not change sign depending on the GVZ status, like that due to differences in time duration of polarizations states, are reduced when GVZ samples are combined because the sign of the measured asymmetry in GVZ=IN samples must be changed to make the combination with GVZ=OUT samples and therefore the false asymmetries mostly cancel out.

3.4   The accelerator

The MAMI accelerator consists of an injector, a linear accelerator where the beam reaches the energy of 3.46 MeV, and three race-track microtrons (RTM).

One RTM consists of two dipoles and a linear accelerator that is located between the dipoles (see figure 3.3). The linear accelerator consists of high frequency cavities that work at the MAMI master frequency of 2.45 GHz. The beam is deviated by the dipole magnetic field with an increasing radius every turn it gains energy. The dipoles redirect the beam to the linear accelerator where it is accelerated again.

The RTMs accelerate the beam up to energies of 14.35 MeV, 180 MeV and
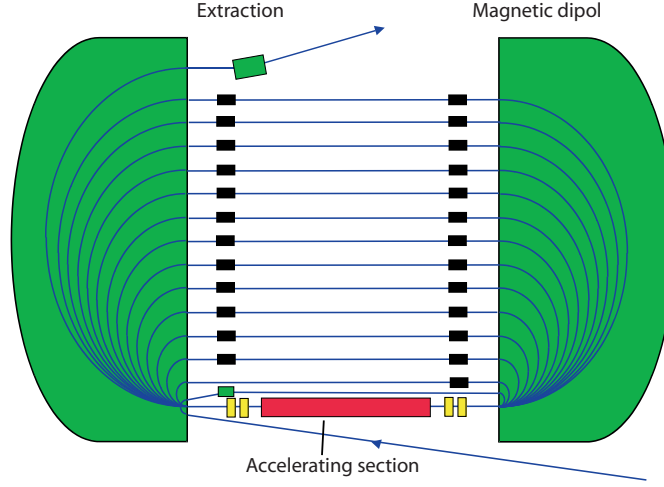
Figure 3.3. Race-track microtron. The electron beam obtains energy in the accelerating section through the action of microwave resonant cavities. Then the electron trajectory is bent by the perpendicular dipole field. A set of pipes that fit with the increasing bending radius of the electron trajectory lead the electron to the opposite dipole where the beam is redirected to the linear accelerator. If in each turn the electrons gains the energy ΔE after n turns its energy will be $n \cdot \Delta E$. Picture from [17]

854.3 MeV, respectively. Through early beam exits in the last RTM the energy can be chosen between 180 MeV and 854.3 MeV in skips of 15 MeV. After running the three microtrons the beam is transported to the several experimental halls.

3.5   Spin dynamics in the accelerator

The spin motion in an electromagnetic field is described by the Thomas-BMT equation [18] given by

$$\vec{\omega}_s = \frac{e}{m\gamma}[(1+a)\vec{B}_\parallel + (1+a\gamma)\vec{B}_\perp - \left(a + \frac{1}{1+\gamma}\right)\frac{\gamma}{c^2}\vec{v} \times \vec{E}] \qquad (3.4)$$

where γ is the Lorentz factor, $\vec{E}$ is the electric field, $\vec{B}_\perp$ is the component of the magnetic field perpendicular to the electron momentum, $\vec{B}_\parallel$ is the component of the magnetic field parallel to the momentum and $a = \frac{g-2}{2} \approx \frac{1}{862}$ is the electron anomalous magnetic moment.

The electron is accelerated by an electric field $\vec{E}$ parallel to its momentum. The guiding magnetic field $\vec{B}$ is perpendicular to its momentum. The spin precesses around the magnetic field with an angular frequency

$$\vec{\omega}_s = (1+a\gamma)\vec{\omega}_c \qquad (3.5)$$

where $\omega_c = \frac{eB}{m_e\gamma}$ is the cyclotron frequency.

Since ω_s is not a multiple integer of ω_c the final spin direction of the electron is no longer parallel to its momentum direction as it is when the electron are emitted from cathode. Using this property of spin dynamics any orientation for the spin (in the plane of the accelerator) can be obtained. However as the number of times the electron crosses the dipole magnetic field is related with the reached energy only a determined energy is the suitable for a given spin direction.

In order to achieve a higher flexibility in both the choice of the beam energy and the spin orientation a Wien-Filter is used.

3.6   Wien Filter

A Wien-Filter spin-rotator is installed in the injection beam line at a beam energy of 100 KeV. It consists of a homogeneous electric $\vec{E}$ and magnetic $\vec{B}$ field which are perpendicular to each other and transverse to the direction of the particle motion. If we want to achieve an angle θ_s of spin rotation without deviating the electron from its straight line trajectory the fields must fulfil the equilibrium force relation

$$\vec{B} \times \vec{v} = \vec{E} \tag{3.6}$$

If the equilibrium force relation is satisfied and assuming $a << 1$, the relation between the magnetic field B and the spin rotating angle θ_s is [19]

$$B = \frac{mc\gamma^2\beta\theta_s}{eL} \tag{3.7}$$

where γ is the Lorentz factor, $\beta = v/c$ and L is the effective field length.

3.7   Target

The target material consists of liquid deuterium ℓD_2 contained in a target cell.

Target cell The target cell is a paraboloid-shaped thin aluminium container. The length of the cell along the beam axis is 10 cm at forward angles and 23.3 cm at backward angles. The target cell is symmetric with respect to the beam axis as one can see in figure 3.4.

Deuterium as target In the table below, we show the physical properties of liquid deuterium and compare them with those of liquid hydrogen. The liquid deuterium radiation length is smaller than that of hydrogen. Therefore the beam
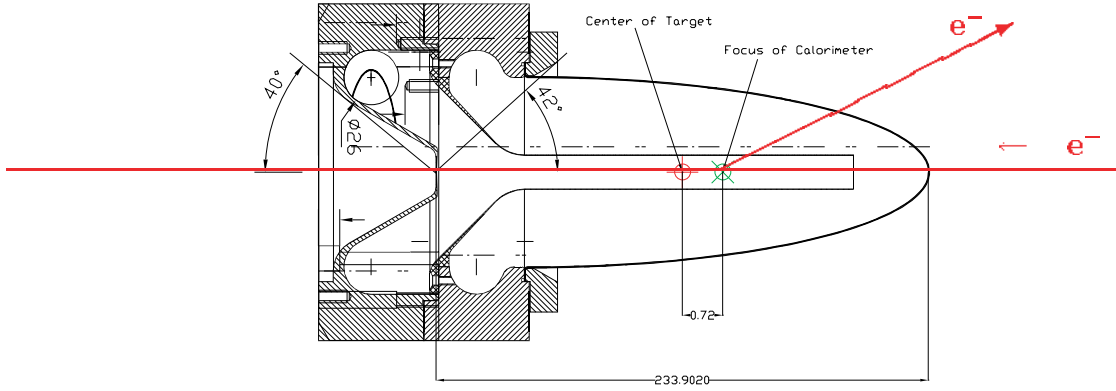
Figure 3.4. Side view of the target at backward angles. The dimension of the target length is in mm

loses more energy as it crosses the liquid deuterium. At backward angle configuration ($l = 23.3$ cm) beam goes through about 3.5×10^{-2} radiation lengths for ℓ-D_2 and about 2.7×10^{-2} radiation lengths for ℓ-H_2.

target	$X_0(cm)$	ρ	$M(g/mol)$	$T_{\mathrm{boil}}(K)$	$T_{\mathrm{frz}}(K)$
ℓ-H_2	866	0.0708	1.0079	20.4	14.0
ℓ-D_2	724	0.1624	2.0140	23.6	18.6

We show the density, the molar mass, the boiling point temperature and the freezing point temperature [20].

The target is kept as liquid in order to have a high density that guarantees a high luminosity. To keep them as liquids we have developed a sophisticated cooling system [21]. The power deposited by the beam is 100 W. The heat deposition produces an increase of the target temperature and may produce boiling. The boiling diminishes the effective target density and generates target density fluctuations. The density fluctuations originate a false asymmetry when they are helicity correlated and a broader asymmetry distribution if they are not helicity correlated. To avoid boiling and density fluctuations, the liquid is kept in a turbulent flow so that the transverse exchange of heat is made more efficiently. The liquid target temperature is kept close to the freezing point so that there is space for temperature increasing due to the energy deposition.

The density of target nuclei per unit volume ρ_t is given by

$$\rho_t = \frac{N}{V} = \frac{N_A m/M}{V} = \frac{\rho N_A}{M} \tag{3.8}$$

where N_A is the Avogrado number, m is the total mass, M is the atomic molar mass of target and ρ is the target density (mass per unit volume). The densities ρ_t of the hydrogen and the deuterium are

$$\rho_t = \left(\frac{N}{V}\right)_{H_2} = 4.228 \cdot 10^{22} \ \ (\text{nuclei/cm}^3) \tag{3.9}$$

$$\rho_t = \left(\frac{N}{V}\right)_{D_2} = 4.857 \cdot 10^{22} \ \ (\text{nuclei/cm}^3) \tag{3.10}$$

The number of nuclei per unit volume in liquid deuterium is a factor 1.15 greater than that of liquid hydrogen.

3.8 Luminosity monitors

Definition of luminosity and its value   The luminosity is defined as the product of incident flux of particles Φ and the density per unit area of target scattering centers. The flux of incident particles can be calculated as the quotient of the beam current intensity and the electron charge I_e/e. The number of target nuclei per unit area can be calculated as the product of the density of target nuclei per unit volume ρ_t times the effective target length l_t. The luminosity is given by

$$L = \Phi \cdot \rho_t \cdot l_t \tag{3.11}$$

configuration	target	$l_t(cm)$	$L(s^{-1}cm^{-2})$
forward	ℓH_2	10.0 cm	$5.37 \cdot 10^{37}$
backward	ℓH_2	23.3 cm	$1.23 \cdot 10^{38}$
backward	ℓD_2	23.3 cm	$1.41 \cdot 10^{38}$

Physical principle   The luminosity can be measured by the Møller scattering that has the following properties:

- The Møller scattered electrons do not arrive to the calorimeter because they are scattered at small forward scattering angles, since both the incident and the scattered particles have the same mass and the energy is ultrarelativistic.

- The luminosity monitors receive both Møller scattered electrons and electrons scattered off nucleons. These processes can be distinguished by the luminosity monitors because they have different kinematics.

- The electron is a pure Dirac pointlike particle without structure (up to the present knowledge) so that the QED provides completely the Møller scattering cross section.

- At small forward angles the Møller scattering cross section is dominant compared to the cross section of the elastic scattering off the nucleon.

Luminosity monitors   The Luminosity monitors are eight water Cherenkov detectors installed at small forward angles $4° − 10°$ and optimized to detect Møller scattered electrons [22]. They measure a current that is proportional to the rate of incident particles. The luminosity of the whole process is proportional to the signal of the luminosity monitors. The measurement is relative. The luminosity is measured for every 20 ms polarization state to obtain any helicity correlated luminosity asymmetry. The absolute value of luminosity can be deduced from the known values of incident beam current and mean effective target density.

Asymmetries in luminosity monitors   The physical process to measure the luminosity should present no spin asymmetry nor azimuthal modulation.

For longitudinally polarized electrons the Mϕller scattering shows a parity violating Asymmetry (PVA) due to the axial-vector nature of electroweak interaction. The Møller scattering occurs at small forward angles where the momentum transfer is low and therefore the PVA is small, of order 10^{-9}, negligible compared to the PVA of elastic scattering off nucleons, that is of order 10^{-6}. The PVA is symmetric over the azimuthal angle.

When the electrons are transversely polarized the Møller scattering cross section presents a non-negligible two photon exchange asymmetry in the order of tens of ppm that exhibits an azimuthal modulation with $\cos \phi$. In the analysis, the luminosity must be averaged over the eight luminosity monitors, that is, averaged over the whole azimuthal angle. As the asymmetry is modulated by $\cos \phi$ it should average out.

The Møller two photon exchange asymmetry can be calculated in the framework of QED.

3.9   Beam monitors

To understand and correct the systematic uncertainties it is necessary to measure additional quantities during the experiment as beam energy, beam current intensity, beam position, beam angle and target density because they have helicity correlated differences that lead to systematic changes in the measured asymmetry.

3.9.1   Beam position monitors

At the A4 experimental halls, there are two beam position monitors (XYMO20, XYMO27). They are placed at $8.4 \ m$ and $1.2 \ m$ before the target cell. The beam

position measurement is integrated in the A4 data acquisition system. Theses measurements allow to have data about the beam state (position and angle) for both helicity states. Helicity correlated beam differences are in the order of $0.05 - 0.4\ \mu m$. They are kept so low through a feedback loop that allows the adjustment of beam position at MAMI systems.

3.9.2 Energy monitor

The energy of electrons is measured in the stage RTM3 of the microtron with the energy monitor called ENMO. The energy is determined through the time necessary for the electrons to pass through the second dipole magnet of RTM3. It is measured during the beam extraction using two high frequency cavities placed before and after the dipole magnet. The measurement is also employed to stabilize the beam energy. The injection in the RTM3 is done such that the time of travel between both cavities and thus the electron energy is kept constant.The signal corresponding to the energy is taken into account in the A4 data acquisition system. The beam stabilization allows to keep helicity correlated differences of order ~ 10 eV. This allows to reduce the false asymmetries that are due to the energy fluctuations.

3.9.3 Current intensity monitors

To measure the beam current intensity, several devices are installed along the beam transport line: intensity monitors and the Foerster probe.

The intensity monitors are HF resonant cavities that are sensitive to the beam current passing through them. The signals of two intensity monitors, PIMO08 and PIMO27, are integrated in the A4 data acquisition system. The intensity monitors are also used for the beam stabilization. Any signal deviation is corrected at the source with the help of the master oscillator of the laser diode. However the intensity monitors do not measure absolute values. The calibration of the intensity monitors is carried out with the help of the Foerster probe which allows a measurement of the absolute beam current with a precision of 1% with a bandwidth of ~ 0.1 Hz.

3.10   PbF$_2$ calorimeter

The A4 experiment is designed as a single-arm calorimeter measurement. The calorimeter detects the scattered electrons and measures their position and energy. The kinematics of the scattering is completely determined knowing the scattering energy and the scattering angle. The recoil protons are not detected.
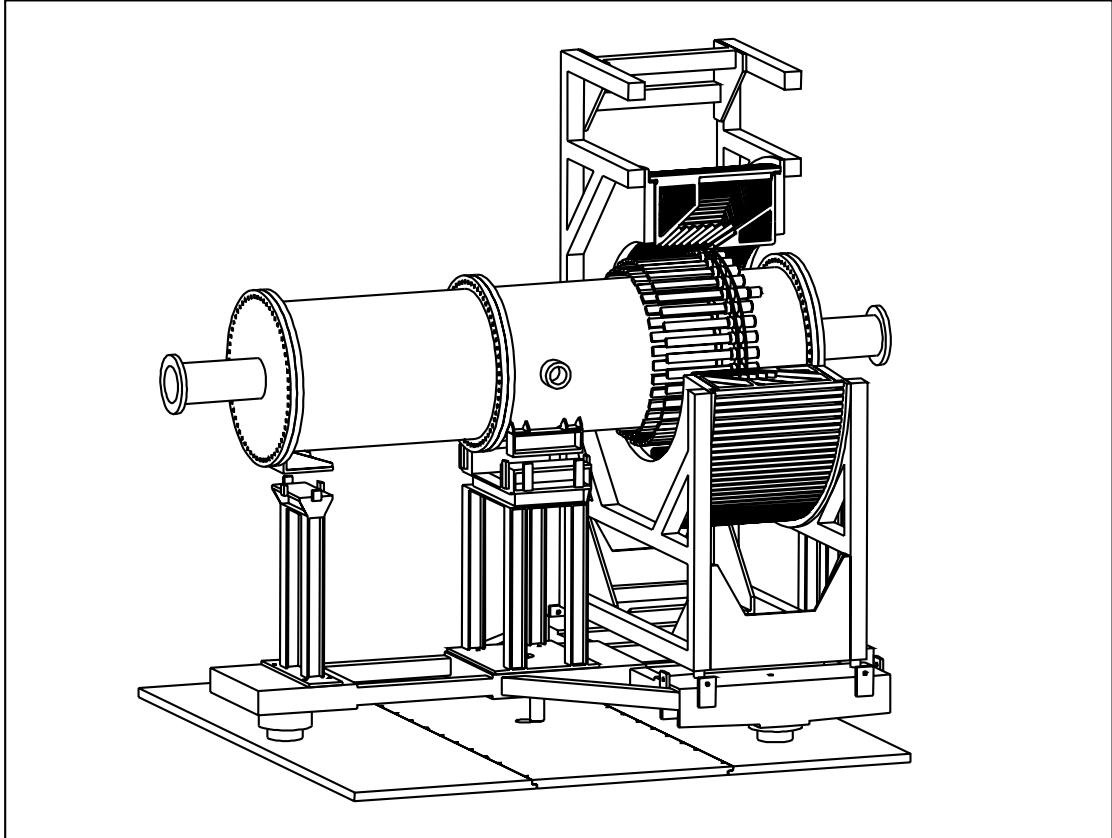
Figure 3.5. Drawing of the complete detector set up. Picture taken from [23]. In the picture one quarter of the calorimeter has been cut so that we can see the scintillators that are installed at backward angles. We can see also the scattering chamber and the window of indicates the position of the target,just in the middle of the scattering chamber. All the detector is mounted over the rotating platform so that it can rotate 180° from forward configuration to backward configuration. At forward configuration the beam enters from the left of the pictures. At backward configuration the beam enters from the right.

3.10.1   Description of demands

1. Fast detector response. A high number of detected quasielastic events N is required due to the counting statistics $\sigma(A) = \frac{1}{\sqrt{N}}$. The count rate must be high enough during a reasonable measurement time. This leads to the necessity of a fast detector response.

2. Good energy resolution. We are interested in the asymmetry of the quasielastic $e-d$-scattering cross section. The detector should have a sufficient energy resolution for a proper separation of the quasielastic events and events coming from another processes.

3. Resistance to radiation. Due to the high count rate, the detector will suffer a high radiation deposition during the measurement. The detector should maintain in time a good efficiency and a good energy resolution.

3.10.2   Set up

The A4 detector is a homogeneous fully absorbing segmented calorimeter that uses PbF$_2$ crystals. The lead fluoride is a pure Cherenkov radiator material without scintillation component and presents a high transmission of light from the visible light to the ultraviolet one. The refraction index is 1.8 for a wavelength of 400 nm. The PbF$_2$ radiation length is $X_0 = 0.93\ cm$ and its Moliere radius R_M 1.8 cm. For more details about the calorimeter consult the reference [24].

The calorimeter is symmetric with respect to the beam axis. It is arranged in 146 frames that cover the whole 2π azimuthal angle. Each frame contains 7 crystals set out vertically that constitute 7 concentric rings. The seven rings cover near 10° of scattering angle. The calorimeter consists of 1022 crystals altogether.

The calorimeter is mounted over a rotating platform that allows a rotation of detector of 180° such that the detector can operate at both forward and backward angles.

At forward configuration it covers the scattering angle 30° − 40°. At backward configuration it covers the scattering angle 140° − 150°.

The geometry of the crystals is design so that at least a 90 % of the incident energy is deposited in a 3×3 cluster of neighbouring crystals. The incident energy is deposited through a development of an electromagnetic shower. The length of the crystal corresponds to 16 radiations lengths of PbF$_2$. The transversal development of the electromagnetic shower is contained in a cluster of 9 crystals as they cover a cylinder of radius $R = 2R_M$.

The energy deposition in the crystal produces Cherenkov optical photons. At the end of thecrystal it is mounted a photomultiplier. The current is proportional

to the detected light. The current is integrated and the integral, that is the collected charge is a measure of the incident energy.

3.10.3 Advantages

The PbF$_2$ is a suitable material for our calorimeter as it fulfils the A4 demands.

- The duration of the Cherenkov pulses is very short. Therefore the calorimeter response is very fast. The integration time for a single signal is 20 ns. This allows a theoretical rate of $1/20 \cdot 10^{-9} = 50$ MHz per each crystal.

- The PbF$_2$ yields a high light output. The energy resolution of the detector is directly related to the Poisson statistical fluctuations of the number of optical photons generated by the electromagnetic cascade. The energy resolution of the detector is 3.9 %$/\sqrt{E(GeV)}$ [3]

- The PbF$_2$ presents a better resistance to radiation than other tested materials. The crystals damages can be healed illuminating it after the beamtime with blue and ultraviolet light [24].

- Symmetry. The azimuthal symmetry of the detector gives a good angular resolution. Moreover some false asymmetries like those due to helicity correlated differences in the beam positions or beam angles cancel out in the whole calorimeter due to the azimuthal symmetry. For the two photon exchange asymmetry experiment the 2π coverage in the azimuthal angle of the detector allows the detection of the cosines modulation of the asymmetry.

3.11 Electronics

The fast response of the PbF_2 calorimeter of around 20 ns needs also a fast electronics to treat the signal with a minimal dead time. Each calorimeter module has its own electronic channel so that signal can be treated in parallel. The 1022 single electronic module consists of two galvanic separated units, one analog part and one digital part. The analog part integrates the signal of the PMT, sums up analogically the signals of its 8 neighbours and provides trigger and veto information. The digital part converts the analog signals into 8 bits digital values and stores them in a histogram memory. Details can be found in [25]

3.12 Scintillators

A set of plastic scintillators are used at backward angle configuration to distinguish between charged and neutral particles. At backward angles, there is a
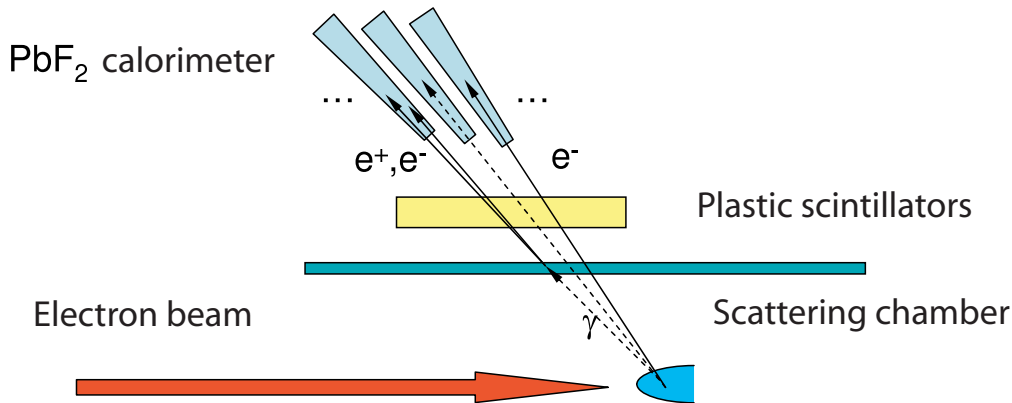
Figure 3.6. Schematic drawing of detector at backward angles. The scintillators are located between the scattering chamber and just before the calorimeter. The electrons are detected by the scintillators as they are charged particles. Photons are not detected in principle. However there is some probability that photons convert into pairs $e^+ - e^-$ such that generate a signal in the plastic scintillators. The conversion can happen in the scattering chamber walls or in the plastic scintillators themselves.

no negligible background of neutral particles that mainly come from the decay of neutral pions $\pi^0 \to 2\gamma$ of the inelastic scattering. These γ's have a detector response in the PbF$_2$ which is very similar to that of electrons since both electron and γ develop electromagnetic showers in the Cherenkov material.

The scintillators are located between the scattering chamber and just before the calorimeter crystals (see figure 3.6. Since at backward angles the rate is low they cover a range of 2 frames including the respective seven rings, that is 14 crystals altogether. Scintillators should have a symmetric arrangement due measurement requirements. They constitute a system of 72 plastic scintillators. 70 of them cover 2 frames (14 crystals) and the other 2 cover 3 frames (21 crystals).

Whenever a charged particle crosses a scintillator scintillation light is produced which is detected by a photomultiplier.

As some advantages of these scintillators we can quote: high efficiency in detecting charged particles (almost 100%), consistency between the spectral range of their radiation and the photomultipliers spectral response and finally, a very rapid decay time of the order of a few ns.

The scintillators electronic generates an additional bit in the calorimeter histogram memory such that two different kind of histograms are built: Those with coincidence of calorimeter and scintillators, which we will refer to as *coincidence spectrum*, and those where only the PbF$_2$ calorimeter produced a signal, which we will call *noncoincidence spectrum* to.

3.13   Polarimeter

The experimental asymmetry is proportional to the beam degree of polarization which has to be measured. The precision of the polarization degree measurement has an influence in the precision of the measured asymmetry.

$$A_{ph} = \frac{A_m}{P_e} \tag{3.12}$$

Two polarimeters are installed outside the A4 set up. A Møller polarimeter from the A1 collaboration provides absolute measurements of the polarization with a statistical uncertainty of $\sim 1\%$ and a systematic uncertainty of $\sim 1\%$. Those measurements are carried out usually once per week during the data taking period. A Mott polarimeter located close to the source provides relative measurements with $\sim 1\%$ statistical uncertainty which can be gauged with the A1 polarimeter. The Mott measurements are usually performed every 2 days during the data taking period. Two polarimeters are installed in the A4 set up: The Transmission Compton polarimeter and the Backscattering Compton polarimeter.

Chapter 4

Extraction of the count rates

4.1 Introduction

One of the objectives of the experiment is the measurement of the transverse spin asymmetry in the quasielastic electron scattering off deuterium.

By means of the PbF_2 calorimeter the scattered electrons are counted and their energy E' is measured. The detector allows also the determination of the scattering polar angle θ (through the knowledge of the crystal position where the electron hits the calorimeter). These variables (E', θ)[1] determine completely the scattered electron kinematics (omitting the Fermi motion of the nucleons) such that no detection of the recoil nucleon is necessary to distinguish the quasielastic scattered electrons from the inelastic scattered electrons.

In order to determine the asymmetry from the data the count rates of quasielastic events for the opposite spin states (+ and -) must be extracted from the experimentally measured energy spectra. First we will give a general description of the different experimental configurations that have been used by the A4 collaboration in order to compare the measured PbF_2 energy spectra. We say some words about the Monte Carlo simulation of the A4 detector response that is carried out to reproduce the experimental spectra so that the background can be subtracted. Finally the count rates and the cross sections obtained by this procedure will be compared with the expectations based in the theoretical calculations.

4.2 Description of the energy spectrum

The experimental configurations that have been used so far to measure both the parity violation asymmetry with longitudinal spin and the two photon exchange

---

[1]The kinematic parameters E' and θ are equivalent to Q^2 and ω, that is, the square four-momentum transfer and the transferred energy in the laboratory system

asymmetry with transverse spin are:

Config.	Target	Scattering	E (MeV)	Q^2 (GeV^2)	Detector
Forward	lH_2	Elastic	855	0.23	PbF$_2$
			570	0.11	
Backward	lH_2	Elastic	315	0.23	PbF$_2$/Scintil
	lD_2	Quasi-Elastic			

At forward angles there is a clear separation of the elastic peak from the inelastic events. The details of the extraction of the elastic events to calculate the transverse spin asymmetry can be found in the frame of two works [9] and [3].

At backward angles there is a non-negligible background of neutral particles coming from the neutral pion decay mainly $\pi^0 \to 2\gamma$. The elastic peak is not separated in the energy spectrum any more. A set of plastic scintillators are necessary to distinguish the charged and neutral particles. As explained in the section 3.12 two spectra are generated:

A **non-coincidence** spectrum when a signal occurs in the calorimeter but not in the corresponding scintillator. The non-coincidence spectrum contains the neutral particles background. An example is shown in the figure 4.6

and a **coincidence** spectrum when a signal occurs in both the calorimeter and the corresponding scintillator. The coincidence spectrum contains the charged particles events, including the (quasi)-elastic scattered electrons. The (quasi)-elastic peak can be distinguished in the coincidence spectrum. So we will extract the true events from the coincidence spectrum to calculate the asymmetry. An example of a coincidence spectrum can be seen in figure 4.7 for a H$_2$ target. In this figure the elastic peak can be recognised.

At backward angles two different targets are used, corresponding to slightly different physical processes:

- **Liquid hydrogen** ℓ-H$_2$ The process of interest is the **elastic scattering** of the electrons off the proton.

- **Liquid deuterium** ℓ-D$_2$ The process of interest is the **quasielastic scattering** of the electrons, that is, the scattering of the electron with one of the bound nucleons. The cross section of the elastic scattering with the deuteron as a whole is strongly suppressed.

Figure 4.1.   In the figure we can see the a $\mathbf{H_2}$ **target** energy spectrum measured at forward angles with a beam energy of 855 MeV. In the x-axis it is represented the signal in ADC channels (which is proportional to the energy), in the y-axis the number of counts. From right to left we can recognise the elastic peak that corresponds to 734 MeV, the pion threshold and the peak of the broad $\Delta(1232)$ resonance to the left of the pion threshold; beyond the delta resonance there is a background composed probably of γ's of the π^0 decay, at the low end of the spectrum the discriminator threshold and the pedestal at $\sim -10ADC$. The elastic peak corresponds to a definite energy, ideally the spectrum would be a Dirac delta (ignoring the radiative tail). But due to the finite energy resolution of the detector the elastic delta is convoluted with a detector response function, that is assumed to be a gaussian function.
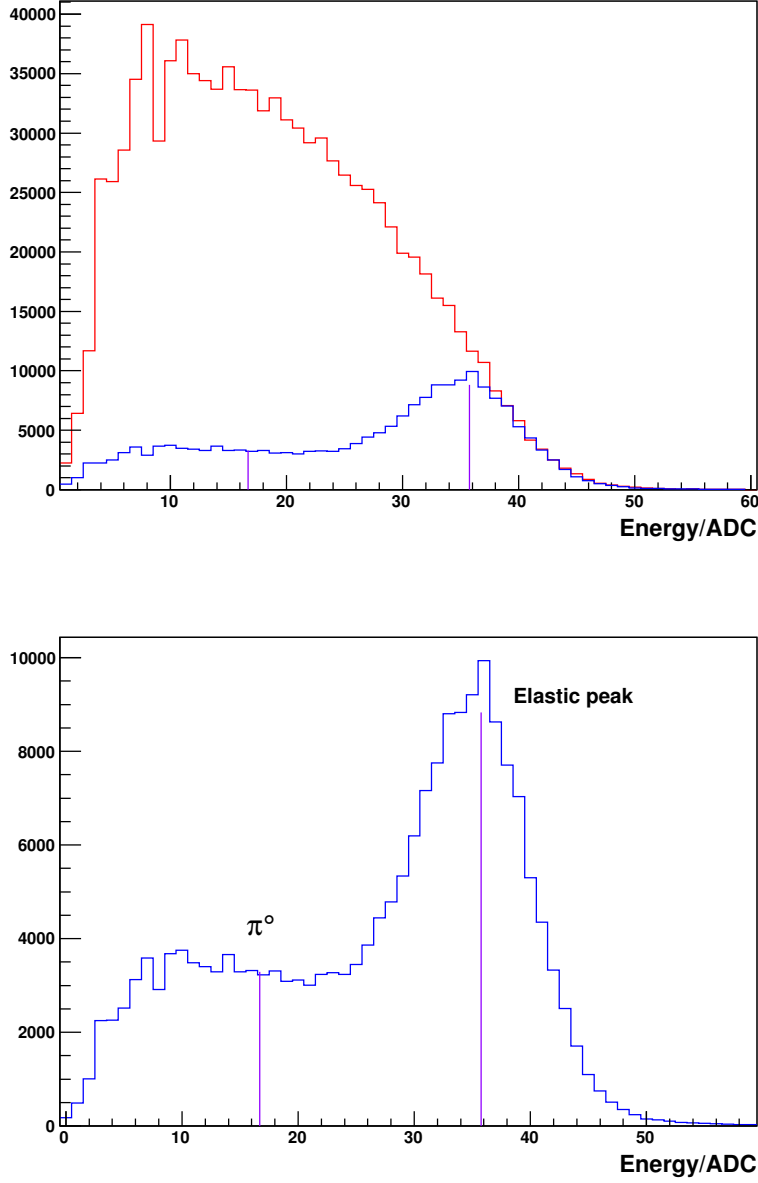
Figure 4.2. **H$_2$ target:** The upper figure shows the noncincidence histogram in red and the coincidence histogram in blue corresponding to one module, the 32, and one single run. The purple vertical lines correspond to the position of the elastic peak the second (from the left) and the position of the pion threshold the first. The noncoincidence histogram height is about a factor 10 larger than that of the coincidence histogram. The elastic peak is isolated in the coincidence histogram. The coincidence histogram is shown in the lower figure in a larger scale. The flat region between the elastic peak left slope and the pion threshold probably corresponds to the neutral background due to the γ's that leave a signal in the scintillators.
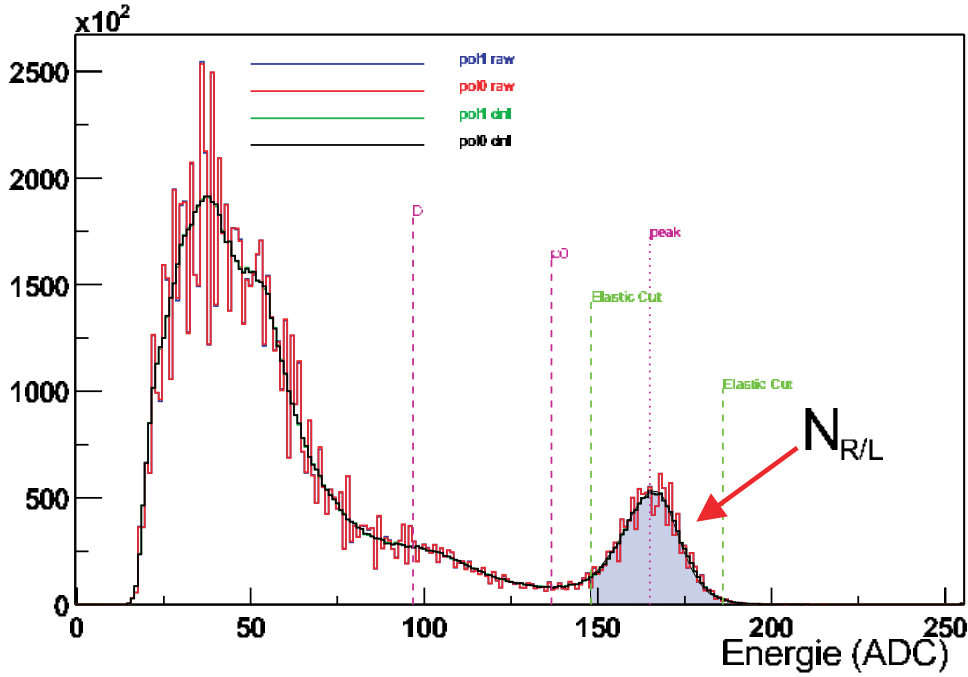
4.2.1 Spectrum at forward angle

In the figure 4.1 we can see the an energy spectrum measured at forward angles with a beam energy of 855 MeV. In the x-axis it is represented the signal in ADC channels (which is proportional to the energy). From right to left we can recognise the elastic peak, the pion threshold and the peak of the broad $\Delta(1232)$ resonance beyond the pion threshold. The elastic peak corresponds to a definite energy, ideally the spectrum would be a Dirac delta. But due to the finite energy resolution of the detector the elastic delta is convoluted with a detector response function, that is assumed to be a gaussian function.

The elastic peak is clearly isolated as it is shown in the figure 4.1. The elastic and inelastic scattering events are energetically separated. The pion threshold line is thus a point of reference to delimit the elastic peak region. Nevertheless as the detector presents a finite energy resolution there is some degree of overlap between elastic and inelastic events. So it becomes necessary to choose convenient cuts to delimit the elastic peak region.
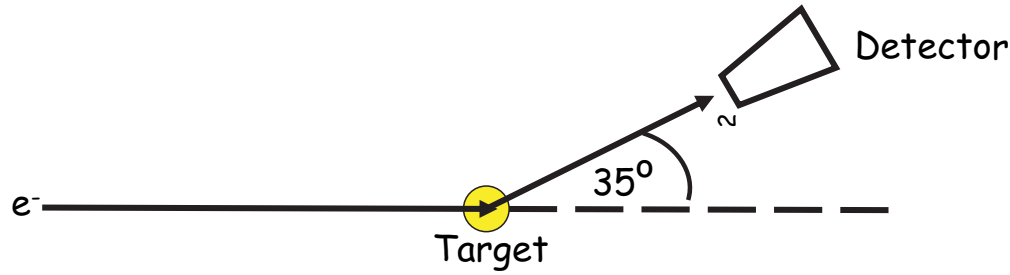
Figure 4.3. Schematic drawing of the forward angle configuration.

4.2.2 Backward angle coincidence spectrum

Two features of the backward angle coincidence spectrum make the choice of the cuts defining the elastic peak region more complicated.

- For the experiment at backward angles the beam energy is 315.1 MeV, lower than the beam energies corresponding to the forward angle configuration. Therefore the scattered electron energy and the pion threshold energy are lower than those at forward angles. The energy resolution of the detector for the backward energy is thus larger because its dependence on energy is $\Delta E/E = 3.5\%/\sqrt{E(GeV)}$ [3]. A higher degree of mixing between the (quasi)elastic scattered electrons and the inelastic scattered electron can be expected.

- Despite of being the γ's background eliminated by means of the scintillators some photons may still produce a signal in the scintillators and be recorded as coincidence events. This happens through the interaction of photons with matter i.e. pair production, Compton scattering and photoelectric effect that occur in the materials between the scattering chamber and the plastic scintillators: the scattering chamber walls and the scintillators themselves. As a consequence there is some amount of background in the coincidence spectrum, even in the region of the elastic peak.
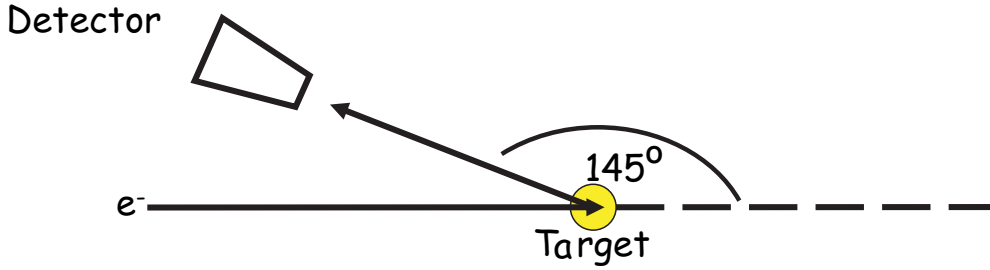
Figure 4.4. Schematic drawing of the backward angle configuration.

4.2.3   Backward coincidence spectrum for D_2

At A4 experiment energy range the electron scattering process that dominates is not the elastic scattering in the deuteron as a whole but the so called quasielastic scattering off one of the deuteron's nuclear bound nucleons (proton or neutron). According to the impulse approximation the scattering with the nucleon occurs as if it were free but assuming it has certain momentum distribution given by the deuterium wave function in the momentum space. The other nucleon acts as a spectator. This movement of the nucleon inside the nucleus is known as Fermi motion. The Fermi motion of the bound nucleons leads to a smearing of the scattered electron energy and therefore to an effective increase of the energy resolution. The smearing effect can be accounted adding quadratically a constant term (no dependent on the energy) to the energy resolution give by 4.6. Since the scattering off the proton does not present the smearing in the energy it can be assumed that the energy resolution for the scattering off D_2 equals the energy resolution for the scattering off H_2 plus an additional term that accounts for the smearing in energy, added quadratically, that is:

$$\left(\frac{\Delta E}{E}\right)^2_{D_2} = \left(\frac{\Delta E}{E}\right)^2_{H_2} + \left(\frac{c_F}{E}\right)^2 \tag{4.1}$$
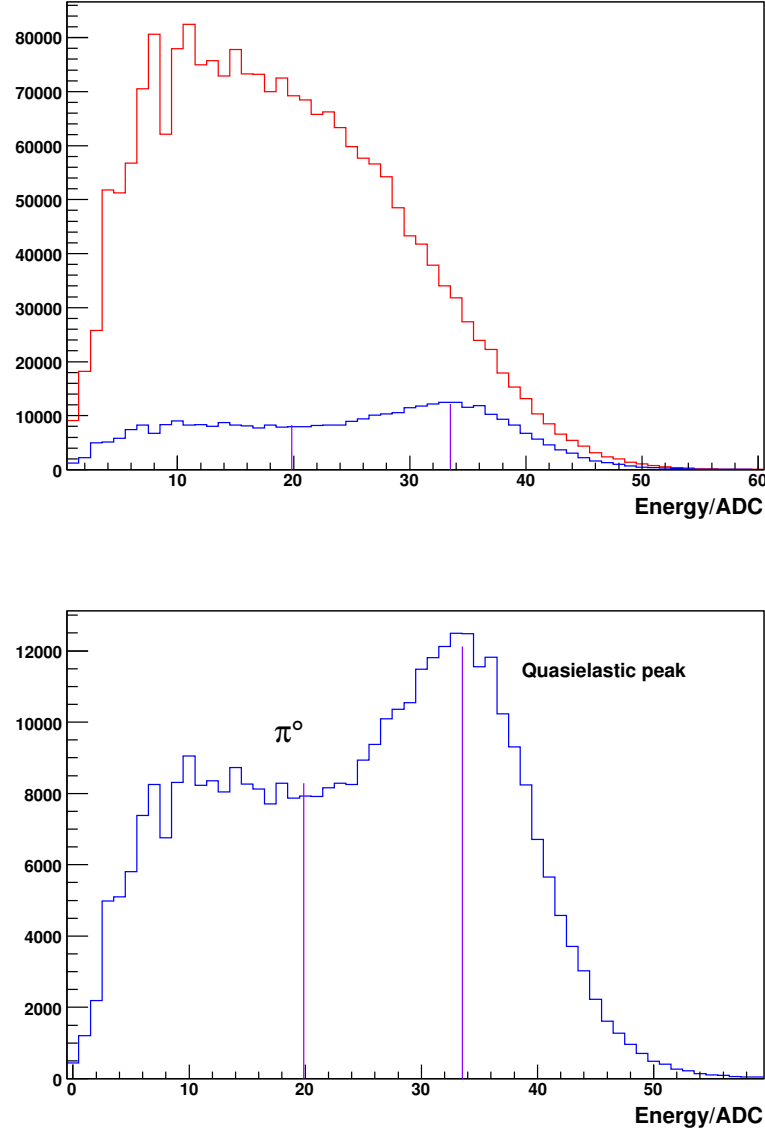
Figure 4.5. **D_2 target:** In the upper panel the noncoincidence histogram in red and the coincidence histogram in blue are shown. In the lower panel the coincidence histogram is shown with a larger scale. The purple vertical lines represent the pion threshold the first (from the left) and the quasielastic peak the second. One can observe that the height of the quasielastic peak is greater than that of the elastic peak in the H_2 spectrum. The quasielastic peak is broader than the elastic peak. One can observe also that the quasielastic peak position is shifted to lower energies about two adc channels with respect to the position of the elastic peak. On the other hand, the flat region between the quasielastic left slope and the pion threshold is higher with respect to the quasielastic peak than the corresponding flat region in the H_2 spectrum with respect to the elastic peak. That is, the dilution background degree is larger in the case of the deuterium.

where c_F/E is the constant term that accounts for the energy smearing due to the Fermi motion.

Moreover, the electroproduction of pions on the deuterium occurs both incoherently and coherently, that is, the pion is produced on the nucleon as if it were a free particle but also it can be produced on the deuteron as a whole coherently. As we will see later, this means that the pion threshold energy for the deuterium is higher than the threshold for the hydrogen. Therefore the mixing of inelastic and elastic events will be larger.

4.3 Extraction of the quasielastic events

4.3.1 Separation of elastic and inelastic events

Separation of inelastic events from elastic ones is necessary, since they have different physical asymmetries. These processes are separated through the energy measurement as they have different scattering energies. The unique electron energy loss during the elastic scattering is due to the nucleon recoil. In the inelastic scattering, on the other side, the electron delivers more energy for the creation of extra particles.

Conservation of energy and momentum determines the energy of the elastic scattered electron in the laboratory system:

$$E' = \frac{E}{1 + \dfrac{2E}{M}\sin^2\dfrac{\theta_e}{2}} \qquad (m_e = 0) \tag{4.2}$$

where E' is the energy of the elastic scattered electron, E is the energy of the incident electron, M is the nucleon mass and θ_e is the polar scattering angle of the electron in the laboratory system.

The energy of the inelastic scattered electron when it has excited a state of invariant mass W on the nucleon is:

$$E_{Thres}^{\pi^0} = \frac{E - \dfrac{W^2 - M^2}{2M}}{1 + \dfrac{2E}{M}\sin^2\dfrac{\theta_e}{2}} = E' \cdot \left(1 - \frac{W^2 - M^2}{2ME}\right) \tag{4.3}$$

In the elastic scattering the invariant mass equals the nucleon mass $W^2 = M^2$. At the pion threshold the invariant mass equals the nucleon mass plus the pion mass $W^2 = (M + m_\pi)^2$.

In the table below the relevant kinematic parameters of the different kinematic configurations used in the A4 experiment are shown. One can see the kinematic

conditions at forward angle with hydrogen target at two different energies corresponding to different squared four-momentum transfer, and the backward angle configuration with the squared four-momentum transfer $Q^2 = 0.23$ GeV^2 equal to that of one of the forward configurations. At backward angle the A4 collaboration uses liquid hydrogen as well as liquid deuterium as targets.

θ	E MeV	Q^2 GeV^2	E' MeV	$E_{Thres}^{\pi^0}$ MeV	target
$30° - 40°$	855	0.23	734	605	H_2
$30° - 40°$	570	0.11	514	378	H_2
$140° - 150°$	315	0.23	195	88	H_2
$140° - 150°$	315	0.23	195	100	D_2

4.3.2   Fit of elastic peak and energy calibration

As the (quasi)elastic peak is clearly separated (at forward angle in the energy spectrum provided by the calorimeter, at backward angle in the coincidence energy spectrum) a function can be found to fit the peak.

The most reasonable function to try with is a gaussian. However, taking into account the radiative corrections to the elastic scattering cross section, it is clear that some elastic scattered electrons lose energy through the emission of bremsstrahlung photons. Therefore the elastic peak is not symmetric because of the presence of a radiative tail.

The radiative tail is considered in the fitting by including an exponential function in the left side. The fitting function that is employed in the A4 analysis is then [3], [24].

$$f(x) = \begin{cases} A \exp\left[-\dfrac{(x-\mu)^2}{2\sigma_R^2}\right] & x \geq \mu \\ A\left\{\exp\left[-\dfrac{(x-\mu)^2}{2\sigma_L^2}\right] + \exp\left[\dfrac{x-\mu}{\lambda}\right]\left(1 - \exp\left[\dfrac{-(x-\mu)^2}{2\sigma_L^2}\right]\right)\right\} & x \leq \mu \end{cases}$$

From the fit parameters of the right gaussian curve we can estimate the energy resolution at the elastic peak energy.

$$\frac{\Delta E}{E} = \frac{\sigma_R}{\mu - p} \tag{4.4}$$

where p is the pedestal of the calorimeter module.

As the signal is linear with the energy we can calibrate the ADC for each Medusa module using the energy of the elastic peak and the ADC channel given by the fit parameter μ. The offset is the pedestal of the module.

$$E' = m \cdot (x_{ADC} - p) \tag{4.5}$$

Once the ADC is calibrated we can find the pion threshold channel by using the pion threshold energy calculated with the equation 4.3. And now we can calculate also the energy resolution at the pion threshold energy.

4.3.3   Energy resolution

Energy resolution at the elastic peak

The relative energy resolution is parametrized with three parameter as follows:

$$\frac{\Delta E}{E} = \frac{c_1}{E(GeV)} \oplus \frac{c_s}{\sqrt{E(GeV)}} \oplus c_3 \tag{4.6}$$

where c_1 is the energy independent contribution of the electronic noise, $c_1 = 0.6$ %. c_s is the statistical contribution to the energy resolution, $c_s = 4.69$ % [3], and c_3 is related to an energy proportional term that takes into account signal losses when the volume in which the energy deposition would be developed does not fit in the detector size, $c_3 = 0.4$ %.

For the elastic scattered electron energy of 0.195 GeV one can calculate the relative energy resolution at the elastic peak: $\Delta E/E = 11$ %. On the other hand the energy resolution at the elastic peak for every calorimeter module is calculated from the experimental energy spectrum using the equation 4.4. They are statistically distributed and the average relative energy resolution corresponds to $\Delta E/E|_{exp} = 11$ %.

Energy resolution at the quasielastic peak

From parameters obtained fitting the quasielastic peak we can estimate the energy resolution at the quasielastic peak of deuterium. Since contributions to energy resolution given by the statistical term, noise and loss of events can be supposed to be equal for deuterium, the quadratic difference is a measure of the energy broadening due to Fermi motion.

The quasielastic peak corresponding to the energy spectrum for the deuterium target is also fitted to the function 4.3.2. The fit parameters are used to calculate the relative energy resolution at the quasieleastic peak through the relation 4.4. The energy resolution calculated for every module is also distributed with an average greater that that of hydrogen data. The average relative energy resolution at the quasielastic peak is $\Delta E/E|_{exp} = 16.7$ %

Assuming that the only difference between the energy resolution shown by the elastic peak (hydrogen data) and the quasielastic peak (deuterium data) is due to

the energy smearing this term can be calculated through the quadratic relation 4.1

From the experimental values of the relative energy resolution for both hydrogen and deuterium data and using the energy 0.195 GeV for the elastic scattered electrons the smearing parameter c_F (where the F comes from the Fermi motion) is calculated to be:

$$c_F \approx 24 \ MeV \tag{4.7}$$

On the other hand the energy smearing can be estimated theoretically using the known Fermi momentum for the deuteron, given by $p_F = 55 \ MeV$. The energy smearing can be related to the Fermi momentum through the relativistic expression $E^2 = p^2 + m^2$ taking differentials:

$$EdE = pdp \tag{4.8}$$

Identifying the energy difference with the energy smearing $dE = \delta\omega$ and the momentum difference with the Fermi momentum $dp = p_F$ one obtains:

$$\delta\omega = \frac{qp_F}{\sqrt{M^2 + q^2}} \tag{4.9}$$

where the momentum of the nucleon has been identified with the tri-momentum transfer q. The tri-momentum transfer is related to the energy transfer $\delta\omega$ and the four-momentum transfer Q as follows:

$$Q^2 = q^2 - \omega^2 \tag{4.10}$$

The energy transfer in the elastic scattering can be calculated through the relation:

$$\omega = \frac{Q^2}{2M} = 122 \ \text{MeV} \tag{4.11}$$

where M is the nucleon mass $M = 939$ MeV. It turns out that $q = 495$ MeV/c.

$$\delta\omega = 25.6 \ \text{MeV} \tag{4.12}$$

This value of energy smearing is very close to that estimated using the quasielastic peak fit parameters.

4.3.4   Definition of cuts

In order to extract the number of elastic events we should determine the boundaries fo the elastic peak region. To do so both a lower cut and an upper cut in energy are defined. The upper cut has the function of excluding the pile-up events with more energy than that of a single event. The lower cut intends to separate the elastic events from the inelastic events. Some degree of background in is unavoidable, especially at backward angles, therefore we must find an optimum place in the ADC channel axis to locate the lower cut so that the systematic errors of the asymmetry measurement are minimized. The choice of the lower cut will be discussed in detail in the chapter 5.

The lower cut is taken to the right of the pion threshold. The distance of the lower cut to the pion threshold is usually expressed in terms of k times the energy resolution at the pion threshold energy. That is

$$E_{lowcut} = E_{Thres}^{\pi^0} + k \cdot \Delta E_{Thres} \tag{4.13}$$

At forward angle measurement the value $k = 1.6$ was chosen. At backward angles we expect higher values of the cut k.

4.4   Monte Carlo simulation of the energy spectrum

In the A4 collaboration experiment a Monte Carlo simulation of the detector response is carried out [26]. The simulation is able to reproduce the experimentally observed energy spectra. We are interested here in the simulation at backward angles for both hydrogen and deuterium target.

The simulation uses Geant4[2], an object oriented programming toolkit for simulating the passage of radiation through matter. Geant4 uses Monte Carlo methods for tracking particles.

The simulation carried out for the hydrogen target is discussed here. The results can be easily transferred to the deuterium case.

4.4.1   Physical processes and detector response

The simulation can be divided in two parts: the physical processes occurring during the interaction in the target and the detector response.

---

[2]http://www.geant4.org/geant4/

Interaction in the target. The beam electrons interact with the materials of the target cell and the target and therefore suffer an energy loss through ionization and bremsstrahlung. As a consequence, instead of having a beam with a definite energy, the beam electrons energy has a certain probability distribution function, known as straggling function.

The main particles and physical processes that occur during the interaction with the target are:

- Elastic scattering of the electron

  $$\vec{e}^- + p \rightarrow e^- + p$$

- Inelastic scattering of the electron with the production of either a charged pion or a neutral pion. Most of the pions are produced through the excitation of the $\Delta(1232)$ resonance with a very short lifetime that decays producing both a nucleon and a pion. The creation of pions through the inelastic scattering of electrons is called electroproduction.

  $$\vec{e}^- + p \rightarrow e^- + p + \pi^0$$
  $$\vec{e}^- + p \rightarrow e^- + n + \pi^+$$
  $$\vec{e}^- + p \rightarrow e^- + \Delta(1232) \rightarrow e^- + p + \pi^0$$
  $$\vec{e}^- + p \rightarrow e^- + \Delta(1232) \rightarrow e^- + n + \pi^+$$

- Neutral pions generated by photoproduction, through bremstrahlung photons. That is, beam electrons radiate γ's when passing through matter via bemstrahlung. These γ's have certain probability to produce pions. This process is called pion photoproduction.

  $$\vec{e}^- \rightarrow e^- + \gamma \Rightarrow \gamma + p \rightarrow p + \pi^0$$

- γ's produced by the neutral pion decay.

  $$\pi^0 \rightarrow 2\gamma$$

Detector response Before reaching the calorimeter the charged particles lose energy as they pass through the materials between the target cell and the calorimeter like the scattering chamber walls and the plastic scintillators.

Once in the calorimeter the scattered electrons and the γ's develop electromagnetic showers. The fast particles of the electromagnetic showers are the responsible for the production of Cherenkov radiation. The Cherenkov radiation is transmitted through the calorimeter crystal and detected by the photomultipliers. The amount of Cherenkov optical photons is proportional to the incoming particle energy.

4.4.2 Non-coincidence and coincidence spectra

The simulation must reproduce both the non-coincidence spectrum and the coincidence spectrum.

The **noncoincidence spectrum** consists of the neutral particles background that do not produce a signal in the scintillators. It is explained mostly by the decay of neutral pions into photons $\pi^0 \to 2\gamma$. The simulated spectrum generated by the neutral pion decay process is shown in the figure 4.6

The beam energy 315 MeV is sufficient to reach the pion production threshold. During the inelastic scattering of a beam electron the production of either a neutral pion or a charged pion is induced. Most of the pions are produced through the excitation and decay of the $\Delta(1232)$ resonance. The π^0 mean life is 8.4×10^{-17} s, since it decays via the electromagnetic interaction, and it is so short, even considering the relativistic γ factor [3], that the π^0's do not reach the detector, which is located at a distance of about 1 m from the target cell, but they decay into γ's. These γ's have an energy comparable to that of the scattered electrons, as they obtain energy also from the rest mass of the π^0. The γ's arrive to the calorimeter where they develop electromagnetic cascades. The calorimeter is not able to distinguish between the γ's of the π^0 decay and the scattered electrons. On the other hand these γ's do not produce a signal in the plastic scintillators and therefore they are stored in the noncoincidence spectrum.

Pion	Mass (MeV)	Lifetime (s)	Decay modes
$\pi^\pm$	139.579	$2.60 \cdot 10^{-8}$	$\mu\nu_\mu(100\%)$
π^0	134.97	$8.4 \cdot 10^{-17}$	$\gamma\gamma(98\%)$
			$\gamma e^+ e^-(2\%)$

Values taken from [20]

On the other hand charged pions are also produced. They are generated in a similar amount as the neutral pions but their contribution to the spectrum is much less and it occurs mainly at low energies of the experimental spectrum. The charged pions have a large lifetime since their decay modes occur via the weak interaction. The $\pi^\pm$ mean life is $2.60 \cdot 10^{-8}$ s = 26 ns so that most of them arrive to the calorimeter before the decay occurs [4]. In the calorimeter the $\pi^\pm$'s lose energy until they stay at rest since they are heavy particles [5]. The main decay mode of the

---

[3]The kinetic energy of the pions would be at most of order of 100 MeV. The relativistic factor $\gamma = 1 + \dfrac{E_K^\pi}{m_\pi} \approx 2$.

[4]With a kinetic energy of order of 100 MeV a pion has a relativistic factor $\gamma \sim 2$, that is $v \sim 0.87c$ and the time to reach the calorimeter, at a distance of ~ 1 m is about 4 ns

[5]The calorimeter is a Cherenkov detector. So for low velocities the signal is no longer linear with the energy.
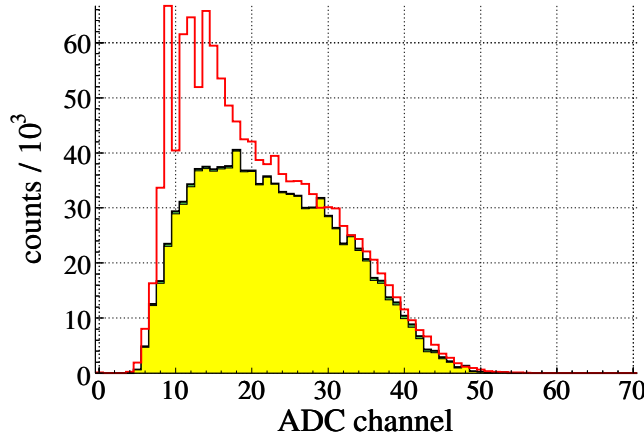
Figure 4.6. The simulated noncoincidence spectrum for the **H$_2$ target** is shown in yellow. This simulation includes only the contribution of the $\pi^0 \to 2\gamma$, the neutral pions being those originated in the target by both electroproduction and photoproduction. The histogram in red is the experimentally observed noncoincidence spectrum. The agreement of the simulated spectrum with the experimentally observed is very good at the high energies. For the lower energies one can observe a discrepancy between the simulated and the experimentally observed spectrum. This region probably can be explained by the contribution of the decay products of the charged pions produced by the beam electrons in the target. Figure taken from [27]
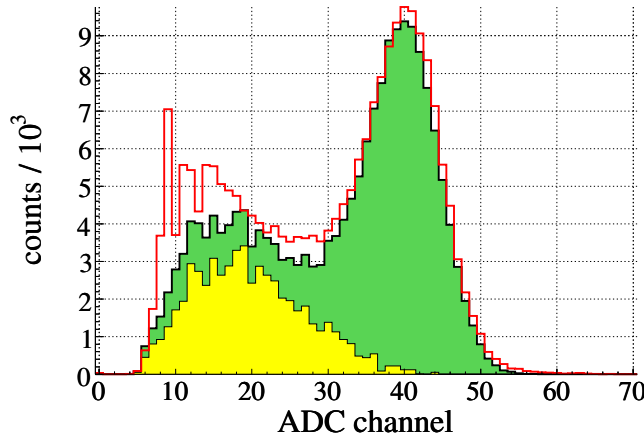
Figure 4.7. The simulated contribution of both the elastically and inelastically scattered electrons to the coincidence spectrum for the **H$_2$ target** is shown in green. The yellow region corresponds to the simulation of the contribution of the $\pi^0 \to 2\gamma$ to the coincidence spectrum. The γ's deliver their energy to electrons through processes like pair production, Compton scattering or photoelectric effect during the interaction with the materials between the target cell and the scintillators, included. By this way the γ's of the π^0 decay contribute to the coincidence spectrum. The histogram in red corresponds to the experimentally observed coincidence spectrum. The agreement is good in the elastic peak. The disagreement is greater for low energies. This disagreement is due to the lack of the contribution of the decay products of the charged pions as in the noncoincidence case. Figure taken from [27]

charged pions is the decay into muons, which have a large mass $m_\mu \approx 105$ MeV. Finally the muon $\mu^\pm$ decays into an electron (or positron) and a neutrino. If the electron produces a signal it is not in coincidence with the scintillator signal so that it is stored in the noncoincidence histogram. For all these reasons the contribution of the charged pions is only visible in the low energy part of the noncoincidence spectrum.

The simulated **coincidence spectrum** is composed of the elastic scattered electrons and the inelastically scattered electrons corresponding to the pion production. The coincidence spectrum incorporates as well the γ's of the π^0 decay that leave a signal in the plastic scintillators as they deliver totally or partially their energy to electrons during the interaction of the γ's with the materials located between the target cell and the plastic scintillators: the scattering chamber walls and the plastic scintillators themselves. This effect might happen through the following processes: a γ converts into a electron-positron pair, suffers Compton scattering or photoelectric effect. Further the photon itself or the electron delivers its energy in the calorimeter producing thus a signal in both a plastic scintillator and the calorimeter so that this event is recorded in the coincidence spectrum (see the figure 4.7).

4.5   Model for background subtraction

The simulation of the detector response to the neutral background of γ's suggests using a simple model to subtract the neutral background mixed in the coincidence spectrum. The idea is using the non-coincidence spectrum $N_{non}(x)$ to estimate the amount of neutral background $N_{bk}(x)$ present in the coincidence spectrum in each bin x. The model has two basic parameters:

$$N_{bk}(x) = \epsilon \cdot N_{non}(x + \delta) \tag{4.14}$$

- A scaling factor ϵ: It is related to the probability of conversion of γ's into $e^- - e^+$ pairs. Therefore we must multiply the noncoincidence spectrum by this scaling factor ϵ to estimate how many gamma photons produce a signal in the scintillators and therefore how many are present in the coincidence spectrum.

- A shift δ in the energy: It takes into account the difference in energy loss between electrons that produce a signal in the scintillators and photons that do not produce a signal in the scintillators.

The parameters of the model ϵ and δ can be determined either by the simulation or by the following simple estimation: The dominant process by which the γ's
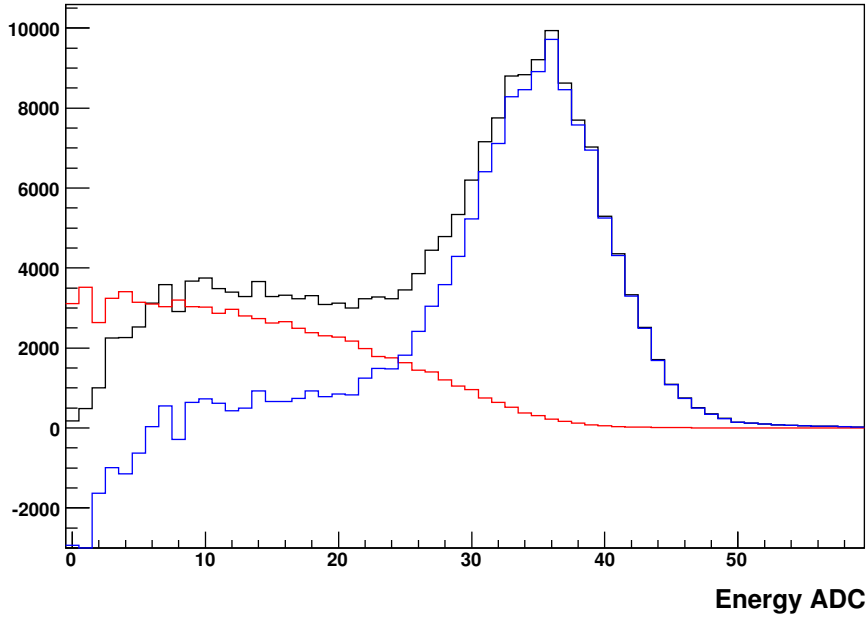
Figure 4.8. H_2 **target:**The black histogram corresponds to the coincidence spectrum for hydrogen. The red histogram is obtained from the noncoincidence histogram applying the scaling and shifting model. It is an estimation of the background in the coincidence spectrum. The histogram in blue is the difference between the coincidence histogram and the histogram of the background present in the coincidence spectrum. The blue histogram represents the true elastic events. One can observe that at the left of the elastic peak the number of true events is not zero. This is correct because the histogram of the true events must contain the radiative tail. For the lower energy part of the energy spectrum, though, the histogram of the true events becomes negative showing the limitations of the scaling and shifting model.
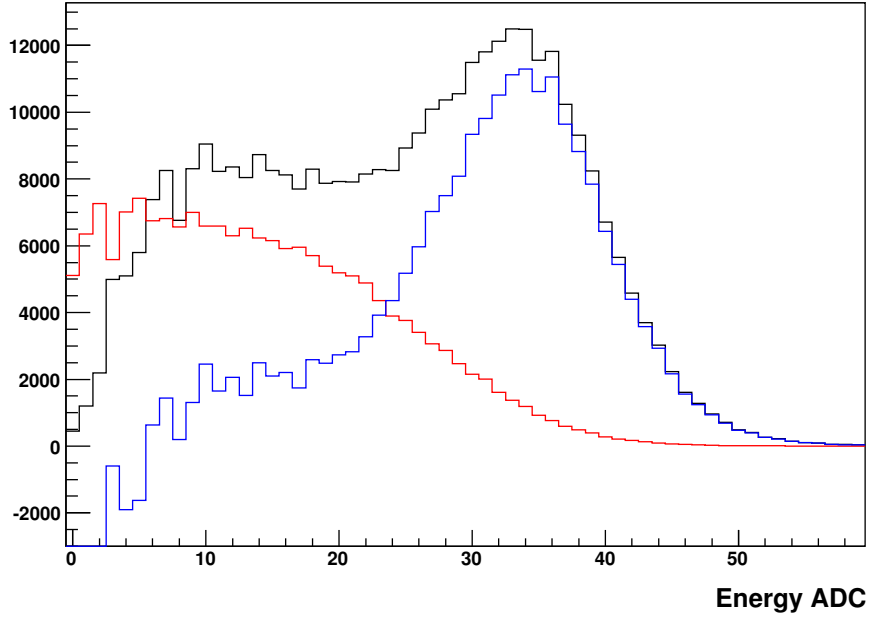
Figure 4.9. **D_2 target:** The black histogram corresponds to the coincidence spectrum for hydrogen. The red histogram is obtained from the noncoincidence histogram applying the scaling and shifting model. It is an estimation of the background in the coincidence spectrum. The histogram in blue is the difference between the coincidence histogram and the coincidence background histogram. The blue histogram represents the true quasielastic events.One can observe that at the left of the quasielastic peak the number of true events is not zero. This is correct because the histogram of the true events must contain the radiative tail. For the lower energy part of the energy spectrum, though, the histogram of the true events becomes negative showing the limitations of the scaling and shifting model. One can observe that the degree of neutral background mixed in the quasielastic peak is larger than at the elastic peak.

deliver energy to electrons and therefore generate a signal in the scintillators is the pair production. The pair production probability in the scattering chamber walls and in the scintillators can be estimated. The probability per unit length of pair production is the product of the pair production cross section and the material density of atoms. It is equal by definition to the inverse of the pair conversion length that is related with the material radiation length [28].

$$p/l = N\sigma = \frac{1}{\lambda_{pair}} \simeq \frac{7}{9}\frac{1}{X_0} \qquad (4.15)$$

where p/l refers to the probability per unit length, σ is the pair production cross section, N is the density of atoms in the material, λ_{pair} is the pair conversion length and X_0 is the material radiation length. This formula defines a probability per unit length. Now we consider the Aluminium scattering chamber wall with a thickness of 5 mm in the trajectory of electrons and the plastic scintillators whose thickness is 2 cm. The aluminium radiation length is $X_0^{Al} = 8.9$ cm [20] and the plastic scintillators radiation length is $X_0^{PlS} = 42.5$ [20].

$$p = N\sigma\Delta x \sim \frac{7}{9}\frac{\Delta x}{X_0} = \frac{7}{9}\left(\frac{0.5/\sin 35°}{8.9} + \frac{2/\sin 35°}{42.5} \right) = 7.6 \text{ } \% + 6.4 \text{ } \% = 14 \text{ } \%$$
$$(4.16)$$

However if the pair is produced at the end of the passage through the plastic scintillator no signal will be generated in the scintillator. Therefore the probability for pair production in the materials between the scattering chamber and the plastic scintillator is overestimated. The estimation of the probability that the γ's produce a signal in the scintillators given by the scintillators is $\epsilon \approx 0.10$ [29]

The charged particles suffer an energy loss by ionization and radiation as they pass through the scintillators material and through the materials between the target and the scintillators. That means that there is a shift between coincidence and noncoincidence histograms provided photons do not lose so much energy. We can estimate the energy loss of the electrons as they cross the plastic scintillators and the scattering chamber wall.

$$(\Delta E)_{loss} = \rho\left(\frac{dE}{dx}\right)\left(\frac{\Delta x}{\sin\theta_e}\right) \qquad (4.17)$$

where ρ is the density of the material in g/cm^3, dE/dx is the stopping power in MeV·g/cm^2, Δx is the width of the material and θ_e is the scattering angle.

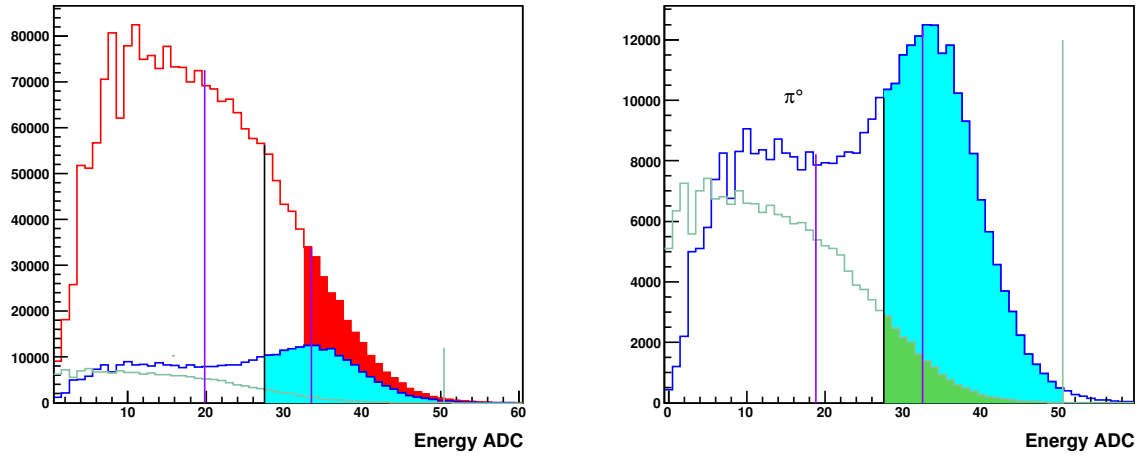| Material	$\rho(g/cm^3)$	$\frac{dE}{dx}$(ion)	$\frac{dE}{dx}$(rad)	Δx (cm)	$(\Delta E)_{loss}$
Al	2.70	1.892	6.909	0.5	20.65
Pl. Scint.	1.032	2.198	3.710	2.0	21.29

Figure 4.10. The left panel contains the noncoincidence spectrum in red and the coincidence spectrum in blue. The purple vertical lines represent the pion threshold and the quasielastic peak. The black vertical line represents the lower cut in energy and the green vertical line the upper cut. Both lines delimit the quasielastic peak region. The noncoincidence histogram is integrated between the cuts corresponding to the quasielastic peak after applying to them a shift according to the model for the subtraction of background. The integrated region appear in red. The coincidence histogram is integrated between the lower and the upper cut. This integral is coloured in blue. The right panel contains the coincidence histogram in a greater scale. The green histogram is obtained from the noncoincidence histogram applying a shift and a scaling factor. The integrated region in green represents the background in the coincidence spectrum.

where the stopping power is given in MeV·g/cm^2 and corresponds to the energy 180 MeV. The densities are taken from [20] and the stopping powers are given by [30]. The electron energy loss at these materials is overestimated because some γ's emitted by the electrons are not absorbed and arrive to the detector since the γ's are emitted in a narrow cone in the direction of the scattered electron.

The shift in the energy is estimated by the simulation to be $\delta \approx 35$ MeV according to [29].

In the analysis of the data the values of ϵ and δ provided by the simulation [29] are used.

4.6 Application of the model to extract the quasielastic events

The neutral background in the coincidence spectrum can be estimated from the noncoincidence spectrum applying to it the shift δ in energy and multiplying by the conversion factor ϵ. Let $y(x)$ be the content of the coincidence background histogram for the energy x. Let $h(x)$ be the content of the noncoincidence histogram at the energy x. Then:

$$y(x) = \epsilon \cdot h(x + \delta) \tag{4.18}$$

In the figures 4.8 and 4.9 we can see for the H_2 target and the D_2 target, respectively, the coincidence histogram in black. In red we can see the coincidence background histogram after applying the scaling and the shift to the noncoincidence histogram. The histogram in blue is the subtraction of the background from the coincidence histogram and corresponds to the true elastic events (for the H_2 target) or to the quasielastic events (for the D_2 target) .

In order to extract the rate of (quasi)elastic events the (quasi)elastic peak must be integrated between the lower cut and the upper cut. The best choice of the lower cut is discussed in the chapter 5. The coincidence histogram should be integrated as it is shown in the figure 4.10, the blue region in both panels. The integral for both polarization states is calculated separately, calling them N_{co}^{+} and N_{co}^{-}.

$$N_{co}^{\pm} = \sum_{i=low}^{up} N_{i,co}^{\pm} \tag{4.19}$$

where low represents the ADC channel of the lower cut in energy and up has an analog meaning for the upper cut in energy, the $N_{i,co}^{\pm}$ represents the number of counts for the ADC channel i of the coincidence histogram.

In order to calculate the background dilution the integral of the non-coincidence histogram is performed. The shift is applied by performing the integral with the shifted lower and upper cuts. The shifted integrated region can be seen in the first panel of the figure 4.10 in red. The integrals of the noncoincidence spectrum are performed for both polarization states separately, calling them N_{non}^{+} and N_{non}^{-}.

$$N_{non}^{\pm} = \sum_{i=low+\delta}^{up+\delta} N_{i,non}^{\pm} \tag{4.20}$$

where low and up have the same meaning as in the last equation, the $N_{i,non}^{\pm}$ represents the number of counts for the ADC channel i of the noncoincidence histogram and δ is the shift in energy that is applied to the lower and the upper cut.

Afterwards the nonconcidence number of counts $N_{non}^{\pm}$ is multiplied by the conversion factor ϵ to obtain the amount of background in the (quasi)elastic peak. This amount can be seen in both panels of the figure 4.10 in green.

Now we can calculate the number of estimated true (quasi)elastic counts subtracting the background events and the coincidence events, that is:

$$N_{good}^{\pm} = N_{co}^{\pm} - \epsilon N_{non}^{\pm} \tag{4.21}$$

4.7   Rate estimation and the experimentally observed

After extracting the count rate of quasielastic events from the energy spectrum the experimentally observed rates and hence the cross section shall be compared here with the predicted rates from the theoretical cross section in order to check that the physical processes agree with what is expected. The comparisons are based, throughout, on the assumption that the Rosenbluth cross section is a good first approximation for the elastic scattering. Moreover for the quasielastic scattering on the deuteron we resort to the static approximation in which the deuteron is modelized as two free nucleons (proton and neutron) at rest. Therefore the quasielastic scattering cross section is the sum of the elastic scattering cross sections for both nucleons.

$$\left.\frac{d\sigma}{d\Omega}\right|^{d} \approx \left.\frac{d\sigma}{d\Omega}\right|^{p}_{\text{Ros}} + \left.\frac{d\sigma}{d\Omega}\right|^{n}_{\text{Ros}} \tag{4.22}$$

where the Rosenbluth cross section is:

$$\left.\frac{d\sigma}{d\Omega}\right|_{\text{Ros}}(E,\theta) = \left.\frac{d\sigma}{d\Omega}\right|_{\text{Mott}}(E,\theta) \cdot \left\{ \frac{G_E^2(Q^2) + \tau G_M^2(Q^2)}{1+\tau} + 2\tau G_M^2(Q^2)\tan^2\frac{\theta_e}{2} \right\} \tag{4.23}$$

the Mott cross section is:

$$\left.\frac{d\sigma}{d\Omega}\right|_{\text{Mott}}(E,\theta) = \frac{\alpha^2}{4E^2\sin^4\dfrac{\theta_e}{2}} \cdot \frac{E'}{E}\cos^2\frac{\theta_e}{2} \tag{4.24}$$

The parameters have the same meaning as those defined in the equation 1.9 in the section 1.1. In our case $E = 315.1$ MeV. Now we list the parameters that depend on the polar angle.

Ring	$\overline{\theta}$	E' (MeV)	Q^2 (GeV^2)	G_E^p	G_M^p	G_E^n	G_M^n
1	140.78	197.5	0.2208	0.5878	1.6598	0.0237	−1.1432
2	142.31	196.8	0.2205	0.5862	1.6554	0.0238	−1.1402
3	143.80	196.2	0.2233	0.5847	1.6513	0.0239	−1.1374
4	145.23	195.6	0.2244	0.5833	1.6475	0.0239	−1.1348
5	146.61	195.0	0.2254	0.5820	1.6440	0.0240	−1.1324
6	147.94	194.5	0.2264	0.5808	1.6408	0.0241	−1.1302
7	149.23	194.1	0.2272	0.5797	1.6378	0.0241	−1.1282

where we have calculated the scattered electron energy E' using the equation 4.2, the square four-moment transfer Q^2 using the equation 1.10 and the electromagnetic Sachs form factors for both the neutron and proton have been calculated using the Friedrich and Walcher parametrization given by [31].

As we want to compare both the count rates and the differential cross sections, we need both quantities as an average over the detector acceptance and the target length:

$$\left(\frac{d\sigma}{d\Omega}\right)_{av} = \frac{1}{\int_{target} dl \int_\Omega d\Omega} \int_{target} dl \int \frac{d\sigma}{d\Omega}(E,\theta)d\Omega \qquad (4.25)$$

$$R = L \frac{1}{\int_{target} dl} \int_{target} dl \iint \frac{d\sigma}{d\Omega}(E,\theta)\sin\theta \; d\theta \; d\phi \qquad (4.26)$$

Comparison of the experimentally observed and the expected rates

The experimentally observed cross section is calculated as the quotient of the luminosity L and the count rate R

$$\sigma = \frac{R}{L} \qquad (4.27)$$

where the count rate is calculated for every ring as they cover the whole 2π azimuthal angle and a small interval of the polar scattering angle. The number of counts for one ring is calculated using a single run (to keep the beam conditions as stable as possible) and adding the number of counts of all the frames corresponding to one ring. In each single module the number of counts for both polarization states are added.

$$N_{i,Ring} = \sum_{fr=1}^{146} N_{i,mod} \qquad \left(N_{i,mod} = N_{i,mod}^+ + N_{i,mod}^-\right) \qquad (4.28)$$

The number of counts per ring is divided by the duration of one single run $T_i = 300$ s. The particular value of the beam current intensity for the run used is provided by the PIMO27 beam current monitor. The count rate is normalized to the beam current intensity of 20 μA and is normalized to the total number of frames per ring, as some of them are not included in the analysis because they are damaged or not working.

$$R_{i,Ring} = \frac{N_{i,Ring}}{T_i} \frac{20\mu A}{I_i} \frac{146}{n_{i,Ring}^{Det}} \qquad (4.29)$$

In the table below we show the average polar angle $\bar\theta$, the solid angle $\Delta\Omega$, the theoretical Rosenbluth cross section σ_{theo} and the experimentally observed cross section calculated from the data σ_{exp} for the seven rings of the calorimeter. The values of both the experimental and the theoretical cross sections are plotted in the figure 4.11. The R_{cal} is calculated by means of the equation 4.26. On the other hand, the experimentally observed count rate R_{exp} is the calculated using

the equation 4.29. In the last column the ratio of the experimental rate to the predicted rate R_{exp}/R_{cal} is shown for comparison.

Ring	$\overline{\theta}$	$\Delta\Omega$(sr)	R_{cal}(kHz)	R_{exp}(kHz)	σ_{theo}(nb)	σ_{exp}(nb)	R_{exp}/R_{calc}
1	140.78	0.1040	299	225	20.84	17.49	75.0%
2	142.31	0.1006	272	210	20.28	16.94	77.3%
3	143.80	0.0972	246	190	19.77	15.85	77.3%
4	145.23	0.0938	225	169	19.32	14.63	75.2%
5	146.61	0.0905	205	152	18.91	13.63	74.3%
6	147.94	0.0873	186	130	18.54	12.06	69.9%
7	149.23	0.0842	169	113	18.21	10.84	66.6%

The measured cross sections are smaller than the theoretical results. Nevertheless we are using the very naïve model of the deuteron cross section (see equation 4.22) based in the static approximation that is not sufficient to account for the quasielastic process in the deuteron. Moreover we have not considered the radiative corrections that deplect the quasielastic cross section as occurs in the case of the elastic cross section (as can be seen in the frame of the diploma [26]). We have shown here all the seven rings but the ring 1 and 7 should be discarded because in those rings the crystals are not surrounded by the complete set of eight crystals necessaries so that the energy deposition of the incident particles can be developed almost completely. The comparison in the figure 4.11 of the calculated cross section and the experimentally observed cross section shows that they present different slopes. The discrepancy between them increases with the scattering angle.
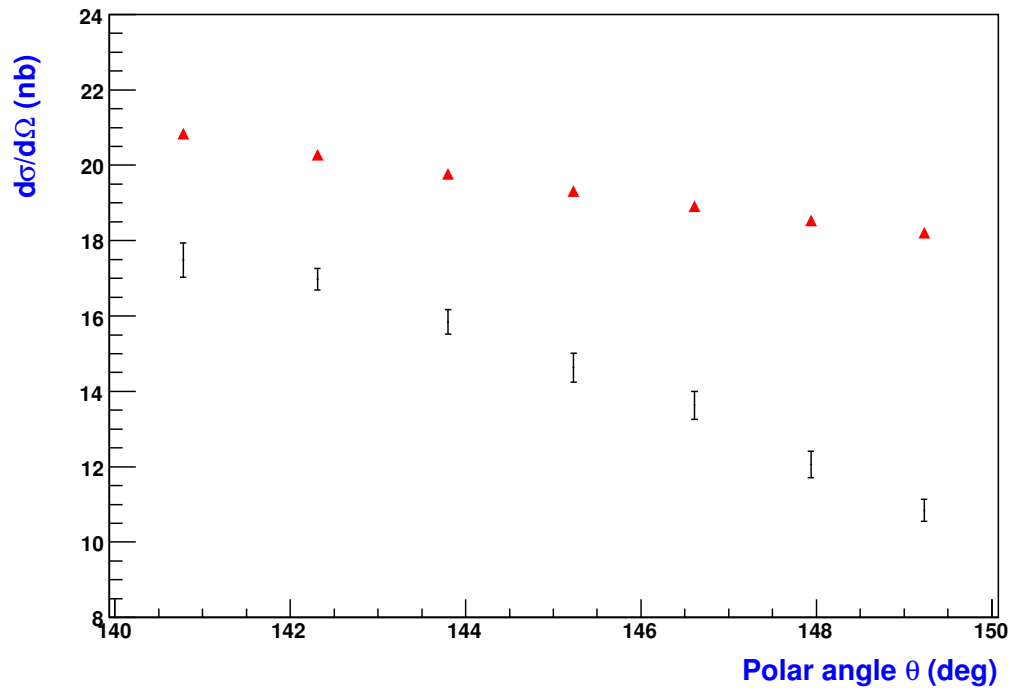
Figure 4.11. In red triangles the calculated cross section with the rough approximation $(d\sigma/d\Omega)_d \approx (d\sigma/d\Omega)_p + (d\sigma/d\Omega)_n$ for every ring is shown. In black one can see the experimentally observed cross section with the error bars.

Chapter 5

Determination of the physical asymmetry

The aim of this work is the extraction of the asymmetry in the quasielastic scattering. For this purpose the measured spectra described in the last chapter are used to obtain the number of counts for both opposite polarization states. The quasielastic peak appears isolated in the coincidence spectrum and we have the model described in section 4.5 to subtract the neutral background from the coincidence spectrum. Nevertheless due to the uncertainties inherent to the model parameters the extraction of the true events is not trivial. The first part of this chapter is thus devoted to the discussion of the optimum procedures to apply the model to obtain the true events. Two procedures are discussed: one based in the search of an optimum lower cut in energy; and another based in a weighted binwise method. First of all we present a discussion on the statistical behaviour of the number of counts and the measured asymmetry that will be useful in the following discussion of the above-mentioned procedures. Once the raw asymmetry has been extracted from the spectra we will check that the asymmetry azimuthal dependence is the expected one for the transverse spin asymmetry. The second part of the chapter is devoted to the correction of the raw asymmetry from the false asymmetries due to helicity correlated changes in the beam parameters or in the luminosity. The method employed is the multilinear regression analysis.

5.1   Statistical considerations

First we will make some considerations about the statistical behaviour of the measured asymmetry and about the number of counts. We will derive the expression for the statistical uncertainty in the measured asymmetry and also the expected statistical uncertainty in the number of counts as both the asymmetry

and the number of counts uncertainties are closely related.

Number of counts   The probability of scattering of beam electrons to the calorimeter solid angle is very small. It can be estimated as the quotient of the scattered electrons rate for the whole calorimeter $R \approx 1022 \cdot 1.4$ kHz and the flux of incident beam electrons I_e/e where $I_e = 20\ \mu A$ is the beam current intensity and e is the electron charge:

$$p = \frac{R}{I_e/e} \approx 10^{-8} \tag{5.1}$$

As the probability of scattering is very small and the incident flux of electrons is large $I_e/e = 1.25 \cdot 10^{14}$ s^{-1}, the number of events is expected to follow a Poisson parent distribution [1]. If the mean of the number of counts, that is, the number of observed scattered electrons, for a certain time period is $\overline{N}$ the standard deviation will be the square root of the mean $\sigma = \sqrt{\overline{N}}$. Moreover since the mean of the number of counts for a certain time period is large the Poisson parent distribution fulfils the gaussian limit. Hence the parent distribution of the number of counts, if the statistical fluctuations of the beam parameters, especially the beam current intensity, are not considered, is a gaussian whose width σ is the square root of the mean.

Asymmetry   The asymmetry in the number of counts for the opposite polarization states, called the raw asymmetry, is defined as:

$$A = \frac{N^+ - N^-}{N^+ + N^-} = \frac{\Delta N}{N} \tag{5.2}$$

The asymmetry is expected to follow a gaussian parent distribution. The standard deviation of the asymmetry can be expressed as a function of the statistical uncertainty in the number of counts. For that purpose we can use the theory of error propagation. Or equivalently: the squared relative error of a quotient is the sum of the squares of the relative errors:

$$\frac{\sigma^2(A)}{A^2} = \frac{\sigma^2(\Delta N)}{(\Delta N)^2} + \frac{\sigma^2(N)}{N^2} \tag{5.3}$$

Now we use the fact that $\sigma(\Delta N) = \sigma(N)$ to write

$$\frac{\sigma^2(A)}{A^2} = \frac{\sigma^2(N)}{(\Delta N)^2} + \frac{\sigma^2(N)}{N^2} \tag{5.4}$$

---

[1]In the processes that lead to the Poisson distribution we consider only the scattering but of course in the real experiment the probability of detection should be also taken into account

And using the definition of the asymmetry $\Delta N = A \cdot N$

$$\frac{\sigma^2(A)}{A^2} = \frac{\sigma^2(N)}{(AN)^2} + \frac{\sigma^2(N)}{N^2} \qquad (5.5)$$

Taking out a common factor

$$\frac{\sigma^2(A)}{A^2} = \frac{\sigma^2(N)}{N^2}\left(1 + \frac{1}{A^2}\right) \qquad (5.6)$$

So finally

$$\sigma(A) = \frac{\sigma(N)}{N}\sqrt{1 + A^2} \qquad (5.7)$$

If the asymmetry is very small $A \approx 10^{-6}$ the statistical error might be approximated by

$$\sigma(A) = \frac{\sigma(N)}{N} \qquad (5.8)$$

In the case the number of counts has a Poisson parent distribution $\sigma(N) = \sqrt{N}$ we obtain the very familiar expression for the asymmetry standard deviation

$$\sigma(A) = \frac{1}{\sqrt{N}} \qquad (5.9)$$

The last derivation has taken into account only the statistical fluctuations of the underlying scattering process. If there are other processes whose statistical fluctuations have influence on the asymmetry value like fluctuations of either the beam current intensity or the target density, it is expected, according to the Central Limit Theorem, the asymmetry to follow a broader gaussian distribution; just in the case those fluctuations are not helicity correlated. These contributions to the asymmetry error are known as non helicity correlated systematic errors. On the other hand if those fluctuations are helicity correlated they shift the mean of the asymmetry distribution and are called helicity correlated systematic errors. A schematic drawing of the difference between the helicity correlated systematic errors and the non helicity correlated fluctuations is shown in the figure 5.1.

5.2 Determination of the raw asymmetry from the experimentally observed spectra

Now we focus in how to determine the asymmetry in the quasielastic scattering from the coincidence and noncoincidence spectra. For that purpose the true quasielastic events must be extracted from the experimental histograms for both polarization states. The raw asymmetry is calculated as:
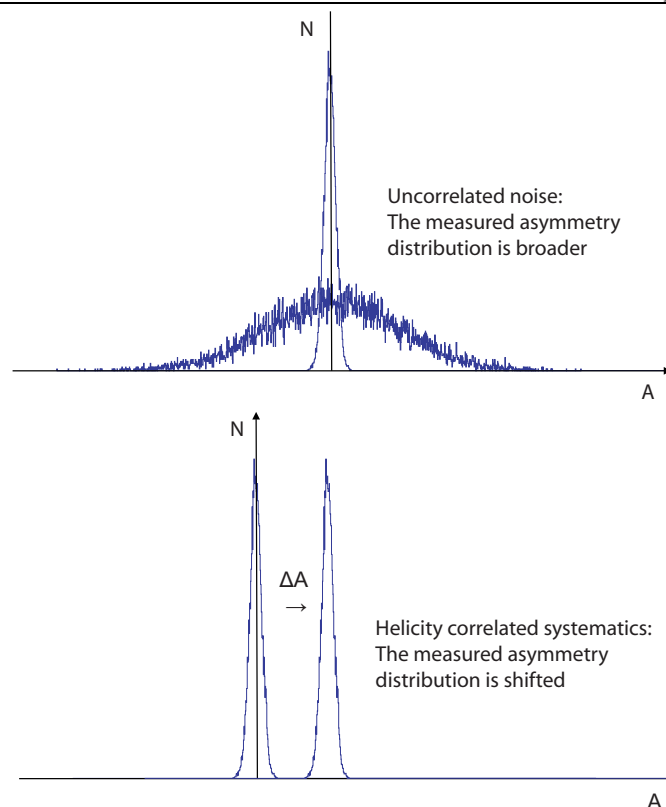
Figure 5.1. The upper picture illustrates the effect of the fluctuations that are not helicity correlated: they just make the asymmetry distribution broader. On the other hand if there are helicity correlated fluctuations of beam properties or target fluctuations a shift of the mean asymmetry occurs [22].

$$A_{ph} = \frac{N_{ph}^+ - N_{ph}^-}{N_{ph}^+ + N_{ph}^-} \tag{5.10}$$

As it was explained in the last chapter the quasielastic peak is delimited by two cuts in energy: an upper cut to exclude the pile up events, and a lower cut to separate the quasielastic events from the inelastic events. The neutral background mixed in the quasielastic region can be subtracted using the scaling and shifting model. However the uncertainties in the parameters of the model introduce a source of error in the extraction of the asymmetry.

Two different methods will be used to extract the true events by means of the scaling and shifting model and to handle the source of error introduced by them:

- applying an optimum lower cut in energy

- and the weighting procedure.

The first method, the application of an optimum lower cut, has been studied with much more intensity in the framework of this thesis and therefore it will be presented here more detailed than the other one.

5.2.1   Applying cuts

In this procedure the number of quasielastic events are obtained integrating the histograms between convenient cuts in energy and applying the scaling and shifting model. Then the dependence of the measured asymmetry error on the position of the lower cut in energy is studied so that an optimum lower cut can be found to minimize the error.

First the quasielastic peak (in the coincidence histogram) is integrated between a lower cut and an upper cut in energy for both polarization states and the number of counts obtained from these integrals are called N_{co}^+ and N_{co}^-. The asymmetry associated with these numbers of counts of the coincidence histogram is:

$$A_{co} = \frac{N_{co}^+ - N_{co}^-}{N_{co}^+ + N_{co}^-} \qquad (5.11)$$

Afterwards the noncoincidence histogram is integrated between the same lower and upper cuts in energy as in the coincidence histogram, but both cuts shifted to the right by the amount δ provided by the model. The noncoincidence integrals are performed also for both polarization states. The number of counts resulting from these integrals are called $N_{non+\delta}^+$ and $N_{non+\delta}^-$, where the subindex δ has been included to remind that the integral in the noncoincidence histogram is done between the shifted cuts. The asymmetry associated with the noncoincidence histogram events is:

$$A_{non} = \frac{N_{non+\delta}^+ - N_{non+\delta}^-}{N_{non+\delta}^+ + N_{non+\delta}^-} \qquad (5.12)$$

Finally, in order to obtain an estimation of the background in the quasielastic peak region in the coincidence histogram the $N_{non+\delta}^\pm$ are multiplied by the model scaling factor ϵ. This estimated background is subtracted from the coincidence number of counts.

$$N_{ph}^\pm = N_{co}^\pm - \epsilon N_{non+\delta}^\pm \qquad (5.13)$$

The raw asymmetry in the quasielastic events in thus calculated from these estimated true quasielastic number of counts $N_{ph}^\pm$.

$$A_{ph} = \frac{(N_{co}^+ - \epsilon N_{non+\delta}^+) - (N_{co}^- - \epsilon N_{non+\delta}^-)}{(N_{co}^+ - \epsilon N_{non+\delta}^+) + (N_{co}^- + \epsilon N_{non+\delta}^-)} \qquad (5.14)$$

The expression for the asymmetry in the quasielastic events can be written in terms of both the coincidence and noncoincidence asymmetries.

Regrouping terms in the equation 5.14

$$A_{ph} = \frac{(N_{co}^+ - N_{co}^-) - \epsilon(N_{non+\delta}^+ - N_{non+\delta}^-)}{(N_{co}^+ + N_{co}^-) - \epsilon(N_{non+\delta}^+ - N_{non+\delta}^-)} \tag{5.15}$$

using now the definitions of both A_{co} and A_{non} and calling $N_{co} = N_{co}^+ + N_{co}^-$ and $N_{non+\delta} = N_{non+\delta}^+ + N_{non+\delta}^-$

$$A_{ph} = \frac{A_{co}N_{co} - \epsilon A_{non}N_{non+\delta}}{N_{co} - \epsilon N_{non+\delta}} \tag{5.16}$$

Dividing both numerator and denominator by N_{co}

$$A_{ph} = \frac{A_{co} - \dfrac{\epsilon N_{non+\delta}}{N_{co}}A_{non}}{1 - \dfrac{\epsilon N_{non+\delta}}{N_{co}}} \tag{5.17}$$

Observe that $\frac{\epsilon N_{non+\delta}}{N_{co}} = \frac{\epsilon N_{non+\delta}}{N_{ph} + \epsilon N_{non+\delta}}$ is the proportion of events inside the coincidence histogram integrated region that correspond to the background. We will call this proportion the dilution factor f:

$$f = \frac{\epsilon N_{non+\delta}}{N_{co}} = \frac{\epsilon N_{non+\delta}}{N_{ph} + \epsilon N_{non+\delta}} \tag{5.18}$$

The dilution factor satisfies $0 \leq f \leq 1$

$$A_{ph} = \frac{A_{co} - fA_{non}}{1 - f} \tag{5.19}$$

The equation 5.19 is the basic formula to calculate the physical asymmetry. It means that the noncoincidence asymmetry must be taken into account for the background events in the coincidence histogram in order to calculate the asymmetry in the quasielastic scattering.

The choice of a convenient lower cut is not trivial. We sum up the reasons that make it necessary to find a criterium in order to choose an optimum lower cut:

- The finite energy resolution of the detector that mixes both the quasielastic and inelastic events. This fact is common for all the configurations even at the forward angles.

- The presence of some degree of neutral background in the coincidence spectrum at the backward configuration. This presence is even more acute in the case of deuterium data.

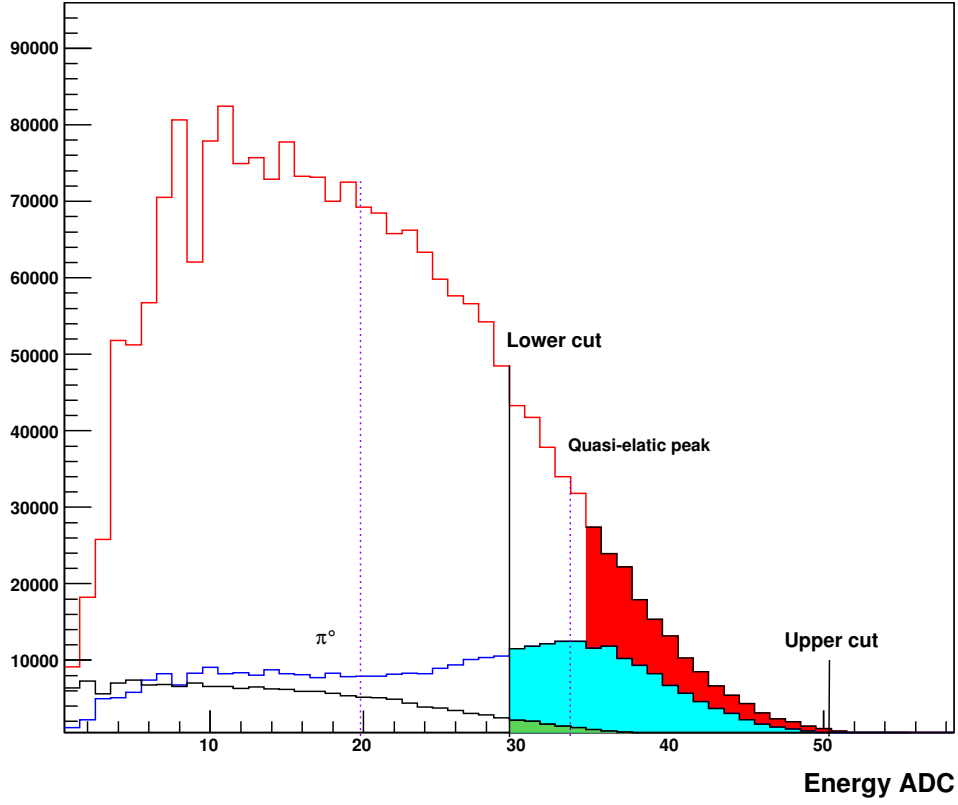The second reason is the dominant in our particular configuration.

Figure 5.2. The coincidence histogram is shown in blue. The noncoincidence histogram is shown in red. Both correspond to the deuterium target. The pointed lines represent the quasielastic peak and the pion threshold. The black line to the right corresponds to the upper cut in energy of the quasielastic peak. And the black line in the left corresponds to the lower cut. The coincidence histogram is integrated between the lower and the upper cuts to obtain the coincidence counts. The integrated region is filled with blue. The noncoincidence histogram is integrated applying the model shift δ to the cuts. The red region is the integrated region where the noncoincidence events are extracted from. The black histogram corresponds to the background in the coincidence spectrum, according to the model. It is obtained from the noncoincidence histogram applying the shift δ and the scaling factor ϵ. The green region corresponds to the background inside the quasielastic peak. The integral corresponding to the green region is equivalent to multiplying the noncoincidence red region by the scaling factor ϵ. The spectra shown in the figure correspond to the module 32, in the ring 4.

Uncertainty of the extracted physical asymmetry as a function of the lower cut position

From the equations 5.13 and 5.19 the necessity of an optimum lower cut can be understood.

The presence of a background in the coincidence spectrum will introduce a systematic error due to the uncertainty in the parameters δ and ϵ of the model. If the lower cut is moved to the right we lose statistics but the systematic error also decreases. On the other hand if the lower cut is moved to the left to gain statistics, the systematic error is increased.

From equation 5.13 we get

$$\sigma^2(N_{ph}) = \sigma^2(N_{co}) + \epsilon^2 \sigma^2(N_{non+\delta}) = N_{co} + \epsilon^2 N_{non+\delta} \qquad (5.20)$$

where we have not taken into account for the moment the error in the parameters. And finally we get for the error of the asymmetry, using the equation 5.8:

$$\sigma^2(A_{ph}) \approx \frac{\sigma^2(N_{ph})}{N_{ph}^2} = \frac{N_{co} + \epsilon^2 N_{non+\delta}}{(N_{co} - \epsilon N_{non+\delta})^2} \qquad (5.21)$$

And dividing both numerator and denominator by N_{co}^2

$$\sigma^2(A_{ph}) \approx \frac{1}{(1-f)^2} \frac{1}{N_{co}} + \frac{f^2}{(1-f)^2} \frac{1}{N_{non+\delta}} \qquad (5.22)$$

This approximate formula for the asymmetry shows that both terms are a product of two factors

- The first factors $1/(1-f)^2$ or $f^2/(1-f)^2$ that are decreasing when the lower cut is moved to the right. Because when going to the right the background dilution f decreases.

- The second factors $1/N_{co}$ and $1/N_{non+\delta}$ increase when the lower cut is moved to the right because both N_{co} and $N_{non+\delta}$ decrease.

Therefore the $\sigma(A_{ph})$ presents a minimum for some position of the lower cut or equivalently for some value of the dilution factor f.

Effectively when the lower cut is moved to the left the number of true events N_{ph} increases and therefore we would expect a decrease of the asymmetry statistical error but at the same time we must subtract a greater amount of background in order to get the true events. The error of the difference, that is quadratically additive, $\sigma(N_{ph}) = \sqrt{\sigma^2(N_{co}) + \sigma^2(\epsilon N_{non+\delta})}$ increases the statistical error $\sigma(A) = \sigma(N_{ph})/N_{ph}$.

Exact formula for the physical asymmetry error

After this discussion we can define the $\sigma(A)$ physical asymmetry error as the figure of merit.

In order to calculate the exact formula for $\sigma(A_{ph})$ we can apply the theory of propagation of errors to the formula 5.19. Since the dilution factor is given by $f = \epsilon N_{non+\delta}/N_{co}$ the uncertainty of f comes from the uncertainty in the model parameters δ and ϵ and from the error in the number of counts of the coincidence histogram N_{co} and the number of counts of the noncoincidence histogram $N_{non+\delta}$. Moreover, the asymmetry in the noncoincidence spectrum A_{non} depends on the value of the δ parameter because the asymmetry of the neutral background, that is a mixture of several physical processes with different physical asymmetries, depends on the energy cut. The error in the physical asymmetry is thus calculated as:

$$\sigma^2(A_{ph}) = \left(\frac{\partial A_{ph}}{\partial A_{co}}\right)^2 \sigma^2(A_{co}) + \left(\frac{\partial A_{ph}}{\partial A_{non}}\right)^2 \sigma^2(A_{non}) + \left(\frac{\partial A_{ph}}{\partial N_{co}}\right)^2 \sigma^2(N_{co}) +$$

$$+ \left(\frac{\partial A_{ph}}{\partial N_{non+\delta}}\right)^2 \sigma^2(N_{non+\delta}) + \left(\frac{\partial A_{ph}}{\partial \epsilon}\right)^2 \sigma^2(\epsilon) + \left(\frac{\partial A_{ph}}{\partial \delta}\right)^2 \sigma^2(\delta) \quad (5.23)$$

Doing the derivatives we arrive to the formula:

$$\sigma^2(A_{ph}) = \frac{1}{(1-f)^2}\sigma^2(A_{co}) + \frac{f^2}{(1-f)^2}\sigma^2(A_{non}) +$$

$$+ (A_{ph} - A_{non})^2 \frac{f^2}{(1-f)^2}\left[\frac{\sigma^2(N_{co})}{N_{co}} + \frac{\sigma^2(N_{non+\delta})}{N_{non+\delta}} + \frac{\sigma^2(\epsilon)}{\epsilon^2}\right]$$

$$+ \frac{f^2}{(1-f)^2}\left[(A_{ph} - A_{non})\frac{1}{N_{non+\delta}}\frac{\partial N_{non+\delta}}{\partial \delta} - \frac{\partial A_{non+\delta}}{\partial \delta}\right]^2 \sigma^2(\delta) \quad (5.24)$$

Looking carefully at the formula 5.24 we see that the error in the dilution factor is suppressed by the factor $\left(A_{ph} - A_{non}\right)$ if the asymmetries differ in some tens of ppm as we expect, that is $A_{ph} - A_{non} \approx 10^{-5}$. Let us compare the order of magnitude of each term included in the formula 5.24 so that we can see which terms are the relevant.

The following relations and values will be used to estimate the order of magnitude:

$$\sigma(A_{co}) = \frac{1}{\sqrt{N_{co}}} \quad (5.25)$$

$$\sigma(A_{non}) = \frac{1}{\sqrt{N_{non+\delta}}} \quad (5.26)$$

The rough estimation of the background dilution factor $f = 0.2$ The estimated number of coincidence counts used in this analysis is $N_{co} = 4 \cdot 10^5 \cdot 1022 \cdot 700 = 2.8 \cdot 10^{11}$. Equivalently for the noncoincidence histogram: $N_{non+\delta} = 10^6 \cdot 1022 \cdot 700 = 7 \cdot 10^{11}$ The rough estimation of the difference in the asymmetry in the quasielastic scattering and the asymmetry in the noncoincidence events $|A_{ph} - A_{non}| = 10^{-5}$. We assume that the relative errors in the model parameters ϵ and δ are around 10%.

Order of magnitude

1	$\dfrac{1}{1-f}\sigma(A_{co})$	2.36 ppm
2	$\dfrac{f}{1-f}\sigma(A_{non})$	0.30 ppm
3	$\dfrac{f}{1-f}|A_{ph} - A_{non}|\dfrac{\sigma(N_{co})}{N_{co}}$	$4.7 \cdot 10^{-6}$ ppm
4	$\dfrac{f}{1-f}|A_{ph} - A_{non}|\dfrac{\sigma(N_{non+\delta})}{N_{non+\delta}}$	$3.0 \cdot 10^{-6}$ ppm
5	$\dfrac{f}{1-f}|A_{ph} - A_{non}|\dfrac{\sigma(\epsilon)}{\epsilon}$	0.25 ppm
6	$\dfrac{f}{1-f}|A_{ph} - A_{non}|\left|\dfrac{1}{N_{non+\delta}}\dfrac{\partial N_{non+\delta}}{\partial \delta} - \dfrac{\partial A_{non+\delta}}{\partial \delta}\right|\sigma(\delta)$	1.3 ppm

One can observe that the first term is the dominant. The systematic contributions due to uncertainties in the model parameters, terms 5 and 6, start competing with the second term when the complete set of data, that is all the counts, is used in the analysis. The first term is the dominant and the terms 2 and 5 give a small contribution of the same order of magnitude between them. The terms 3 and 4 are completely negligible. Finally the contribution to the error arising from the dependence of the A_{non} on the energy cut is given in the row 6. This contribution has been estimated using the results of the analysis of the asymmetry in the noncoincidence spectrum that will be introduced in the section 6.3.

Let us define as statistical error those terms that are decreasing functions of total integrated number of events. On the other hand, it makes sense defining the last terms as the systematic error. Any uncertainty in the knowledge of the conversion factor or the shift will produce a change of the measured asymmetry.

$$\Delta_{stat}^2(A_{ph}) = \frac{1}{(1-f)^2}\sigma^2(A_{co}) + \frac{f^2}{(1-f)^2}\sigma^2(A_{non}) \tag{5.27}$$

$$\Delta_{syst}^2(A_{ph}) = (A_{ph} - A_{non})^2 \frac{f^2}{(1-f)^2}\frac{\sigma^2(\epsilon)}{\epsilon^2} +$$
$$+ \frac{f^2}{(1-f)^2}\left[(A_{ph} - A_{non})\frac{1}{N_{non+\delta}}\frac{\partial N_{non+\delta}}{\partial \delta} - \frac{\partial A_{non+\delta}}{\partial \delta}\right]^2 \sigma^2(\delta) \tag{5.28}$$

The terms depending on $\sigma(N)$ are suppressed by $(A_{ph} - A_{non})^2$.

Data analysis-finding the optimum lower cut

In the figure 5.2.1 one can see how the total integrated number of events depends on the lower cut. The particular module 32, at the central ring 4, for one single run is used as an illustration without limiting the generality of the discussion. In red is shown the dependence of the noncoincidence counts on the lower cut and in blue the dependence of the coincidence counts on the lower cut. In the figure 5.5 one can observe the dependence of the dilution factor on the position of the lower cut. With this information the asymmetry error is calculated according to the equation 5.24 for one module as a function of the position of the lower cut. This function is shown in the figure 5.6. The curve shows that the error decreases if the lower cut is moved to the right, up to a minimum value, at the ADC channel 30 (for this particular module) and then it starts increasing quickly. So if we want to minimize the asymmetry error the optimum cut for this module would be at ADC = 30. It corresponds to a dilution factor $f \approx 20$ %.

Instead of finding the optimum cut in terms of the k defined in 4.3.4 for each single module a more practical procedure is used. This procedure consists in labelling the lower cut with the dilution factor f given according to the scaling and shifting model. The lower cut for each module and for each single run in selected so that the dilution factor is the same in all the channels and all the runs used in the analysis. To investigate this dependence all the runs of the transversal spin data are used. The samples of runs and the corresponding information about the GVZ half-wave plate are shown in the table below.

Sample	Run numbers	GVZ
1	$44662 - 48000$	IN
2	$44802 - 44938$	OUT
3	$49153 - 49413$	OUT
4	$49415 - 49682$	IN

In order to extract the asymmetries from the data several lower cuts have been used that correspond to the values of the dilution factor $f = 29\%$, 23%, 20%, 17%, 14%, 11%, according to the simple model to subtract the background from the coincidence spectrum. In the figure 5.7 the raw asymmetry distributions for a single sector corresponding to the different values of the dilution factor are shown. The width of the gaussians are used to estimate the error of the asymmetry. The errors are shown in the table below

dilution	$\Delta(A_\perp^{raw})(ppm)$
29%	8.84
23%	8.57
20%	8.62
17%	8.61
14%	8.74
11%	8.96

In this table we can observe the dependence of the error in the asymmetry with the dilution factor, that is, with the lower cut. The general tendency in all the sectors is that the error decreases with the dilution factor until it reaches a minimum at $f = 17\%$ and then the error starts increasing. There are, though, some fluctuations as that we can observe at $f = 23\%$ where the error is minimum and it breaks the tendency.   In order to increase the statistics it is better to collect all the sectors. As it is explained in the next section 5.3 we can obtain the error of the asymmetry combining all the sectors. The table below contains the error of the amplitude of the asymmetry when the asymmetries corresponding to each sector are plotted and fitted to a cosine.

dilution	$A_\perp^{raw}(ppm)$	$\Delta_{stat}(A_\perp^{raw})(ppm)$
29%	-30.76	4.34
23%	-34.40	4.20
20%	-35.50	4.20
17%	-36.21	4.14
14%	-37.86	4.17
11%	-40.69	4.32

The table above confirms that the asymmetry error decreases as the dilution factor goes down, it reaches a minimum and afterwards it starts increasing. The minimum corresponds to the dilution factor $f = 17\%$. It shows also a systematic drifting of the raw asymmetry value as the dilution factor changes. This drifting is a little larger than the asymmetry error. It is an evidence of the insufficiency of the model. The relation of the background in the coincidence spectrum with the photon spectrum, that is, the noncoincidence histogram is not so simple as the
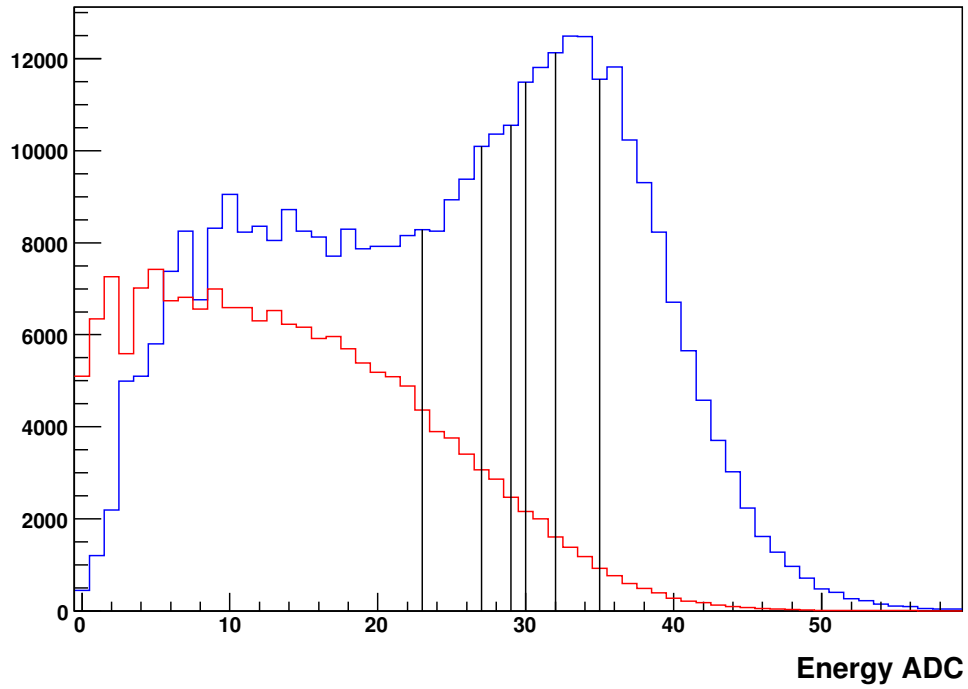
Figure 5.3. The picture shows the coincidence histogram in blue for D_2 data. The histogram in red is obtained from the noncoincidence histogram applying a shift δ and a scaling factor ϵ. The vertical lines represent the different lower cuts used in the present analysis to define the quasielastic peak. They are designed by the corresponding dilution factor f. From left to right they correspond respectively to $f = 29\%, 23\%, 20\%, 17\%, 14\%, 11\%$.

model assumes. Probably when the model is used the degree of remaining neutral background present in the coincidence spectrum depends on the position of the lower cut since the relation of the background in the coincidence spectrum with the noncoincidence histogram is not simple.
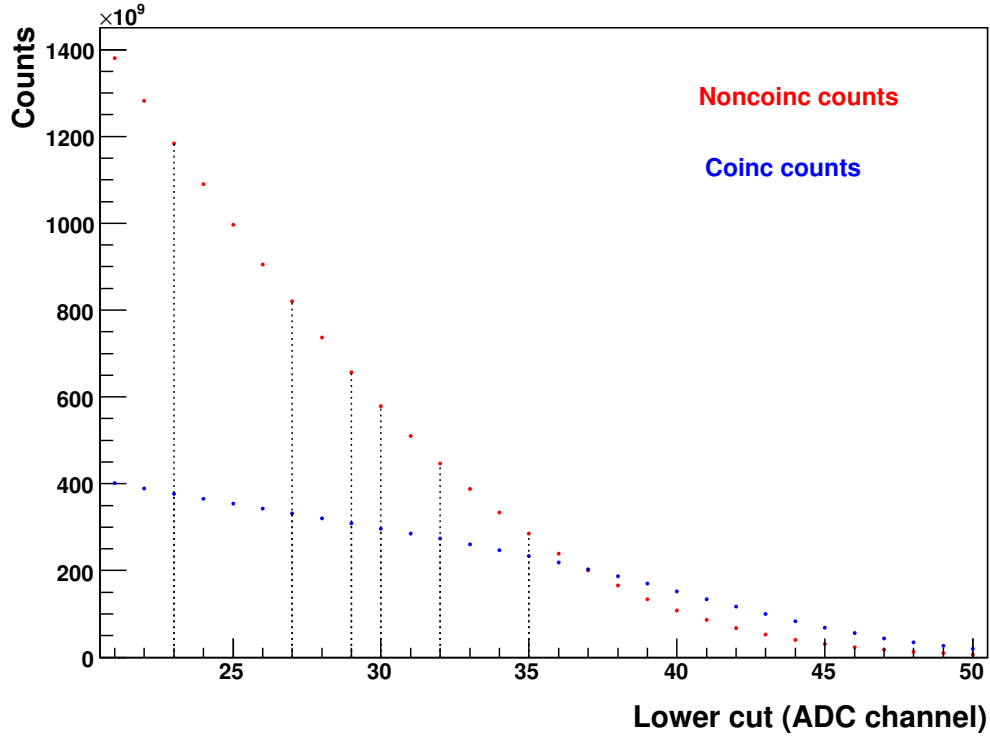
Figure 5.4.   The figure shows in red the number of counts of the noncoincidence histogram and in blue the number of counts of the coincidence histogram as function of the lower cut. The points have been calculated for a particular module (32) and one run but the number of counts has been scaled, so that it represents the total expected number of counts, multiplying by the total number of runs 700 and the total number of modules of the calorimeter, 1022. The vertical lines represent the different lower cuts used in the present analysis to define the quasielastic peak. From left to right they correspond respectively to $f = 29$ %, 23%, 20%, 17%, 14%, 11% (see figure 5.5)
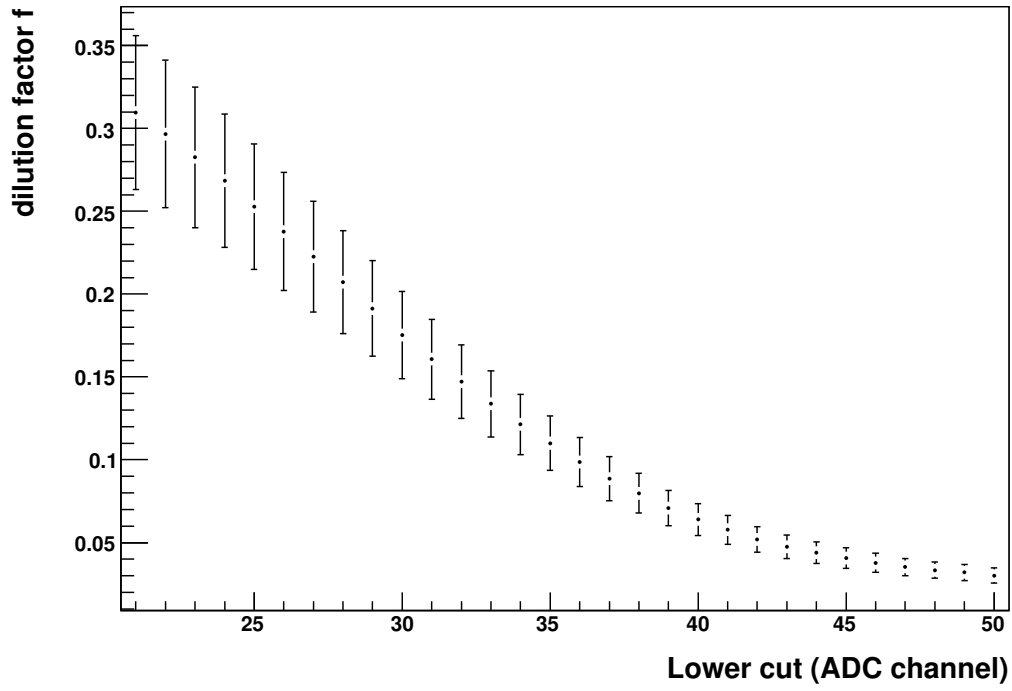
Figure 5.5. The dilution factor $f = \epsilon N_{non+\delta}/N_{co}$ as function of the lower cut for a representative module (module 32 whose spectra can be seen in the figure 5.7). The lower cut is represented as the ADC channel of the corresponding module. The error of the dilution factor is represented as well.
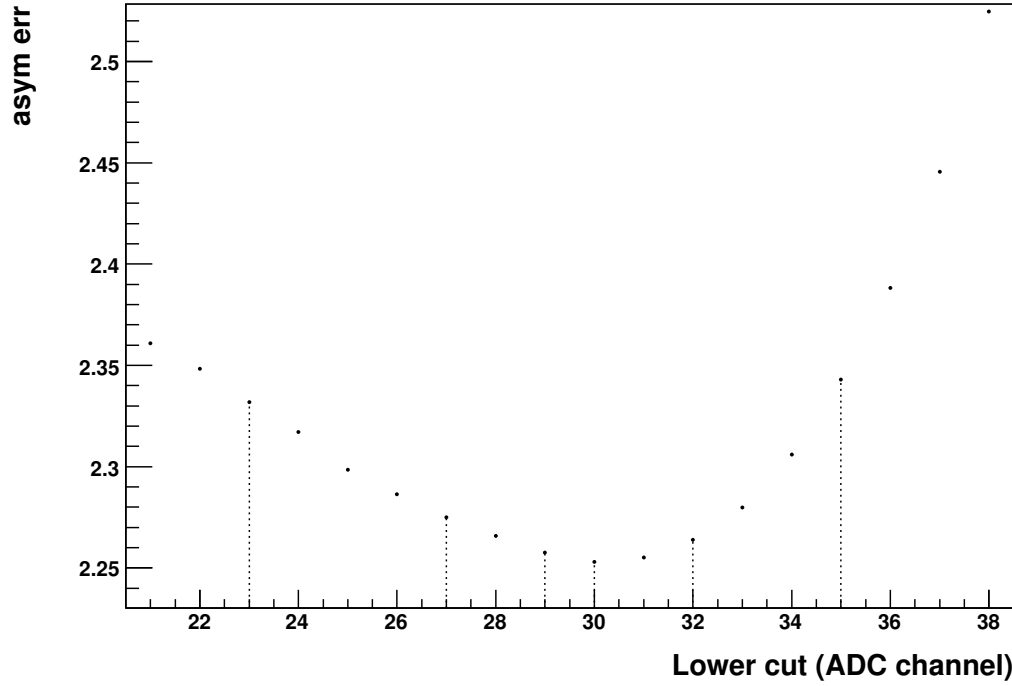
Figure 5.6. The error asymmetry given by the equation 5.24. The error has been obtained using the number of counts of the module 32 for one run as a function of the lower cut. Then it has been multiplied by the total number of channels and by the total number of runs 700 to estimate the error of the mean asymmetry. Both the statistic and the systematic error are taken into account. The systematic error starts to compete with the statistical error when we consider all the statistics provided by the whole calorimeter and the complete set of runs. The vertical pointed lines represent the ADC channels corresponding to determined dilution factor. From left to right they correspond respectively to $f = 29\%$, 23%, 20%, 17%, 14%, 11% (see figure 5.5). The minimum of the asymmetry corresponds to the dilution factor $f = 17\%$.
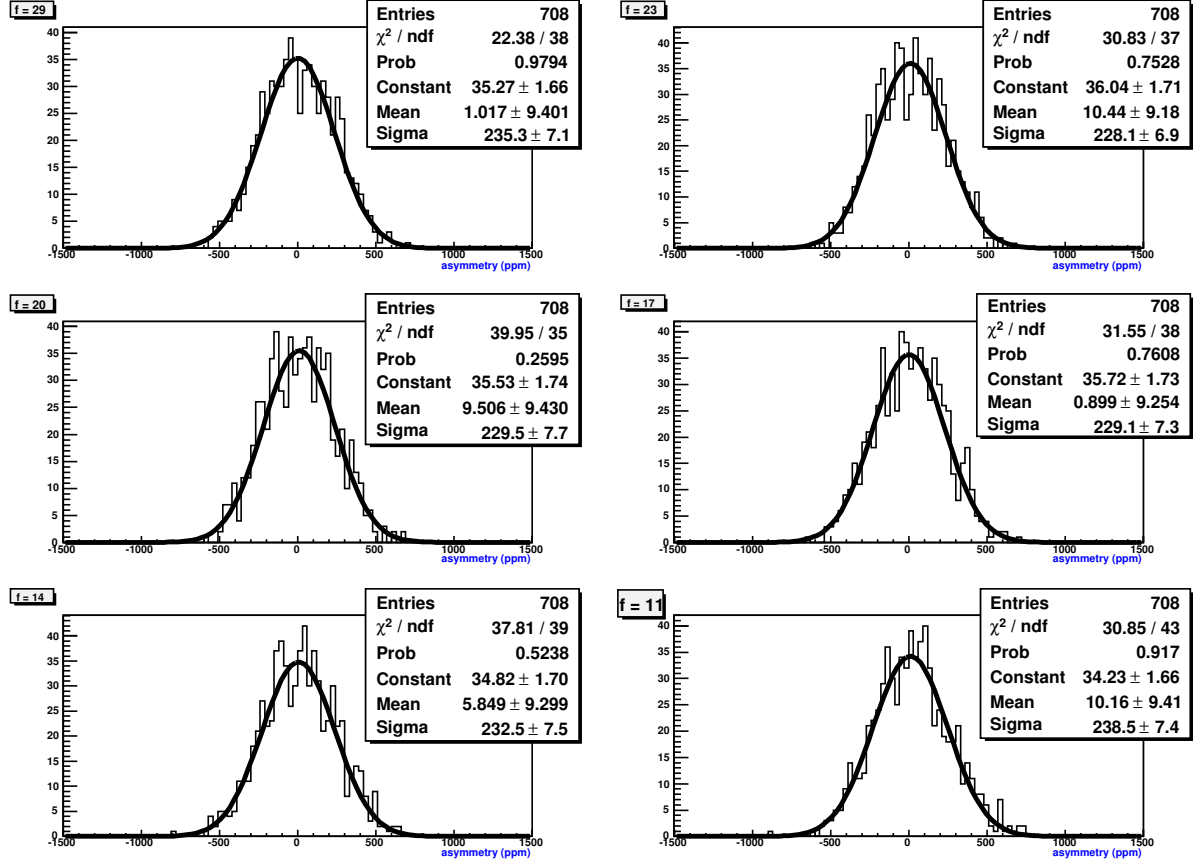
Figure 5.7. The nine panels shown the distribution of the asymmetries extracted for one sector (sector 8) using all the runs corresponding to the transversal data. In each panel the asymmetries have been calculating applying the lower cut associated to a value of the dilution factor f. The fit of the asymmetries distributions to a gaussian is extremely good in all the cases. One can observe the dependence of the width of the gaussian on the dilution factor.

5.2.2 The weighting procedure

In the last section 5.2.1 a procedure to extract the raw asymmetry has been explained. The raw asymmetry is calculated from the number of counts obtained integrating the quasielastic peak between the lower cut in energy and the upper cut in energy. The lower cut is chosen so that the asymmetry error is minimized. The disadvantage of this method is that the genuine events at the left of the lower cut are lost.

In order to include all the genuine quasielastic events in the analysis a weighting procedure can be applied. It consists in taking the lower cut at a distance of one energy resolution from the pion threshold so that all the genuine quasielastic events are contained in the region under analysis. The asymmetry is calculated for every histogram bin through the equation 5.19 where the variables refer in this case refereed to one bin. The asymmetry in the whole quasielastic peak is calculated as a weighted average of the binwise asymmetries. Every bin asymmetry is weighted with the inverse of the square of the asymmetry error given by the equation 5.23, where as before all the variables are referred to single bins.

$$A_{av} = \frac{\sum\limits_{i=l}^{u} \dfrac{1}{\sigma^2(A_i)} \, A_i}{\sum\limits_{i=l}^{u} \dfrac{1}{\sigma^2(A_i)}} \tag{5.29}$$

and the error is

$$\frac{1}{\sigma^2(A_{av})} = \sum_i \frac{1}{\sigma^2(A_i)} \tag{5.30}$$

where

$$\sigma^2(A_i) = \frac{1}{(1-f_i)^2}\sigma^2(A_i^{co}) + \frac{f_i^2}{(1-f_i)^2}\sigma^2(A_i^{non}) \tag{5.31}$$

The weighting procedure is necessary used when the asymmetry presents an energy dependence. The asymmetry we are measuring is equal for all the quasielastic events. But the presence of a background in the coincidence spectrum whose degree of dilution depends on the energy justifies using the weighting procedure. Actually the asymmetry of the background depends on the energy.

5.3 Azimuthal angle dependence

The accelerator provides a transversely polarized electron beam. The spin of the beam polarized electrons is perpendicular to the incident electron momentum and it is contained in the horizontal accelerator plane. The detector covers the

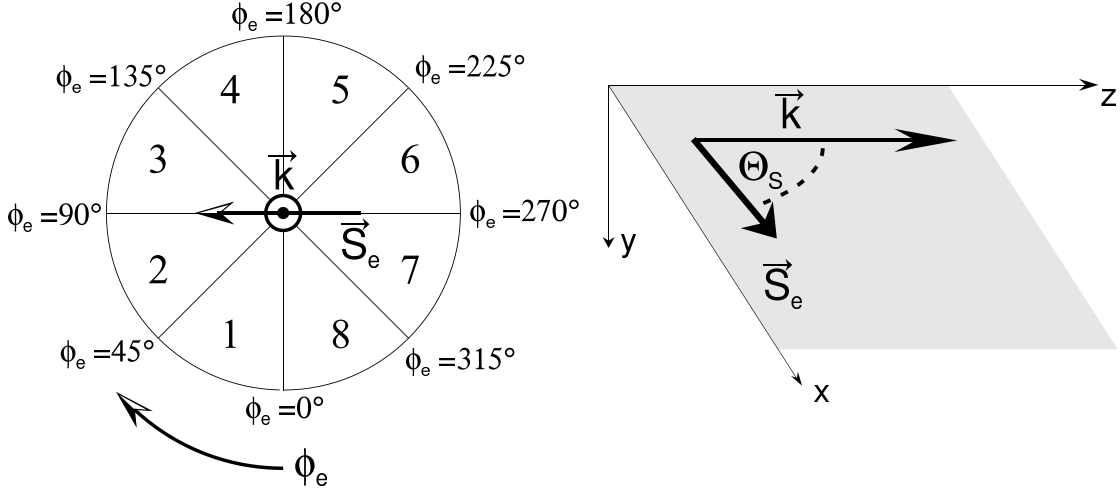whole 2π azimuthal angle range. The convention for the azimuthal angle is shown in the figure 5.8.

Figure 5.8. The calorimeter divided in eight sector as seen from the beam dump. The $\vec{k}$ stands for the incident electron momentum and it points out of the paper plane. The spin $\vec{S}_e$ is contained in the horizontal plane, perpendicular to the beam direction, oriented to the right of the beam. The θ_s stands for the angle between the electron momentum and the spin direction. The azimuthal angle ϕ has the origin below the plane that contains the momentum $\vec{k}$ and the spin $\vec{S}_e$ and increases clockwise, as seen from the beam dump.

The transverse spin asymmetry of the quasielastic $e-d$ scattering takes a maximum when the electron spin direction is perpendicular to the plane of scattering. If the spin direction is contained in the plane of scattering the asymmetry is zero. The plane of scattering is determined by the momentum of the incident electron $\vec{k}_{in}$ and the scattered electron momentum $\vec{k}_{out}$. The vector

$$\vec{S} = \frac{\vec{k}_{in} \times \vec{k}_{out}}{|\vec{k}_{in} \times \vec{k}_{out}|} \tag{5.32}$$

defines the normal direction to the scattering plane and also its positive orientation. Since the scattering of the electrons is symmetric in the azimuthal angle only the projection of the polarization vector P_e in the direction of the normal to the scattering plane, defined in 5.32, contributes to the two photon exchange asymmetry. Therefore the transverse spin asymmetry presents an azimuthal modulation with the $\cos\phi$.

$$A_\perp^m = \frac{\sigma_\uparrow - \sigma_\downarrow}{\sigma_\uparrow + \sigma_\downarrow} = A_\perp(\theta)\vec{P}_e \cdot \vec{S} = A_\perp \cos\phi \tag{5.33}$$

the amplitude of the asymmetry depends on the scattering angle θ. In the analysis the amplitude of the asymmetry corresponds to an average of the asymmetry over the detector scattering angle range.

As the photon exchange asymmetry exhibits an azimuthal modulation $A_\perp = A_\perp^\circ \cos\phi$ in order to gain statistics it is an established procedure in th A4 experiment to divide the calorimeter in 8 sectors (see figure 5.8). Each sector corresponds to one of the luminosity monitors. The size of the sectors is such that it is a compromise between the spatial resolution and the statistics.

Given a sector the asymmetry is calculated for every run. The sign of the asymmetry corresponding to the runs of the samples with the GVZ half wave plate introduced (IN) is changed $A_\perp = -A_\perp^{IN}$ so that all the asymmetries can be collected.

In order to obtain the asymmetry error one can use the known estimators of the mean and the standard deviation:

$$\bar{A}_\perp^s = \frac{1}{N_r} \sum_i^r A_i^s \tag{5.34}$$

$$\sigma(A_\perp^s) = \frac{1}{N_r - 1} \sum_i^r (A_i^s - \bar{A}_\perp^s)^2 \tag{5.35}$$

One can plot also the set of asymmetries extracted from data in a histogram to study how they are distributed. The gaussian fits to the data. The fit parameter σ is an estimator of the width of the parent distribution.

As explained in the section 5.2.1 we have calculated the raw asymmetries using all the runs corresponding to transversal deuterium data. First we calculate the asymmetry for every frame averaging the asymmetry over the five inner rings to gain statistics. In the figure 5.9 we show the plot. The raw asymmetries exhibit the known $\cos\phi$ azimuthal modulation. The set of data fits extremely well to the function

$$A_\perp = A_\perp^0 \cos(\phi + \delta) + b \tag{5.36}$$

where δ is a phase and b is the offset.

The plot of the extracted raw asymmetries for the eight sectors is also shown in the figure 5.10. It is obvious that the function 5.36 fit is also extremely good despite we are dealing with raw data that have been neither normalized to the target density nor corrected from the false asymmetries.

Also shown are the asymmetries for the eight sectors that are obtained using the weighting procedure (5.11). It is notable that the error in the asymmetry in this case is about 0.25 ppm smaller than the error obtained by the cut method.
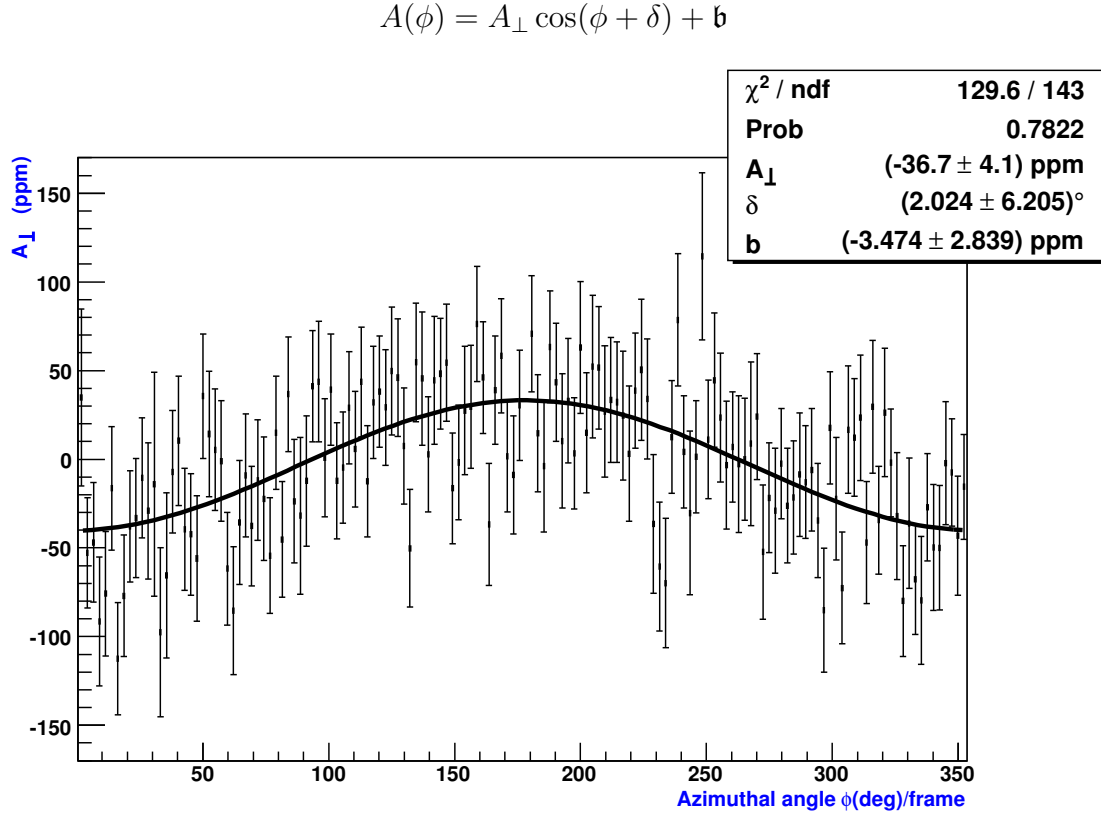
$$A(\phi) = A_\perp \cos(\phi + \delta) + \mathfrak{b}$$

χ^2 / ndf	129.6 / 143
Prob	0.7822
$A_\perp$	(-36.7 ± 4.1) ppm
δ	$(2.024 \pm 6.205)°$
b	(-3.474 ± 2.839) ppm

Figure 5.9. The extracted raw asymmetries for the 146 calorimeter frames show a clear cosine dependence on the azimuthal angle ϕ. The asymmetry for each frame is averaged over the polar scattering angle using the seven calorimeter rings. The fit to the $cos\phi$ is extremely good with a small reduced $\chi^2/\nu = 0.91$ and a high probability $p(\chi^2/\nu \geq 0.91) = 0.78$ to occur.
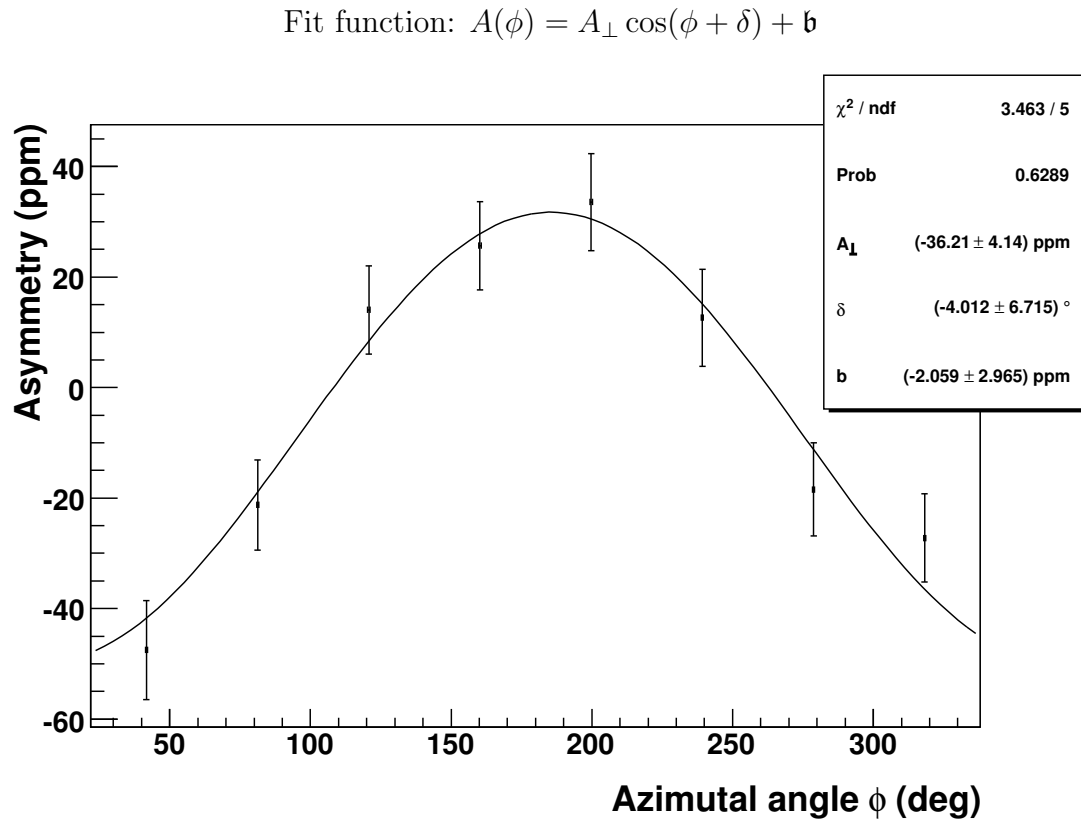
Fit function: $A(\phi) = A_\perp \cos(\phi + \delta) + \mathfrak{b}$

χ^2 / ndf	3.463 / 5
Prob	0.6289
$A_\perp$	(-36.21 ± 4.14) ppm
δ	(-4.012 ± 6.715) °
b	(-2.059 ± 2.965) ppm

Figure 5.10. The extracted raw asymmetries for the eight sectors show also an extremely good fit to the cosine function. This asymmetries are extracted with a lower cut corresponding to the dilution factor f=17%. Note that both the phase and the offset are compatible with zero.
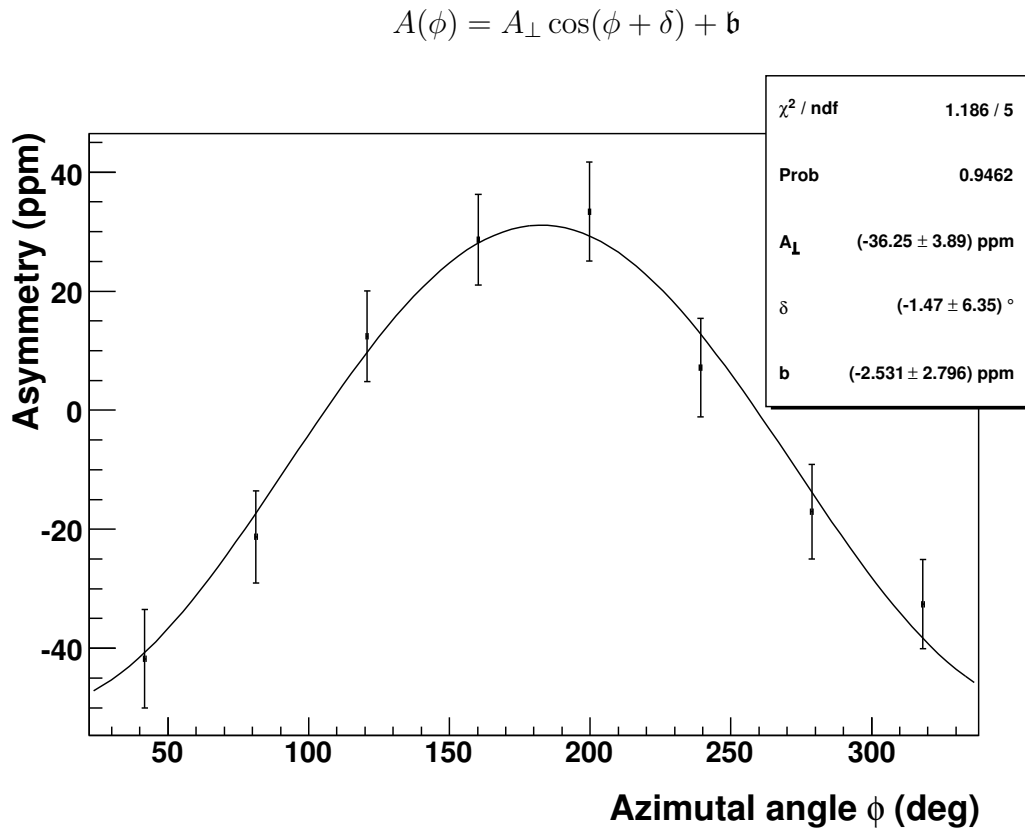
$$A(\phi) = A_\perp \cos(\phi + \delta) + \mathfrak{b}$$

Figure 5.11. Raw asymmetry extracted for the eight sector using the weighting procedure. Observe that the asymmetry error is smaller that those obtained using the different lower cuts.

5.4   Target density fluctuations and luminosity

The asymmetry that is aimed to be measured is properly an asymmetry in the cross section. The cross section in the elastic scattering is the quotient between the rate of the scattering events and the luminosity. The luminosity is the product of the incident particles flux and the target density. At first approximation it is sufficient the calculation of the asymmetry in the rates as the overall luminosity should be equal for both polarization states and therefore it cancels out.

The luminosity presents, though, helicity correlated fluctuations that lead to a change of the physical asymmetry. That is, the luminosity has a non zero asymmetry defined as:

$$A_L = \frac{L^+ - L^-}{L^+ + L^-} \tag{5.37}$$

Therefore the count rates should be normalized to the luminosity for both polarization states.

$$A = \frac{N^+/L^+ - N^-/L^-}{N^+/L^+ + N^-/L^-} \tag{5.38}$$

The asymmetry in the luminosity can be produced by an asymmetry in the beam current intensity and by an asymmetry in the effective target density. Let us write $L = I\rho$

$$A_L \approx \frac{dL}{2L} = \frac{d(I\rho)}{2I\rho} = \frac{\rho dI + I d\rho}{2I\rho} = \frac{dI}{2I} + \frac{d\rho}{2\rho} = A_I + A_\rho \tag{5.39}$$

The asymmetry in the beam current intensity is measured by means of the intensity monitors PIMO27 so that it can be separated from the luminosity asymmetry that therefore is a measure of the target density fluctuations. Instead of normalizing the asymmetry to the luminosity one can normalize it to the target density. The correction from the current asymmetry is postponed to the multi-linear regression method used to correct the physical asymmetry from the false asymmetries due to the helicity correlated differences in the beam parameters. This procedure will be explained in detail in the next section 5.5. The asymmetry will be normalized thus to the target density:

$$A = \frac{N^+/\rho^+ - N^-/\rho^-}{N^+/\rho^+ + N^-/\rho^-} \tag{5.40}$$

$$A \approx \frac{d(N/\rho)}{2N/\rho} = \frac{dN/\rho - N d\rho/\rho^2}{2N/\rho} = \frac{dN}{2N} - \frac{d\rho}{2\rho} = A_N - A_\rho \tag{5.41}$$

$$A \approx A_N - A_\rho \approx A_N - A_L + A_I \tag{5.42}$$

The asymmetry in the target density can be originated from helicity correlated target density fluctuations or from asymmetries in the process in which is based the measurement of the luminosity: the Møller scattering.

The target density fluctuations are strongly suppressed by the cooling system at the target cell with the target kept in a turbulent flow. The transverse spin Møller asymmetry is not negligible at all. Its order of magnitude is comparable to the transverse spin asymmetry in the elastic scattering off the nucleon. Moreover the Møller transverse spin asymmetry exhibits as well an azimuthal modulation with the $\cos\phi$. Therefore instead of normalizing the asymmetry extracted from one sector to the luminosity given by the corresponding opposite luminosity monitor the asymmetry will be normalized to the average luminosity over the eight luminosity monitors. Since the Møler transverse spin asymmetry averaged over the eight luminosity monitors, that cover the whole azimuthal angle, is expected to average out. A detailed analysis on the Møller asymmetry provided by the luminosity monitors will be presented in the next chapter.

5.5   Helicity correlated systematic errors. Beam parameters

The cross section of the elastic (or quasielastic) scattering off the nucleon (nucleus) is a function of both the beam energy E and the polar scattering angle θ, $\sigma = \sigma(E, \theta)$. Therefore any helicity correlated differences in the beam parameters like the beam energy, the beam position or the beam angle lead to trivial differences in the cross section for both polarization states which result in asymmetries we refer to as "false asymmetry″ or "apparative asymmetry″.

The beam parameter differences (for both polarization states) are: the beam energy difference ΔE, the horizontal beam position difference Δx, the vertical beam position difference Δy, the horizontal beam angle difference $\Delta\alpha$ and the the vertical beam position difference $\Delta\beta$. The false asymmetry due to the helicity correlated changes in the beam current intensity is also included in the multilinear regression through the beam current intensity asymmetry, defined as

$$A_I = \frac{I^+ - I^-}{I^+ + I^-} \tag{5.43}$$

It can be assumed a linear relation between the beam parameter difference $X_i = x_i^+ - x_i^-$ and the induced false asymmetry if the beam parameter difference is small enough.

$$A_{false} = \frac{\sigma(x + \Delta x) - \sigma(x)}{\sigma(x + \Delta x) + \sigma(x)} \approx \frac{\sigma(x) + \frac{d\sigma}{dx}\Delta x - \sigma(x)}{\sigma(x) + \frac{d\sigma}{dx}\Delta x + \sigma(x)} \tag{5.44}$$

$$\approx \frac{1}{2\sigma(x)}\frac{d\sigma}{dx}\Delta x = a \cdot \Delta x \tag{5.45}$$

the parameter a_i is the amount of false asymmetry generated by each unit of the beam parameter helicity correlated difference

$$a = A_{false}/X_i. \tag{5.46}$$

The measured asymmetry contains not only the physical asymmetry but also the contributions of the false asymmetries:

$$A_{meas} = P \cdot A_{ph} + \sum_{i=1}^{6} A_{false}^i \tag{5.47}$$

This relation can be written if the linear relation holds as:

$$A_{meas} = P \cdot A_{ph} + \sum_{i=1}^{6} a_i X_i \tag{5.48}$$

5.5.1 A model calculation of the false asymmetries

The false asymmetries can be evaluated with a simple model numerical calculation. In order to obtain the false asymmetry for one beam parameter one calculates the asymmetry in the rate of scattered electrons corresponding to no deviation of the beam parameters

$$R_0 = R_0(E, \theta, I) \tag{5.49}$$

and the rate with a slight variation of the corresponding beam parameter:

$$R_1 = R_1(E, \theta + d\theta, I) \tag{5.50}$$

The false asymmetry is:

$$A_{false} = \frac{R_1 - R_0}{R_1 + R_0} \tag{5.51}$$

The model is based in the assumption that the Rosenbluth cross section is a good approximation for the elastic scattering in order to obtain the false asymmetries, as trivial asymmetries in the cross section. This numerical calculation has been done for the backward angle configuration and the D_2 target (with the static approximation assumption $\sigma_d = \sigma_p + \sigma_n$). In this case $E = 315$ MeV and the current intensity is $I = 20$ μA.

Results of the calculation

The calculation has been done numerically. The table below shows the calculated parameters for every sector. Only the Δx and the $\Delta \alpha$ are calculated since due to the detector azimuthal symmetry they are related with the values of Δy and $\Delta \beta$ at different sectors.

Sector	$\Delta x(\mu m)$	$\Delta \alpha(\mu deg)$	$\Delta E(eV)$	A_I (ppm)
1	0.2433	0.0066	−0.0038	1.0000
2	0.1045	0.0028	−0.0038	1.0000
3	−0.0990	−0.0027	−0.0038	1.0000
4	−0.2433	−0.0066	−0.0038	1.0000
5	−0.2433	−0.0066	−0.0038	1.0000
6	−0.1045	−0.0028	−0.0038	1.0000
7	0.0990	0.0027	−0.0038	1.0000
8	0.2433	0.0066	−0.0038	1.0000

where the numbers listed in the table are the calculated false asymmetries corresponding to a helicity correlated variation of one unit of the beam parameter. The units are shown in parenthesis.

It can be observed that the false asymmetry owing to the beam energy difference ΔE is equal for the eight detector sectors, that is, it does not depend on the azimuthal angle. The effect of this false asymmetry is introducing an offset in the azimuthal transverse spin function $A_\perp = A_\perp^0 \cos\phi$. The false asymmetry associated with the beam current intensity asymmetry introduces an offset as well. On the other hand both the position and angle deviation false asymmetries present a modulation with the azimuthal angle given by $\cos\phi$. Because the deviation in the beam horizontal position, for example, must be projected for every sector depending on the azimuthal angle. As the horizontal position is modulated by a $\cos\phi$ and the vertical position by a $\sin\phi$ the overall effect of the beam position deviation will be a modulation in $\cos(\phi + \psi)$, that is, the effect of the beam position deviation will be the introduction of a phase ψ in the asymmetry azimuthal modulation. The same effect can be expected from the horizontal and vertical beam angle deviations.

5.5.2 Multilinear regression analysis

The asymmetry measured is the sum of the physical asymmetry A_{ph} reduced by the beam polarization degree P and the false asymmetries due to the helicity correlated differences in the beam parameters. The false asymmetries depend linearly on the helicity correlated beam parameter differences.

$$A_{meas} = P \cdot A_{ph} + \sum_{i=1}^{6} a_i X_i \qquad (5.52)$$

The measured asymmetry for every single run and the false asymmetries or the beam parameter differences present fluctuations. The beam parameter differences are measured for every run by means of the beam monitors. The multilinear regression analysis is used to obtain estimates of the fit parameters a_i that correspond to the false asymmetry per unit X_i. Once the fit parameter estimators are known the value of the asymmetry in the origin, that is, where all the $X_i = 0$ can be calculated. This extrapolation of the measured asymmetry to the case in which all the helicity correlated differences in the beam parameters are zero stands for the physical asymmetry, multiplied by the polarization degree.

$$P \cdot A_{ph} = \frac{1}{N} \sum_{i=1}^{N} \left(X_i^0 - \sum_{j=1}^{6} a_j X_i^j \right) \qquad (5.53)$$

The details of the multilinear regression method are presented in the appendix A. It has been assumed so far that the uncertainties ΔX_0 of the data points are all equal in order to simplify the formulae. If the uncertainties of the data points are not equal one must carry out the weighted fit. The details and the formulae of the weighted fit can be found in [3] and in [32]. In this section we present the equation to calculate the physical asymmetry subtracting the estimates of the fit parameters, that is, the false asymmetries 5.53. Below we present the formulae to calculate the errors in the estimates of the fit parameters and the error in the physical asymmetry.

The errors in the fit parameters and in the physical asymmetry are obtained from propagation of errors [32]

$$\Delta a^j = \frac{\Delta X^0}{\sqrt{N-1} s_{jj}} \sqrt{r_{jj}^{-1}} \qquad (5.54)$$

$$\Delta(P \cdot A_{ph}) = \sqrt{\frac{1}{N} + \frac{1}{N-1} \sum_{j=1}^{6} \sum_{k=1}^{6} \frac{\overline{X}^j}{s_{jj}} \frac{\overline{X}^k}{s_{kk}} r_{jk}^{-1}} \Delta X^0 \qquad (5.55)$$

In the work [3] there is a study of the linear regression for one dimension and two dimensions. This study gives some insight on how the errors depend on other parameters, like the mean of the beam parameter differences $\overline{X}$ and the standard deviation σ_X. The errors of the one dimensional linear regression analysis are the following:

$$\Delta a^j = \frac{\Delta X^0}{\sqrt{N-1}\sigma_{X^j}} \tag{5.56}$$

$$\Delta(P \cdot A_{ph}) = \sqrt{\frac{\sigma_A^2}{N} + \frac{\sigma_A^2}{N-1}\frac{\overline{X}}{\sigma_X}} \tag{5.57}$$

The comparison with the one-dimensional regression method is important because it permits the interpretation of what is happening during the analysis. Moreover, from the one-dimensional errors we can extract information about the conditions in which the multilinear regression method can be applied successfully [3].

Chapter 6

Results

In this chapter we present the results of applying the multilinear regression analysis to the raw asymmetries. The first section is devoted to the asymmetry in the signal. First we deal with the beam parameters and the application of the multilinear regression. Then several sources of systematic errors are discussed: the false asymmetries, the polarization degree and the deviation of the spin. Finally some plots and histograms are presented. The second section is centered in the investigations on the asymmetry in the noncoincidence energy spectrum.

The samples of runs that have been used in the analysis of the transversal data are shown in the table below. They correspond to two different beamtimes. The samples are divided in those labelled with GVZ=IN corresponding to the presence of the (sign changer) half-wave plate before the Pockels cell in the polarized beam source and those labelled with GVZ=OUT that means that the half wave plate (sign changer) has not been introduced. The measured values for each sample of the polarization P and the spin angle θ_S with their respective errors are also listed.

Sample	Run numbers	P	θ_S	GVZ
1	$44662 - 48000$	0.79 ± 0.03	$(90 \pm 4)°$	IN
2	$44802 - 44938$	0.79 ± 0.03	$(90 \pm 4)°$	OUT
3	$49153 - 49413$	0.87 ± 0.03	$(88 \pm 4)°$	OUT
4	$49415 - 49682$	0.87 ± 0.03	$(88 \pm 4)°$	IN

6.1   Asymmetry in the signal

6.1.1   Beam parameters

In the figure 6.1 one can see the beam parameter distributions for the all the runs used in the analysis of the transverse spin data. The beam parameter differences X_i exhibit some degree of dispersion. This dispersion is crucial for

the multilinear regression analysis. Actually the error in the physical asymmetry obtained using the multilinear regression method depends on the relation between the mean $\overline{X}$ and the degree of dispersion σ_X of the beam parameter difference. If the systematic error for the physical asymmetry is to be lower than the statistical error, $\sigma_{syst}(A_{ph}) < \sigma_{stat}(A_{ph})$ the parameters $\overline{X}$ and σ_X should fulfil the following relation:

$$\frac{\overline{X}^2}{(N-1)\sigma_X^2} < \frac{1}{N} \qquad (6.1)$$

This relation can be derived trivially from the formula of the asymmetry error in one dimension 5.57 if the first term in the square root is defined as the square of the statistical error and the second term is identified with the square of the systematic error (due to the false asymmetries). The relation above can be simplified to:

$$|\overline{X}| < \sigma_X \qquad (6.2)$$

The beam parameter differences distributions at the energy used at backward angles are such that the quotient between the mean and the standard deviation are greater than 1 except for the beam current asymmetry and the beam energy difference as one can see in the figure 6.1 where the mean and the standard deviation of the distributions are shown. This fact implies that the multilinear regression would yield large systematic error as the beam parameters are not enough dispersed compared to their distance to the origin. Therefore any attempt to extrapolate the asymmetry to the axis where $X_i = 0$ would yield a high uncertainty.

However the use of the GVZ half-wave plate allows to overcome this situation and makes it possible the performance of the multilinear regression.

6.1.2   The importance of the GVZ half-wave plate

As it was explained in the section 3.2 the half-wave plate is introduced to have some control on the systematic effects. Since it reverses the sign of the beam helicity, the physical asymmetry changes sign.

$$A_{ph} = \begin{cases} A_{ph} & \text{GVZ = OUT} \\ -A_{ph} & \text{GVZ = IN} \end{cases} \qquad (6.3)$$

On the other hand, the helicity correlated differences in the beam parameters are not sensitive to the presence of the GVZ half wave plate. The cause is that probably they are originated in the polarized beam source due to optical imperfections that are correlated with the Pockels cell voltage switching. Therefore the beam parameter differences are sensitive to the fast switch of the helicity produced
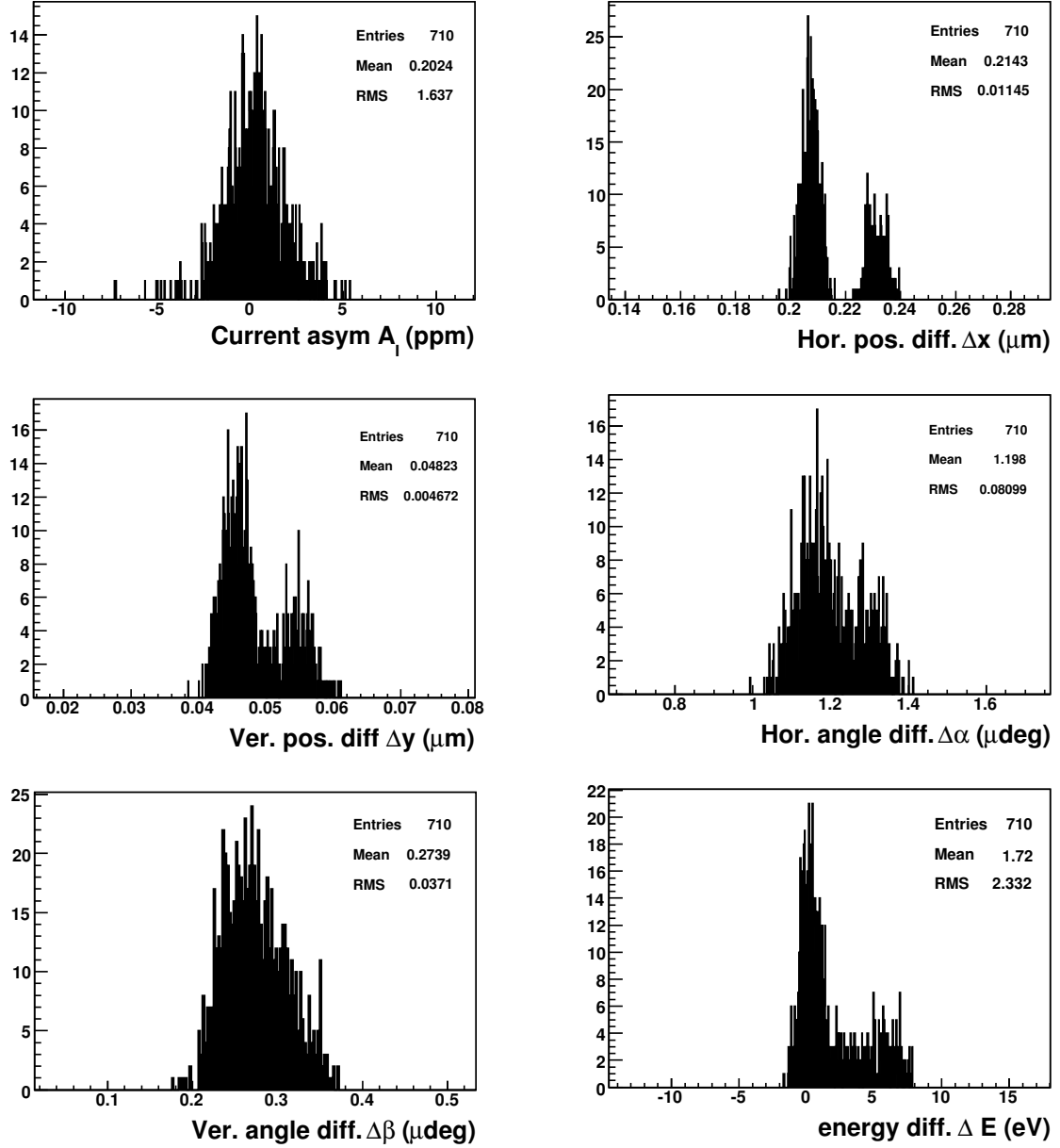
Figure 6.1. The distributions of the beam parameter differences for the transversal data are shown. From left to right and from up to down: Beam current intensity asymmetry A_I in ppm, horizontal beam position difference Δx in μm, vertical beam position difference Δy in μm, horizontal beam angle difference $\Delta \alpha$ in μdeg, vertical beam angle difference $\Delta \beta$ in μdeg, beam energy difference ΔE in eV.
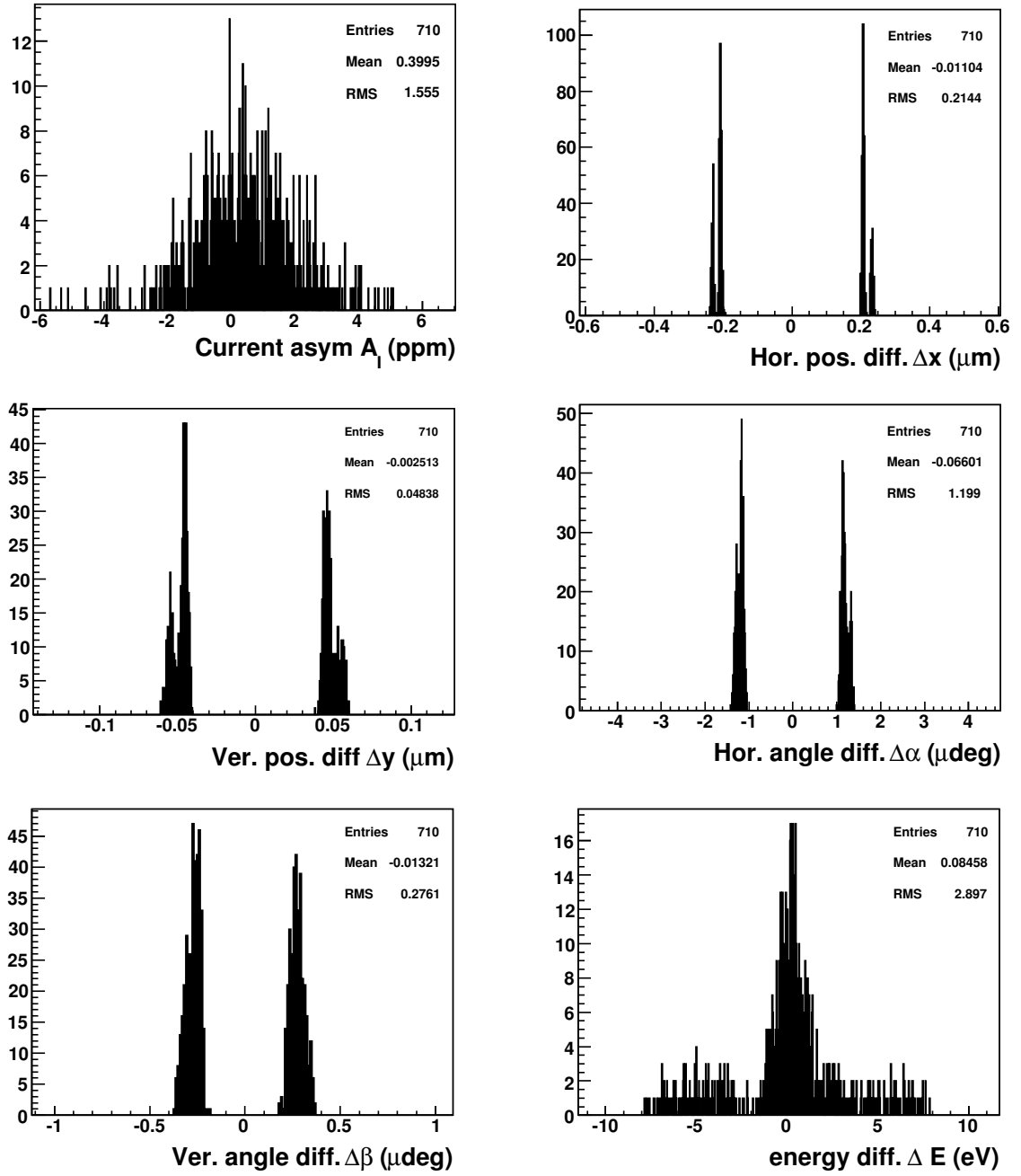
Figure 6.2. The distributions of the beam parameter differences for the transversal data are shown taking into account the different GVZ states. The difference with respect to 7.1 is that for the runs corresponding to GVZ=IN the sign of the beam parameters differences has been changed $X_i \rightarrow -X_i$ because of the sign rule 6.6. The multilinear regression is applicable now.

by the Pockels cell but they are not aware of the slow helicity flip due to the introduction of the GVZ half-wave plate. This fact has a great importance in the correction of the false asymmetries as they do not change their sign when the GVZ is introduced but at the same time the physical asymmetry does change the sign.

When the GVZ-OUT samples are combined with the GVZ-IN samples the sign of the measured asymmetry A_{meas} should be changed for the runs where GVZ is IN in order to take into account the changing of the physical asymmetry A_{ph} sign. Therefore when this changing sign rule is applied, the physical asymmetry recovers the sign corresponding to the GVZ-OUT samples but the false asymmetries change their sign simultaneously. This is equivalent to changing the sign of the beam parameter differences X as can be seen in the relations below:

For the runs where GVZ = OUT

$$A_m = A_{ph} + \sum_{i=1}^{6} a_i X_i \tag{6.4}$$

For the runs where GVZ = IN

$$A_m = -A_{ph} + \sum_{i=1}^{6} a_i X_i \tag{6.5}$$

$$-A_m = A_{ph} - \sum_{i=1}^{6} a_i X_i \tag{6.6}$$

As a consequence, the dispersion of the beam parameters, after combining the GVZ samples and applying the sign rule, becomes more symmetric (see figure 6.2), so that the σ_X gets larger and the mean $\overline{X}$ gets smaller. The relation 6.1 is thus fulfilled. This is a crucial feature of the multilinear regression method.

In the table below one can see the average $\overline{X}$ and the dispersion σ_X of the beam parameters in the beam conditions corresponding to the transversal data samples. The changing sign rule 6.6 has been applied to the beam parameter differences. For that reason they exhibit a good behaviour.

Beam	$\overline{X^j}$	σ_{X^j}	$\overline{X^j}/\sigma_{X^j}$
A_I (ppm)	0.4350	1.65	0.264
Δx (μm)	0.011	0.2143	0.051
Δy (μm)	-0.0025	0.048	0.052
$\Delta \alpha$ (μdeg)	-0.066	1.20	0.055
$\Delta \beta$ (μdeg)	-0.0132	0.276	0.048
ΔE (eV)	0.0846	2.90	0.029

It can be observed that the quotient $\overline{X}^j/\sigma_{X^j}$ is less than one in all the cases. It is similar in magnitude for the position and the angular beam parameters $\overline{X}^j/\sigma_{X^j} \sim 0.05$. The quotient is smaller for the beam energy difference and it is larger for the beam current intensity asymmetry.

6.1.3   The multilinear regression

The results shown here are all based on the analysis of a single sector (sector 8) but all sectors show in general the same behaviour.

As explained in the appendix A the multilinear regression method finally reduces to solving a matrix equation A.12

$$\mathfrak{r} = \mathfrak{R} \cdot \mathfrak{b}$$

where $\mathfrak{R}$ is the matrix (6×6) of covariances r_{jk} between the six beam parameters, and the independent terms column vector $\mathfrak{r}$ is composed of the covariances r_{j0} between the six beam parameters and the measured asymmetry. The column vector of unknowns $\mathfrak{b}$ is related to the false asymmetries coefficients a_k through the relation A.11.

As both the false asymmetries and the transverse spin asymmetry depend on the azimuthal angle the analysis is performed for every calorimeter sector. The matrix of beam parameter covariances for the sector 8 is shown below:

$$\mathfrak{R} = \begin{pmatrix} 1.0000 & 0.1165 & 0.1099 & 0.1153 & 0.1039 & -0.0446 \\ 0.1165 & 1.0000 & 0.9983 & 0.9996 & 0.9946 & 0.6295 \\ 0.1099 & 0.9983 & 1.0000 & 0.9979 & 0.9980 & 0.6521 \\ 0.1153 & 0.9996 & 0.9979 & 1.0000 & 0.9941 & 0.6318 \\ 0.1039 & 0.9946 & 0.9980 & 0.9941 & 1.0000 & 0.6598 \\ -0.0446 & 0.6295 & 0.6521 & 0.6318 & 0.6598 & 1.0000 \end{pmatrix}$$

where the rows from up to down and the columns from left to right correspond to the beam parameters in the following order: A_I, Δx, Δy, $\Delta \alpha$, $\Delta \beta$, ΔE.

The diagonal elements are identically 1 as they should. The off-diagonal elements correspond properly to the covariances between the different beam parameters. Note that the covariances of the current asymmetry with the rest of the beam parameters are ~ 0.1, quite less than one. It is evident that the position and angle beam parameters are strongly correlated among them with covariances close to 1. The beam energy difference presents also large covariances ~ 0.6, that is, it is also correlated with the position and angle beam parameters although it is not so strongly correlated as they are between them.

Below it is shown the $\mathfrak{r}_o$ column vector of the covariances between the measured asymmetry and every beam parameter.

$$
\mathfrak{r} = \begin{pmatrix}
-0.0004 \\
0.0443 \\
0.0422 \\
0.0453 \\
0.0412 \\
0.0218
\end{pmatrix}
$$

The output of the multilinear regression is listed below. The fit parameters a_i, that is, the false asymmetries per unit X_i are shown together with their error calculated from the equation 5.54. In the last column the one dimensional errors are listed, that is, the errors of the fit parameters if the correlations between the beam parameters are not taken into account.

X^j	$a_j \pm \sigma(a_j)$	$\sigma(a_j)_{1D}$
A_I (ppm)	1.76 ± 5.21	5.10
Δx (μm)	413 ± 1706	39..
Δy (μm)	5517 ± 59678	174.
$\Delta\alpha$ (μdeg)	-238 ± 257	7.
$\Delta\beta$ (μdeg)	-275 ± 547	31.
ΔE (eV)	-1.40 ± 4.48	3.0

One can see that the error of the fit parameters are quite large. The one dimensional errors are high and the strong correlations between beam parameters increase the errors even more. The statistics taken for the transversal data is low, chosen to obtain an error of 5% in asymmetries of several tens of ppm. On the other hand the false asymmetries per unit X_i are very small, less that 1 ppm. Therefore the relative errors for the fit parameters are expected to be large. Furthermore, as the beam quality has improved in the recent beamtimes the false asymmetries are lower than before, but the fluctuations of the beam parameters have also decreased. The reduction of the beam parameters dispersion implies that the errors of the fit parameters are larger than before (see equation 5.54).

Multilinear regression for the longitudinal data

The longitudinal data (that are taken with equivalent experimental conditions: backward angles, beam energy of 315.1 MeV and deuterium target) can be used as an alternative to estimate the fit parameters with lower errors. A larger measuring

time is spent to take longitudinal data because more statistics are needed to measure with an error of 5% the parity violating asymmetry, expected to be smaller than the transverse spin asymmetry. The multilinear regression fit is performed with the available longitudinal data to obtain the fit parameters with higher precision and accuracy. Afterwards the estimates of the fit parameters are used in the multilinear regression analysis performed with transversal data.

Analysis per sectors

In the table below we show the fit parameters obtained applying the multilinear regression method to the longitudinal data. The analysis has been carried out for every sector. In the table below the results corresponding to the sector 8 are shown. The fit parameters errors have improved but they are still quite large.

X^j	$a_j \pm \sigma(a_j)$	$\sigma(a_j)_{1D}$
A_I (ppm)	1.21 ± 2.67	2.65
Δx (μm)	86 ± 220	12.4
Δy (μm)	-362 ± 981	57.
$\Delta \alpha$ (μdeg)	0.84 ± 32	2.0
$\Delta \beta$ (μdeg)	25 ± 99	12.
ΔE (eV)	0.28 ± 0.88	0.49

Whole detector

The longitudinal spin asymmetry (parity violating asymmetry) does not present any azimuthal modulation. Performing the multilinear regression method on the whole detector allows to gain statistics and therefore it allows obtaining the fit parameters with lower errors. However, when integrating over the whole detector, the position and angle beam parameters cancel out. They are different depending on the sector considered. On the other hand, the beam current asymmetry and the beam energy difference do not depend on the azimuthal angle. As a consequence one can estimate the current and the energy fit parameters using the multilinear regression on the whole detector.

X^j	$a_j \pm \sigma(a_j)$	$\sigma(a_j)_{1D}$
A_I (ppm)	-2.26 ± 1.10	1.09
Δx (μm)	90 ± 91	5.1
Δy (μm)	-389 ± 4048	24
$\Delta \alpha$ (μdeg)	-8.6 ± 13	0.8
$\Delta \beta$ (μdeg)	-47 ± 41	5.0
ΔE (eV)	-0.50 ± 0.36	0.2

6.2   Physical asymmetry and systematic errors

The value of the fit parameters a_i yielded by the multilinear regression allows the subtraction of the false asymmetry and therefore the calculation of the physical asymmetry through the equation 5.53. Note that in order to extract the physical asymmetry the correction of the polarization degree is also applied.

6.2.1   Systematic error associated with the false asymmetries

A non orthodox mathematical multilinear regression is applied to correct the false asymmetries mixing both the multilinear regression done with the longitudinal data and the multilinear fit performed with the transversal data. Therefore the formula for the asymmetry error 5.55 is modified so that it includes the errors of the fit parameters provided by the longitudinal data fit and the covariances between the beam parameters corresponding to the beam conditions of the transversal data fit.

$$\Delta_{syst}^2(P \cdot A_{ph}) = \frac{\sigma_A^2}{N-1} \sum_{j=1}^{6} \sum_{k=1}^{6} \frac{\overline{X^j}\ \overline{X^k}}{s_{jj}\ s_{kk}}\ r_{jk}^{-1} \tag{6.7}$$

This formula corresponds to the second term of the equation 5.55. It is defined as the systematic error due to the false asymmetries.

$$\Delta_{syst}^2(P \cdot A_{ph}) = \sum_{j=1}^{6} \sum_{k=1}^{6} \frac{\sigma_A}{\sqrt{N-1}s_{jj}} \frac{\sigma_A}{\sqrt{N-1}s_{jj}} \overline{X^j}\ \overline{X^k}\ r_{jk}^{-1} \tag{6.8}$$

where the factors have been rearranged. Observe that the first two factors in the sum can be identified with the error of the fit parameter in the one dimensional case .

$$\Delta_{syst}^2(P \cdot A_{ph}) = \sum_{j=1}^{6} \sum_{k=1}^{6} \Delta_{1dim}(a_j)\, \Delta_{1dim}(a_k) \overline{X^j}\ \overline{X^k} r_{jk}^{-1} \tag{6.9}$$

This formula is the modified expression for the asymmetry systematic error. The first two factors $\Delta_{1dim}(a)$ are the one dimensional errors 6.2.1 of the fit parameters obtained by means of the longitudinal data fit. The following factors $\overline{X}$ correspond to the mean of the difference in the beam parameter calculated from the transversal data. The r_{jk} are the covariances between the beam parameters of the transversal data.

The systematic error of the physical asymmetry that one can associate with the false asymmetries due to the helicity correlated beam parameters fluctuations

is:

$$\Delta_{syst}^{false}(A_{ph}) = \frac{1}{\overline{P}}\sqrt{\sum_{j=1}^{6}\sum_{k=1}^{6}\Delta_{1dim}(a_j)\,\Delta_{1dim}(a_k)\overline{X^j}\;\overline{X^k}r_{jk}^{-1}} \qquad (6.10)$$

where $\overline{P}$ is the mean of the polarization degree.

6.2.2   Systematic error associated with the polarization

The polarization degree of the transversely polarized beam is, for the beamtimes that we are using in the analysis, $P = (0.79 \pm 0.03)$ and $P = (0.87 \pm 0.03)$. The relative error of the polarization degree is 4%. Now we want to calculate how the uncertainty in the measurement of the beam polarization contributes to the error of the physical asymmetry. For that purpose we start from the relation between the physical asymmetry, the beam polarization and the measured asymmetry:

$$A_{ph} = \frac{A}{P} \qquad (6.11)$$

where A stands for the right side of equation 5.53, that is the asymmetry without polarization correction. Using propagation of errors

$$\frac{\Delta A_{ph}}{A_{ph}} = \frac{\Delta A}{A} \oplus \frac{\Delta P}{P} \qquad (6.12)$$

From the equation 6.12 it can be understood that the precision of the polarization measurement is as important as that of the asymmetry. Now one can write the contribution to the asymmetry error of the polarization correction:

$$\Delta_{syst}^{Pol}(A_{ph}) = A_{ph}\frac{\Delta(P)}{P} \qquad (6.13)$$

6.2.3   Systematic error associated with the spin angle

In the table at the beginning of this chapter one can see the spin angle and the spin angle error given by the Transmission Compton Polarimeter. The spin is not completely perpendicular to the beam direction but it presents some deviation $\delta\theta_s$ from the 90°. Therefore there is a small longitudinal component of the spin. The flip of the transverse spin component originates a two photon exchange asymmetry $A_\perp$ and the flip of the longitudinal spin component gives rise to a parity violating asymmetry A_{PV}.

$$A_{ph} = A_\perp \cos\phi\cos\delta\theta_s - A_{PV}\sin\delta\theta_s \qquad (6.14)$$

A preliminary analysis of the longitudinal data taken so far has been carried out to obtain a measurement of the parity violating asymmetry for deuterium at backward angles. From the value of the asymmetry extracted from the transverse spin data A_{ph} and from the parity violating asymmetry the transverse spin asymmetry can be derived:

$$A_\perp = \frac{A_{ph}}{\cos \delta\theta_s} - A_{PV} \tan \delta\theta_s \qquad (6.15)$$

The correction to the measured asymmetry due to the spin angle deviation is give by :

$$\delta A_\perp = A_{ph} \left(1 - \frac{1}{\cos \delta\theta_s} \right) + A_{PV} \tan \delta\theta_s \qquad (6.16)$$

The numerical values are:

$$\delta A_\perp \approx 40 \cdot \left(1 - \frac{1}{\cos 2^\circ} \right) + 25 \cdot \tan 2^\circ = 0.9 \text{ ppm} \qquad (6.17)$$

Now we can obtain the systematic error of the transverse spin asymmetry arising from the error in the spin angle:

$$\Delta^2(A_\perp) = \frac{\Delta^2(A_{ph})}{\cos^2 \delta\theta_s} + \Delta^2(A_{PV}) \tan^2 \delta\theta_s + \left(\frac{A_{ph} \sin \delta\theta_s + A_{PV}}{\cos^2 \delta\theta_s} \right)^2 \Delta^2(\delta\theta_s) \quad (6.18)$$

The numerical values are:

$$\Delta_{syst}(A_\perp) = \left| \frac{A_{ph} \sin \delta\theta_s + A_{PV}}{\cos^2 \delta\theta_s} \right| \Delta(\delta\theta_s) \approx 25 \cdot 4^0 \cdot \frac{\pi}{180} = 1.4 \text{ ppm} \qquad (6.19)$$

6.2.4   Other systematic effects

We present here a brief discussion of other systematics effects:

- **Aluminium**: the transverse spin asymmetry in the cross section of the quasielastic electron-Al scattering. This asymmetry must be considered and subtracted from the measured asymmetry [3]. We need a model calculation of the transverse spin asymmetry in the quasielastic scattering off aluminium for backward angles. The model calculation is not yet available, though.

- **Pile-up**: the pile-up events in the calorimeter may present helicity correlated differences that lead to a false asymmetry in the measured rate [22]. This pile-up asymmetry has not been corrected in the frame of this work. We

expect, though, a small contribution since the pile-up effects strongly depend
on the count rate and the count rate at backward angles is much smaller than
the count rates at the forward angle configuration.

- **Nonlinearity of luminosity**: The measurement of the luminosity signal
  through the luminosity monitors is not linear. This nonlinearity in the lumi-
  nosity signal must be corrected so that the normalisation of the asymmetry
  to the target density can be done properly. We will discuss this subject in
  more detail in the chapter 7. We advance that the nonlinearity of the lumi-
  nosity signal is not yet corrected. However we expect a negligible influence
  of the luminosity nonlinearity on the asymmetry of the signal because the
  target density fluctuations are strongly suppressed.

6.2.5   Results

The table below shows the corrected asymmetry for every sector. In the sec-
ond column the systematic errors due to the false asymmetries are listed. They
represent a small contribution to the total error. In the last column the errors
associated with the polarization correction of data appear.

Sector	$\mathrm{A}^{Ph}_{correct}(10^{-6})$	δ_A^{syst}	δ_A^{pol}
1	-49.56 ± 11.05	0.75	1.96
2	-26.52 ± 10.24	1.02	1.00
3	$22.24 \pm\ \ 9.95$	0.74	0.92
4	33.65 ± 10.00	0.75	1.38
5	41.29 ± 10.33	0.79	1.67
6	6.16 ± 14.24	0.85	0.29
7	-18.14 ± 10.43	0.79	0.70
8	-38.38 ± 10.43	0.86	1.49

The distribution of the transverse spin asymmetries for the sector 8 can be seen
in the figure 6.3. The data fits perfectly to a Gauss distribution. In the figure 6.4
the GVZ-OUT and the GVZ-IN samples have been separated. In green one can see
the OUT asymmetry distribution fitted to a gaussian. The asymmetry distribution
corresponding to GVZ-IN is plotted in red. The means of the distribution are
opposite in sign and compatible in magnitude. This is an evidence of a good
behaviour of the asymmetry under the GVZ half-wave plate.

The physical asymmetry exhibits the azimuthal modulation with the $\cos\phi$ as
one can see in the figure 6.5. In this figure the physical asymmetry normalized
to the target density, corrected from the false asymmetries and corrected from
the beam polarization degree has been plotted. The fit to the function $A(\phi) =$

$A_\perp \cos(\phi + \delta) + \mathfrak{b}$ is extremely good. The phase δ and the offset b are compatible with zero.

The figure 6.6 shows the corrected physical asymmetry corresponding to the samples with GVZ=OUT. As it is normal the fit is a little worse but still acceptable. The amplitude has the correct negative sign. The phase δ is compatible with zero but there is a small offset b. On the other hand the figure 6.7 contains the corrected physical asymmetries corresponding to the samples with GVZ=IN. One observes a better goodness of the fit. The sign of the amplitude is reversed as it should be. There is also a small offset but it has the same sign as the OUT asymmetry offset so that when combining the data (the sign of the GVZ=IN samples is reversed) they cancel out.

In order to calculate the normal spin asymmetry we can use, instead of the $\cos \phi$ fit procedure, the collection of the asymmetries found for each sector multiplied by a suitable geometric factor, due to the azimuthal dependence of the transverse spin asymmetry. This procedure, explained in detail in [3] takes into account the different angular widths (in number of frames) of the sectors employed in the analysis. The geometrical factors F_s are defined by

$$F_s = \frac{\int_{\phi_1}^{\phi_2} d\phi}{\int_{\phi_1}^{\phi_2} \cos \phi d\phi} \tag{6.20}$$

The total asymmetry is calculated from the asymmetries for each sector multiplied by the geometrical factor F_s:

$$A_{ph} = \frac{1}{P} \frac{1}{8} \sum_{s=1}^{8} F_s A_s^{ph} \tag{6.21}$$

The result of the asymmetry given by this procedure is

$$A_{ph} = (-48.90 \pm 2.64_{stat} \pm 0.83_{syst})\text{ppm} \tag{6.22}$$

the second term $stat$ stands for the statistical error and the third term $syst$ stands for the systematic error (it includes the contribution of the false asymmetries and the normalization to the target density).

In the table below we show the contribution to the systematic error from the different background processes:

	Systematic error contribution
False asymmetries	0.62 ppm
Target density	0.55 ppm
Polarization	1.92 ppm
Model parameter ϵ	0.25 ppm
Model parameter δ	1.3 ppm
Spin deviation	1.4 ppm
Aluminium	—
Pile-up	—
Nonlinearity LuMo	—
Total	2.84 ppm

Average over the whole detector   The regression method is applied also to the whole detector. That is the asymmetries calculated using all the modules. This whole asymmetry is expected to be zero because it is azimuthally modulated by a $\cos\phi$ whose average over the whole azimuthal angle is zero. Both the raw asymmetry and the corrected asymmetry yields are compatible with zero as it is expected.

$A_{raw}^{Ph}(10^{-6})$	$A_{correct}^{Ph}(10^{-6})$	δ_A^{syst}
-2.79 ± 3.85	-1.92 ± 3.91	0.58
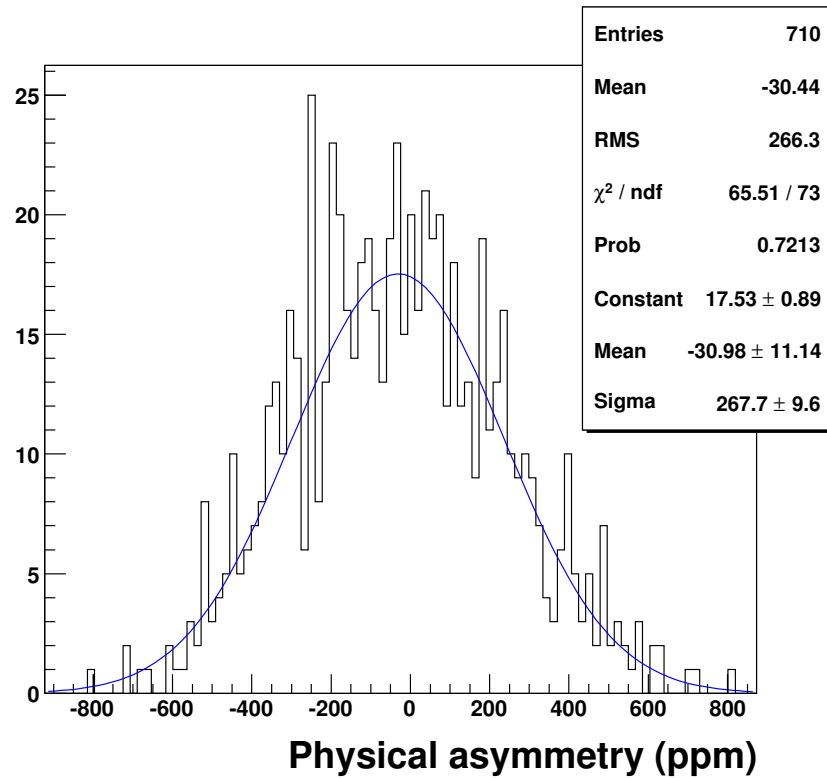
Figure 6.3. The distribution of the asymmetries extracted for the sector 8 using all the runs corresponding to transverse spin data. The asymmetry distribution fits extremely well to a Gauss.
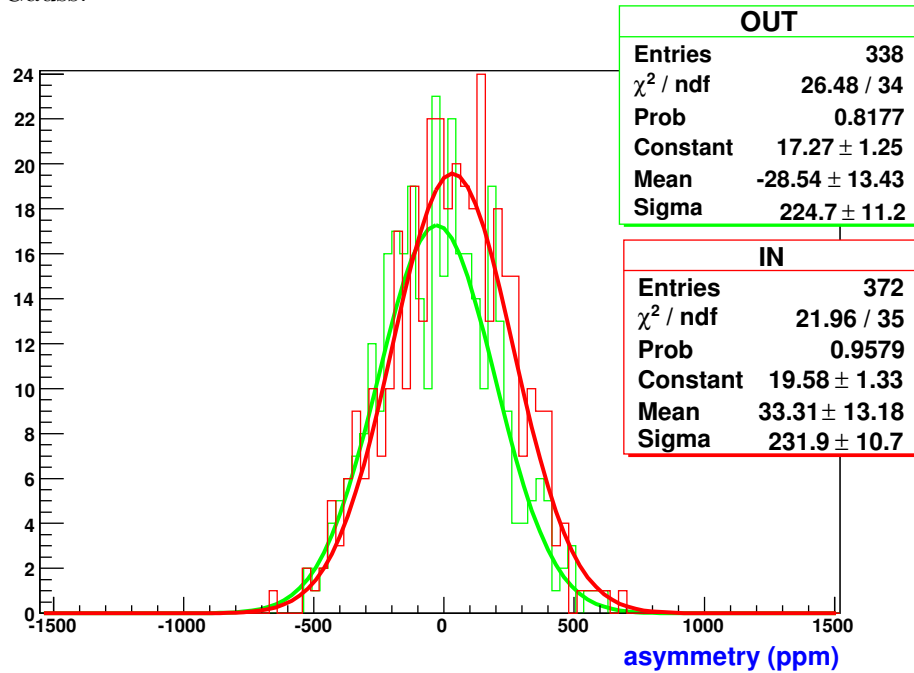
Figure 6.4. In figure raw asymmetries extracted for sector 8 are shown for every 5 minutes run used in analysis. The fluctuation of asymmetry does not present any obvious deviation from statistical behaviour.

$$\text{Fit function: } A(\phi) \quad = \quad A_\perp \cos(\phi + \delta) + \mathfrak{b} \tag{6.23}$$
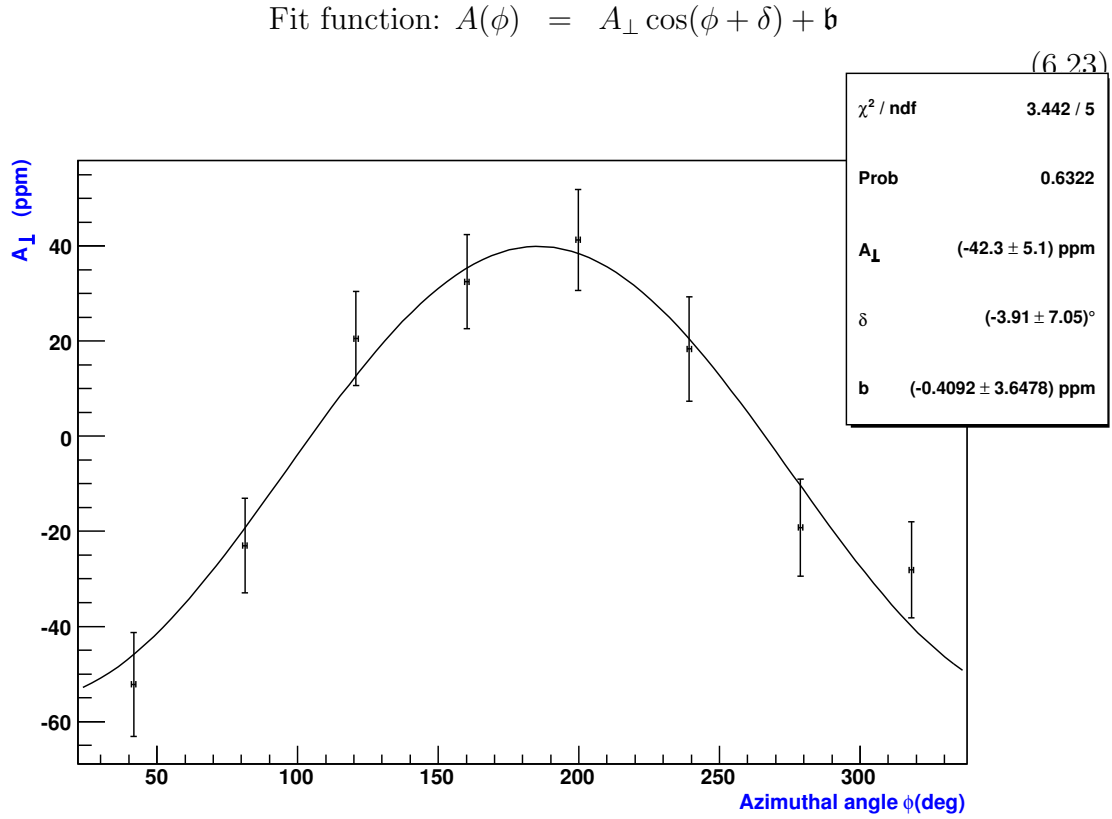
Figure 6.5. Extracted transverse single spin asymmetries for the eight sectors of calorimeter. They show a clear dependence on azimuthal scattering angle ϕ. Fit of curve $\cos\phi$ to asymmetries is astonishing good with a very small reduced χ^2 and a near one probability to occur. So extremely good fit has been also found independently for H_2 data [4]. It is probably a consequence of the higher quality in beam conditions, with respect to measurements at forward angles.

$$\text{Fit function: } A(\phi) \;=\; A_\perp \cos(\phi + \delta) + \mathfrak{b}$$

(6.24)

Figure 6.6.

Figure 6.7.

Fit function: $A(\phi) \;\; = \;\; A_\perp \cos(\phi + \delta) + \mathfrak{b}$

(6.25)

χ^2 / ndf	1.531 / 5
Prob	0.9094
A_L	(-44.28 ± 4.94) ppm
δ	(-2.8974 ± 6.5850)°
b	(-1.306 ± 3.544) ppm
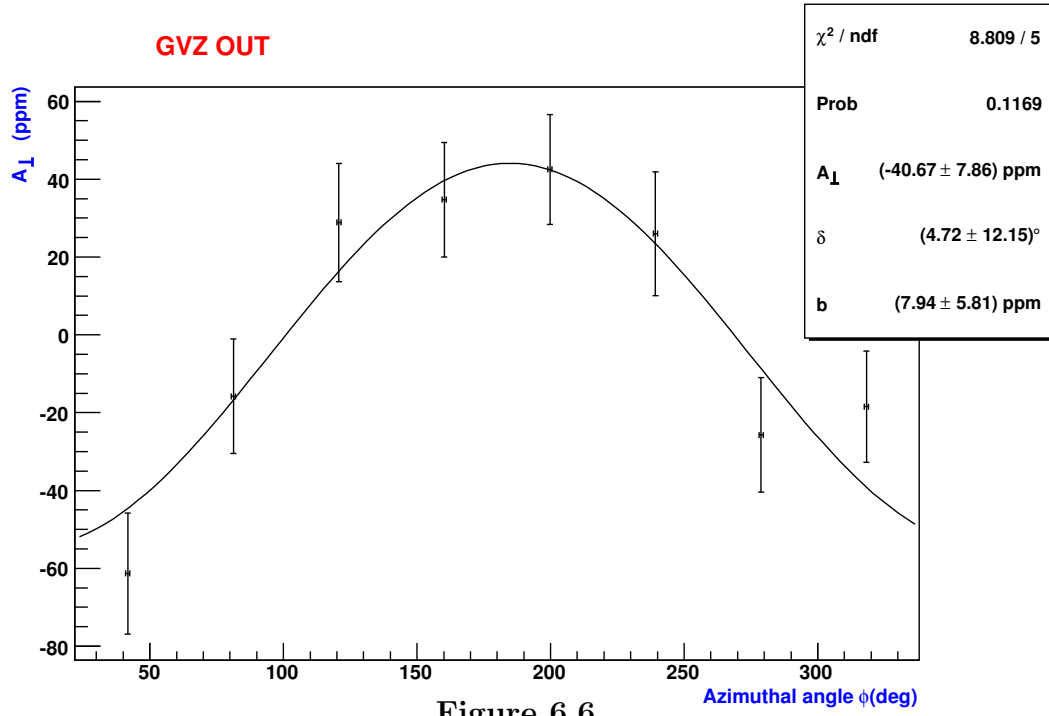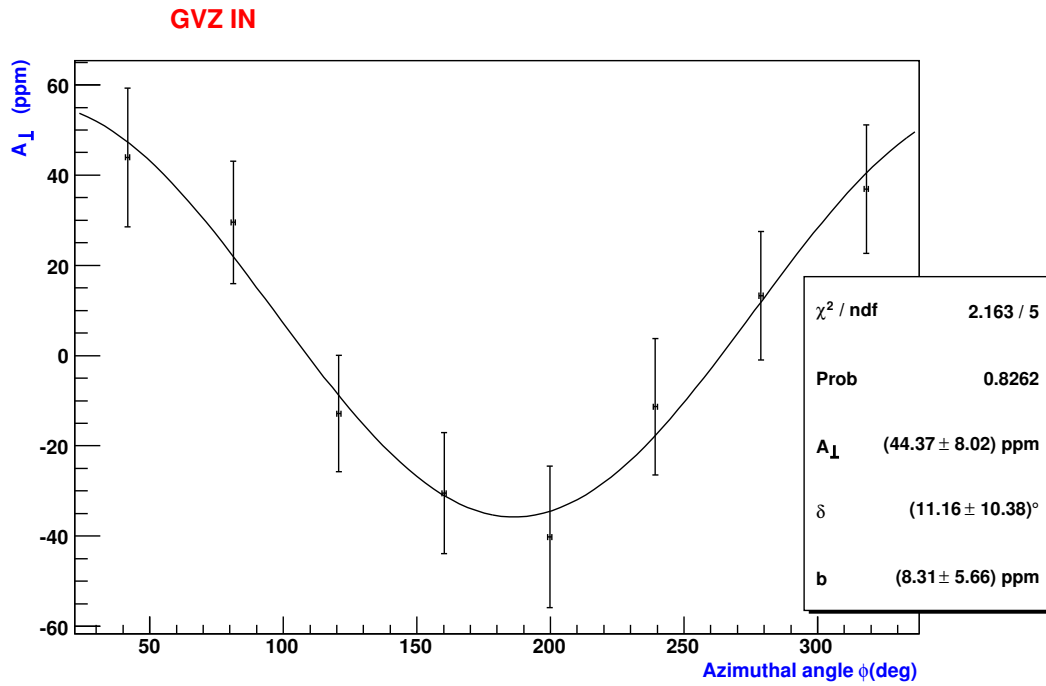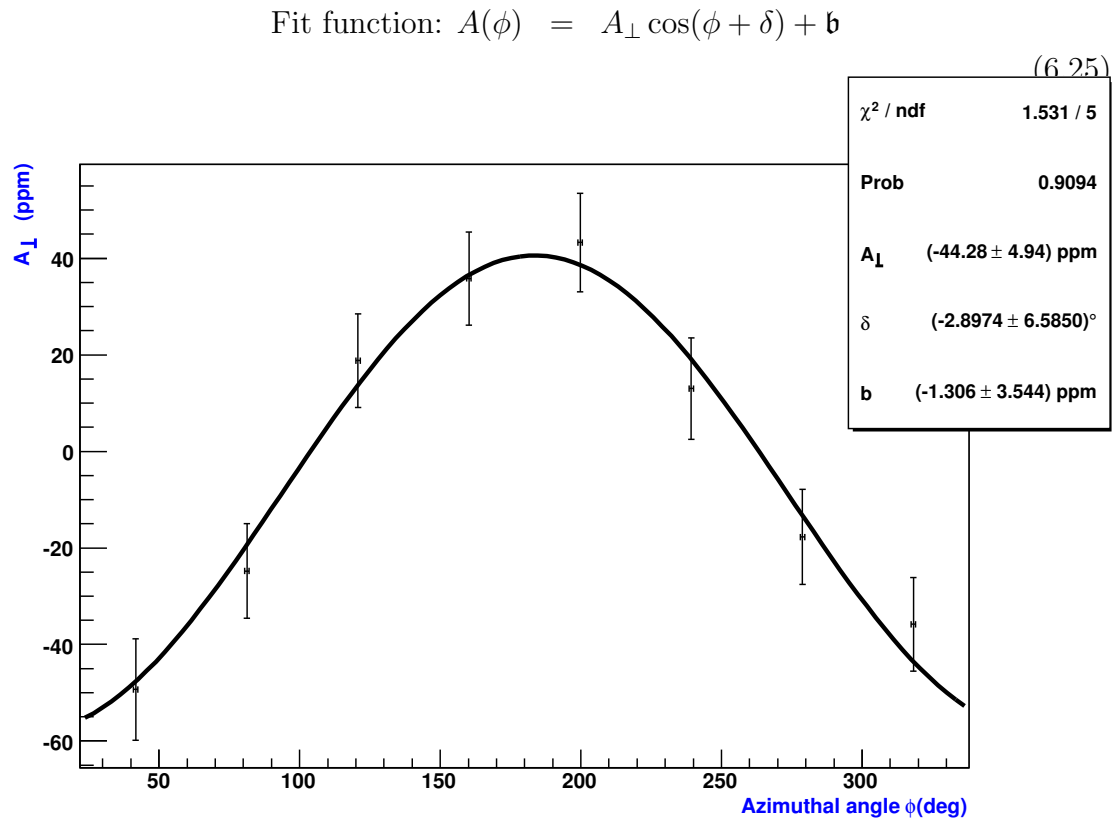
Figure 6.8. This plot corresponds to asymmetries obtained applying the weighting procedure. They have been normalized to effective target density. Also multilinear regression analysis have been used to correct false asymmetries.

6.3 Asymmetry in the noncoincidence energy spectrum

The normal spin asymmetry in the noncoincidence energy spectrum is also investigated. For the asymmetry in the background a similar behaviour was expected to that of the asymmetry in the signal, that is, an azimuthal modulation with the $\cos\phi$. Moreover, we expect the asymmetry in the background to vary with the energy cut because the neutral background is constituted by several physical processes with different asymmetries.

The asymmetry in the noncoincidence spectrum, defined by the equation 5.12, is calculated in parallel to the asymmetry in the quasielastic scattering, applying the shifted energy cuts, as explained in the section 5.2.1. This background asymmetry has been normalized to the target density, corrected from the false asymmetries and the polarization degree. In the figure 6.9 the results of the analysis for the background asymmetry are shown in function of the azimuthal angle. The top panel shows the background asymmetry extracted from the samples of runs with GVZ=OUT. The panel in the middle shows the background asymmetry extracted from the samples with GVZ=IN. And the bottom panel shows the background asymmetry extracted from all the samples (with GVZ=OUT and GVZ=IN) collected, as explained in the section 6.1.2. The asymmetry in the background for the collected samples exhibits the expected $\cos\phi$ azimuthal dependence. However the asymmetries separately extracted from each GVZ set deviate from the expected behaviour and exhibit unexplained oscillations. The oscillations are such that the expected $\cos\phi$ azimuthal modulation is recovered if both GVZ samples are combined.

The following function fits quite well to the asymmetry in the background for the separated GVZ samples

$$A_\perp = A_1 \cos\phi - A_2 \sin 2\phi + b \tag{6.26}$$

the $\cos\phi$ term is motivated by the expected azimuthal dependence of the transverse spin asymmetry and the second term is motivated by the dependence of the pion electroproduction cross section on $\sin 2\phi$. Several combinations of circular functions depending on ϕ and 2ϕ have been tested. The function 6.26 seems to be the best function to fit the data.

We expected the first term to change sign with the GVZ, as it probably arises from the two photon exchange physics. On the other hand we expected the second term not to change sign so that when both GVZ samples are combined the $\sin 2\phi$ terms would cancel out (since the GVZ=IN samples are changed of sign to collect all the GVZ samples).

From figure 6.9 one can observe that the amplitude of the $\sin 2\phi$ in both GVZ

samples are of similar magnitude (equal inside the error margin) and of equal sign, as they should if they are to cancel out when the GVZ samples are combined. Nevertheless the astonishing fact is that the $\cos\phi$ amplitudes are of different magnitude, the difference is large, and for the cuts selected (corresponding to the dilution factor $f = 17\%$), they are even of the same sign. If the cosine term would be originated only from the two photon exchange physics the amplitudes should be equal and of opposite sign. So we can see that the sine terms cancel out when the GVZ samples are combined and the cosine amplitude of the combination is just the average of the cosine amplitudes of the separated samples.

In the table below we show the results of the fit of the function 6.26 to the asymmetry in the noncoincidence spectrum for different energy cuts, corresponding to different dilution factors in the coincidence spectrum. In the first column one can see the fit amplitudes for the GVZ-OUT samples, in the middle the fit results for the GVZ-IN samples and the right column shows the fit amplitudes for the combined samples. The cosine amplitude A_1 is shown in the top and the sine amplitude A_2 is shown in the bottom.

f	OUT	IN	A_{OUT}-A_{IN}
11%	55±7	111±7	−31±5
	81±8	70±8	1±5
14%	34±6	108±6	−40±4
	73±7	62±7	1±4
17%	15±6	112±6	−53±
	68±6	61±6	−1±4
20%	4±5	116±5	−59±3
	61±6	55±6	−1±3
23%	−7±5	114±6	−63±3
	51±6	42±6	0±3
29%	−21±4	110±5	−67±2
	40±5	41±5	−2±2

One can observe that the A_1 of the GVZ=OUT set decreases as the lower cut is moved to the left, that is, for increasing dilution factor (see figure 6.10). For higher energy cut (small dilution factor) the A_1 is positive, at middle energy it crosses zero and at low energy it becomes negative. The A_2 also decreases (from 80 ppm to 40 ppm) when the lower cut is moved to the left but it keeps the positive sign. The A_1 of the GVZ=IN samples remains quite stable, around 110 ppm as the cut is moved. The A_2 of the GVZ=OUT also decreases. It is a little smaller than that of the GVZ=OUT part but they are compatible in magnitude. The A_1 of the combined data is negative and increases in magnitude as the lower energy cut
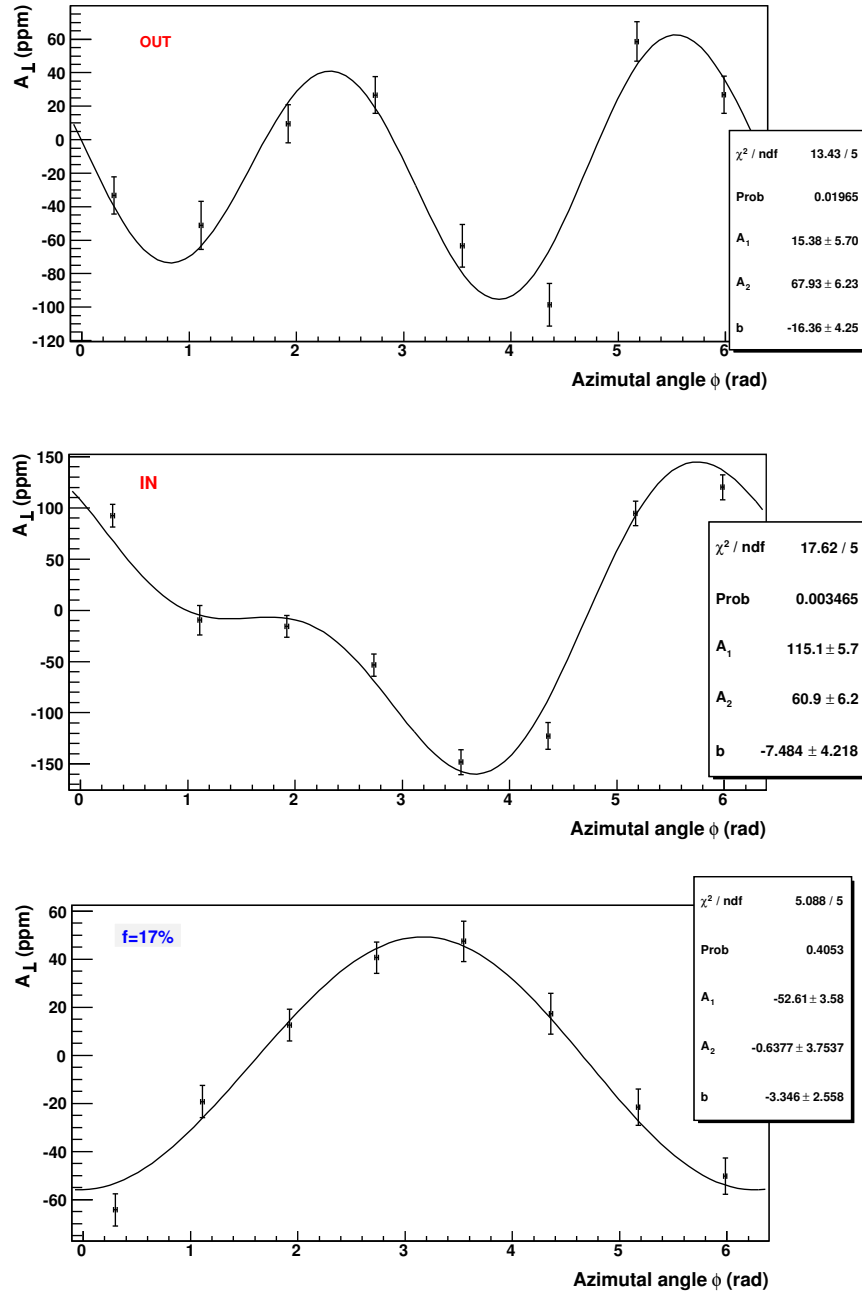
Figure 6.9. The results of the analysis for the asymmetry in the noncoincidence energy spectrum are shown in function of the azimuthal angle. The top panel shows the background asymmetry extracted from the samples of runs with GVZ=OUT. The panel in the middle shows the background asymmetry extracted from the samples with GVZ=IN. And the bottom panel shows the background asymmetry extracted from all the samples (with GVZ=OUT and GVZ=IN) collected, as explained in the section 6.1.2. The asymmetry in the background for the collected samples exhibits the expected $\cos\phi$ azimuthal dependence. However the asymmetries separately extracted from each GVZ set deviate from the expected behaviour and exhibit unexplained oscillations. The oscillations are such that the expected $\cos\phi$ azimuthal modulation is recovered if both GVZ samples are combined.

Figure 6.10.
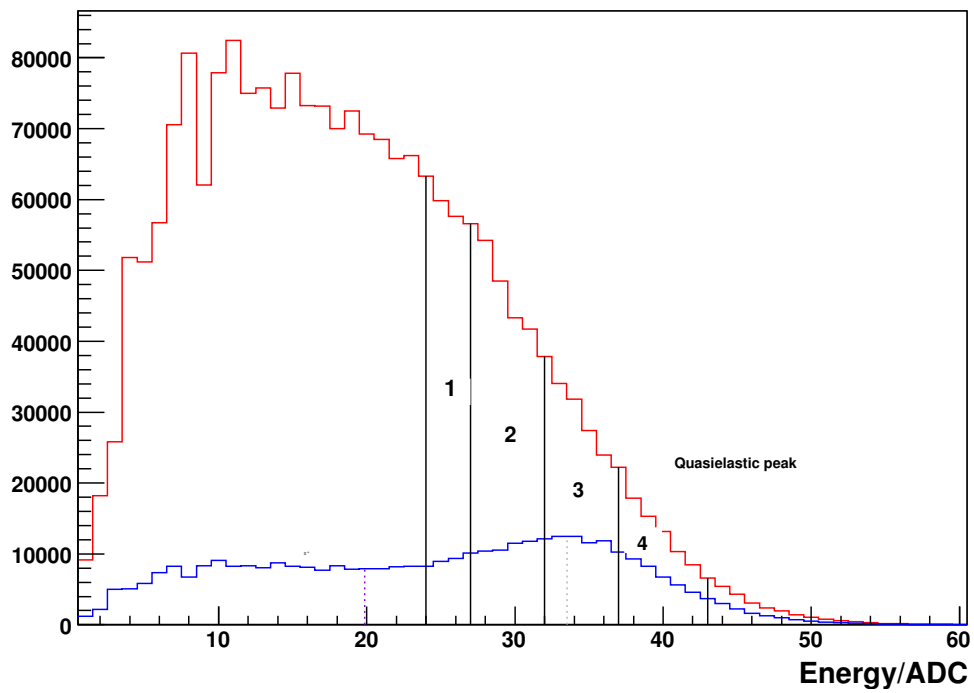
Figure 6.11.

is moved towards the lower energies. The A_2 of the combined data is compatible with zero.

As there is a clear dependence of these amplitudes with the energy we have divided the noncoincidence spectrum in strips whose borders are defined by the energy. That is all the modules and all the runs have cuts corresponding to the same energy. The energy strips for the noncoincidence spectrum are shown in the figure 6.11.

We have performed this analysis for both the transversal data and the longitudinal data, both corresponding to the D_2 target. The figure 6.12 shows the asymmetry in the noncoincidence spectrum for the transversal data with D_2 target. The figure 6.13 shows the asymmetry in the noncoincidence spectrum for the longitudinal data with D_2 target. The table below shows the results of the fit to the function 6.26 for the transversal and longitudinal data, corresponding to the four energy strips.

TRANS			LONG		
OUT	**IN**	$\mathbf{A_{OUT}}$-$\mathbf{A_{IN}}$	**OUT**	**IN**	$\mathbf{A_{OUT}}$-$\mathbf{A_{IN}}$
-48 ± 6	116 ± 6	-83 ± 4	40 ± 2	38 ± 3	11 ± 1
32 ± 7	32 ± 7	-1.5 ± 4	34 ± 2	43 ± 4	5 ± 1
-11 ± 5	-20 ± 7	5 ± 3	-6 ± 2	-6 ± 2	-1 ± 1
-11 ± 7	125 ± 7	-71 ± 4	55 ± 2	58 ± 3	10 ± 2
55 ± 7	55 ± 7	-3 ± 5	50 ± 2	53 ± 4	9 ± 2
-18 ± 5	-11 ± 5	-2 ± 3	-6 ± 2	-8 ± 3	-1 ± 1
59 ± 9	112 ± 9	-31 ± 6	75 ± 3	83 ± 4	16 ± 2
76 ± 5	78 ± 10	-5 ± 6	75 ± 3	75 ± 4	19 ± 2
-21 ± 7	-13 ± 7	-3 ± 4	-5 ± 2	-8 ± 3	-0.3 ± 1.4
149 ± 17	45 ± 16	48 ± 12	100 ± 4	121 ± 6	16 ± 3
119 ± 18	92 ± 17	9 ± 12	104 ± 5	110 ± 6	23 ± 14
-36 ± 12	-7 ± 12	-14 ± 8	-9 ± 3	-16 ± 4	0.75 ± 2

These data suggests that there is a contribution of

$$b_1 \cos \phi + A_2 \sin 2\phi \tag{6.27}$$

that does not change of sign when the GVZ is introduced. This components increase with the energy and they are present, we assume, in both the transversal and the longitudinal data. We make the hypothesis that these components, as they are independent of the two photon exchange physics, have the same magnitude in both the transversal and longitudinal data.

On the other hand there is a component

$$a_1 \cos \phi \tag{6.28}$$

whose sign is reversed by the GVZ and that probably arises from the two photon exchange physics. This component is only present in the transversal data. The amplitude a_1 decreases with the energy (the magnitude decreases with the energy but because it is negative it becomes less negative).

This model can explain the difference in the amplitude of the cosine for the separated GVZ sets and why the amplitude corresponding to the GVZ=OUT varies with the energy and the amplitude of the GVZ=IN remains approximately constant.

For the GVZ=OUT both cosine terms combine so that $a_1 + b_1 = A_1$ increases with the energy. For low energies the a_1 dominates so that A_1 is negative. For high energies the b_1 dominates and therefore the A_1 is positive. On the contrary for the GVZ=IN the sign of the a_1 is reversed and the sign of the b_1 is not reversed and therefore when they are combined the sum remains constant. This model can not explained, though, some inconsistencies of the data like those appearing in the energy strip 4.
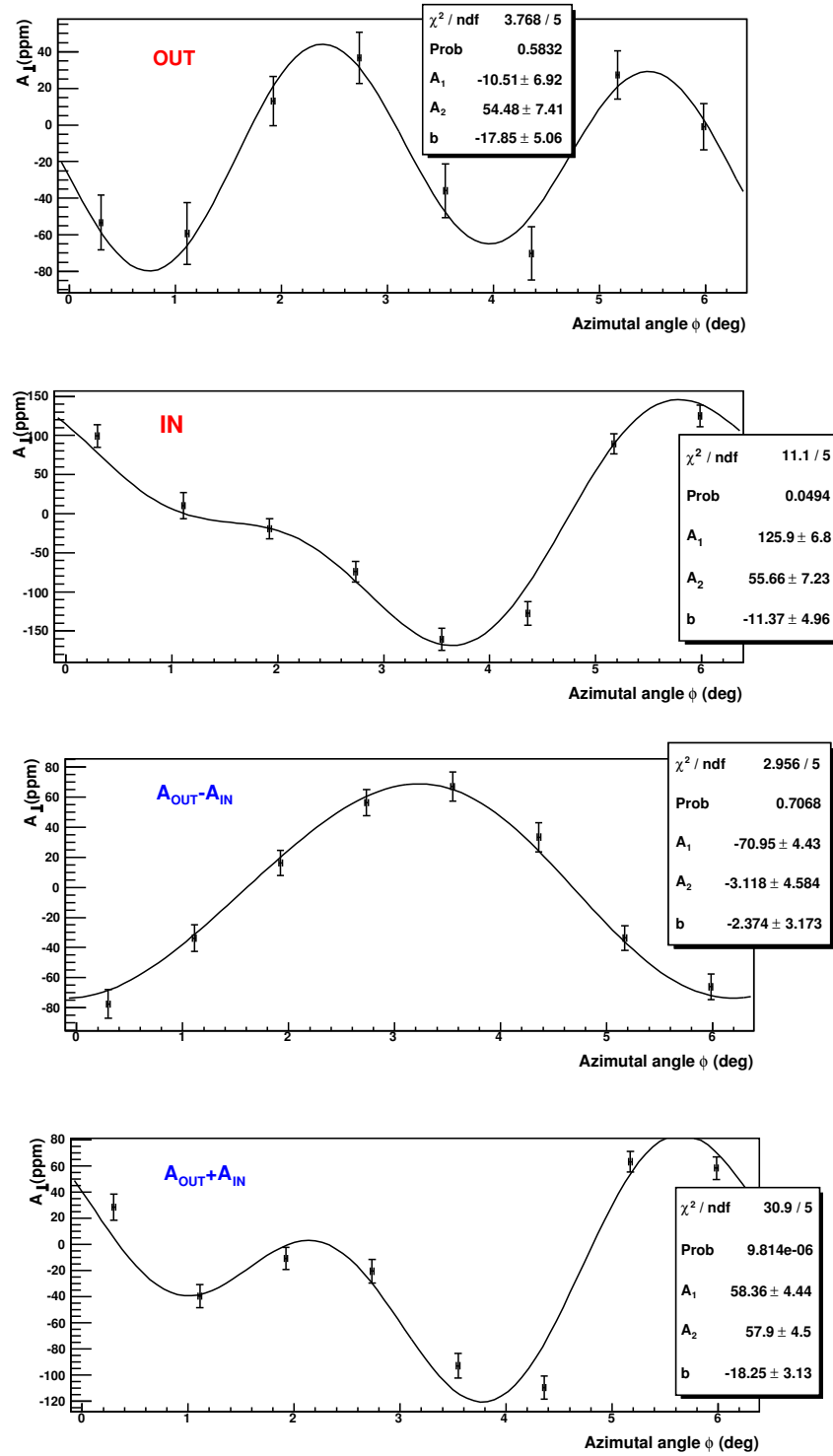
Figure 6.12. The transverse spin asymmetry in the noncoincidence spectrum (energy strip 2) is shown. The top panel shows the asymmetry calculated from GVZ=OUT samples separately. The panel below shows the asymmetry calculated from GVZ=OUT samples. The third panel (from top) shows the asymmetry calculated with all GVZ samples combined (changing the sign of GVZ=IN asymmetries) and the botton panel shows the combination of all GVZ samples without changing the sign of GVZ=IN asymmetries.
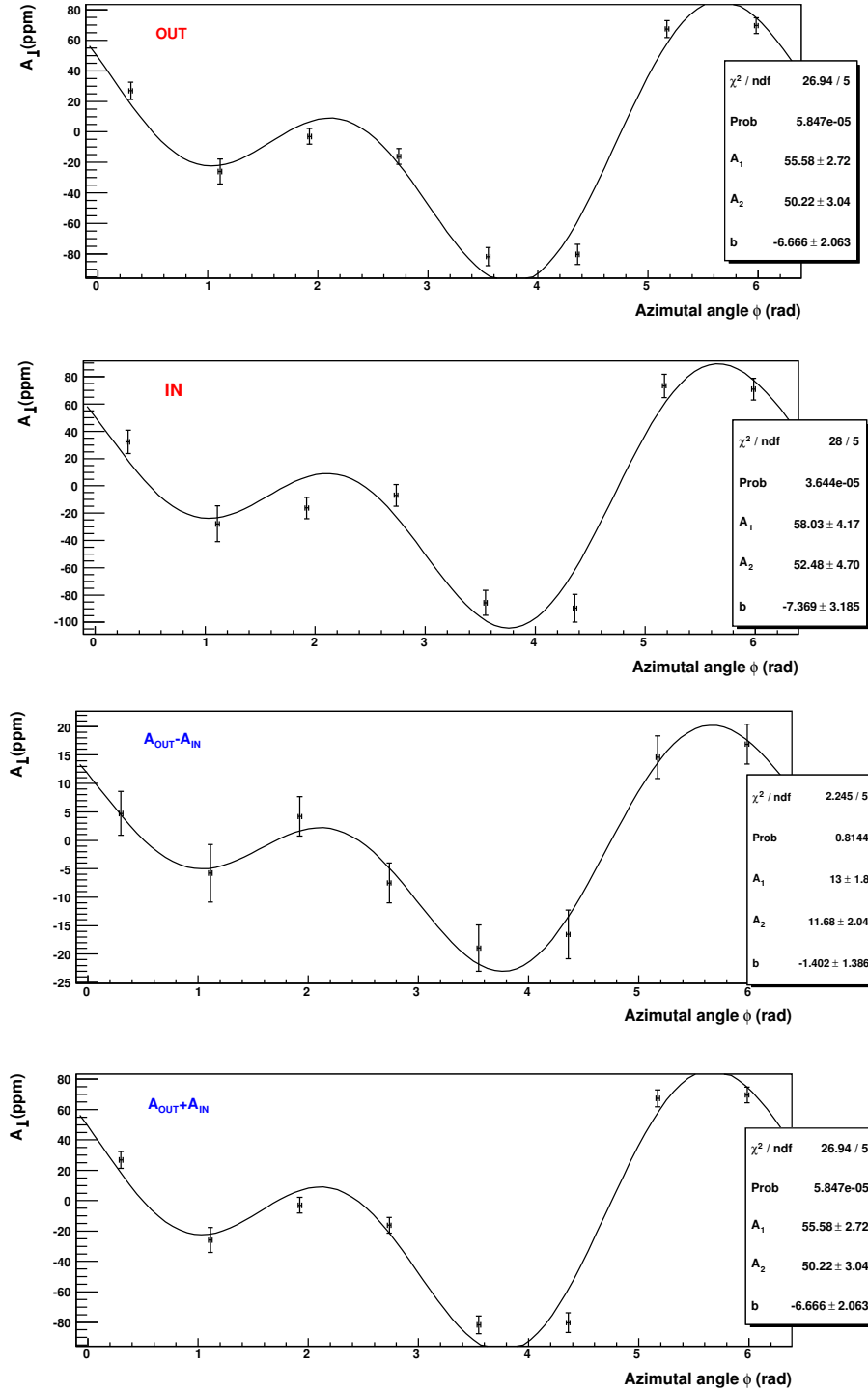
Figure 6.13. The transverse spin asymmetry in the noncoincidence spectrum (energy strip 2) is shown. The top panel shows the asymmetry calculated from GVZ=OUT samples separately. The panel below shows the asymmetry calculated from GVZ=OUT samples. The third panel (from top) shows the asymmetry calculated with all GVZ samples combined (changing the sign of GVZ=IN asymmetries) and the botton panel shows the combination of all GVZ samples without changing the sign of GVZ=IN asymmetries.

6.3.1   Comparison in different experimental conditions

In order to obtain information about the unexpected and unknown behaviour of the asymmetry in the noncoincidence energy spectrum the asymmetries can be investigated under the different A4 experimental conditions.

- Dependence on energy.

- Transversal data and longitudinal data.

- Signal and background (coincidence and noncoincidence spectra).

- H_2 target and D_2 target.

- Forward angle configuration and backward angle configuration.

- Asymmetry in the luminosity monitors.

The first two points have been treated before.

There is evidence that there are also azimuthal modulations described by the fit function 6.26 in the noncoincidence asymmetry of the hydrogen data, see figure 6.14. This effect is thus not exclusive of the deuterium. However the amplitude of the sine is relatively smaller with respect to the cosine component in the case of the hydrogen. Probably it is due to the fact that the two photon exchange asymmetry in the background of the deuterium data is smaller than that of the hydrogen data and therefore the unknown oscillations are more visible in the deuterium data.

An analysis has been carried out of the asymmetry in the $\Delta(1232)$ resonance region at forward angles. Some modulations are observed in this case, see figures ?? and 6.16. Some theoretical calculations are being done to investigate the azimuthal dependences in the $\Delta(1232)$ resonance production.

On the other hand, the asymmetry in the luminosity monitors, which presents also an azimuthal modulation due to the two photon exchange physics in the Møller scattering shows no evidence of this kind of modulation we are investigating. The luminosity monitors show, though, unexpected behaviours in the direction of the spin of the beam electrons. The results of the analysis of the transverse spin asymmetry in the Møller scattering cross section show that there is a non-zero phase in the $\cos\phi$ fit function. This phase probably corresponds to the fact that the spin of the polarized beam electrons is not contained in the plane of the accelerator but it forms a small angle with respect to this plane.

We can measure the spin of the electrons through the analysis of the asymmetry in the luminosity monitors in the longitudinal data. The spin direction is not completely longitudinal but it has a small component in the transverse direction. When the GVZ half wave plate is introduced the spin direction should be reversed.
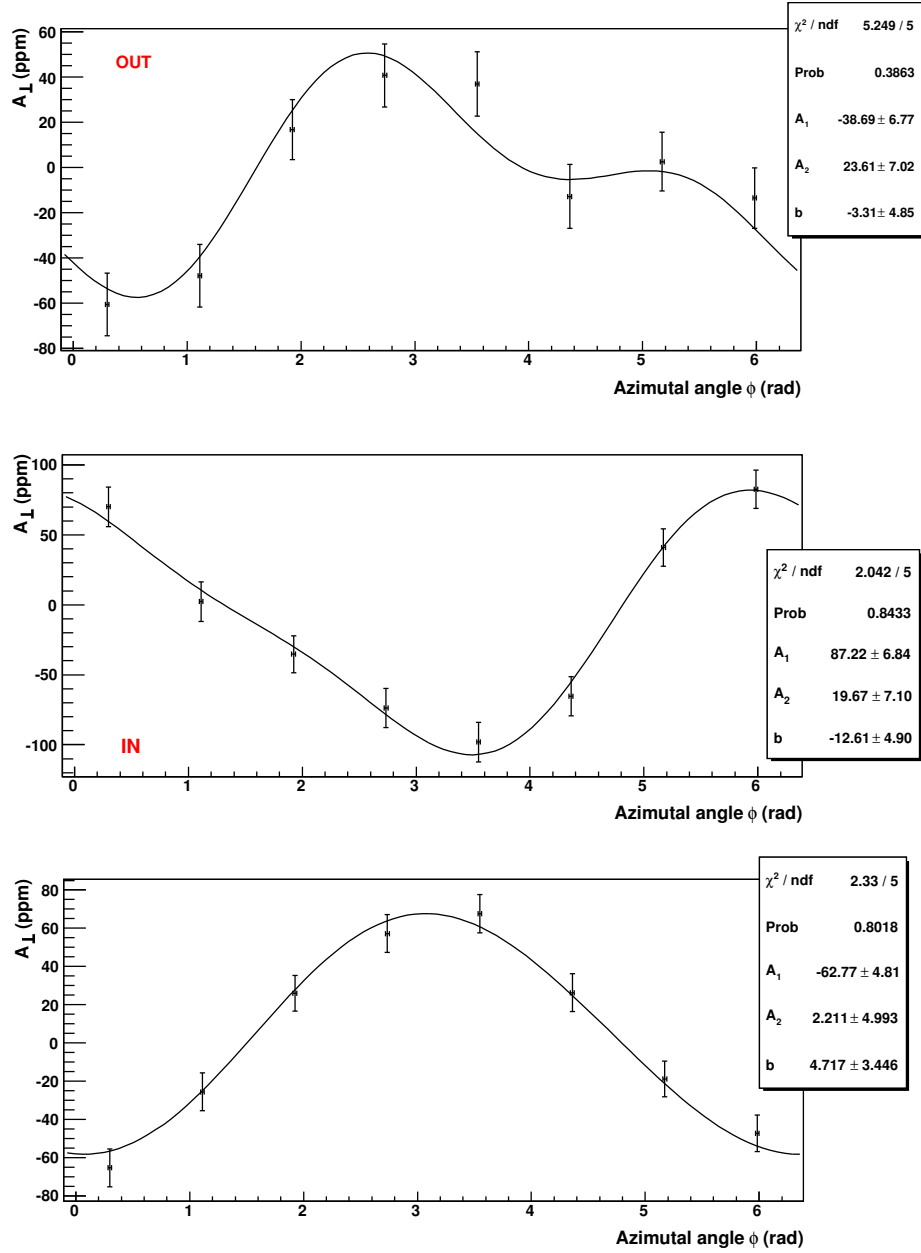
Figure 6.14. The results of the analysis of the transverse spin asymmetry in the noncoincidence spectrum for the H_2 [11] are shown. From top to bottom the data corresponding to GVZ=OUT, the GVZ=IN data and the data for the GVZ samples combined. The separated GVZ samples exhibit the sine azimuthal modulation. The amplitudes of the sine are of compatible magnitude and the amplitude of the cosine are of different magnitude but the signs are the expected. The sine terms cancel out when the GVZ samples are combined so that the asymmetry azimuthal modulation goes with the $\cos\phi$ as in the case of deuterium.
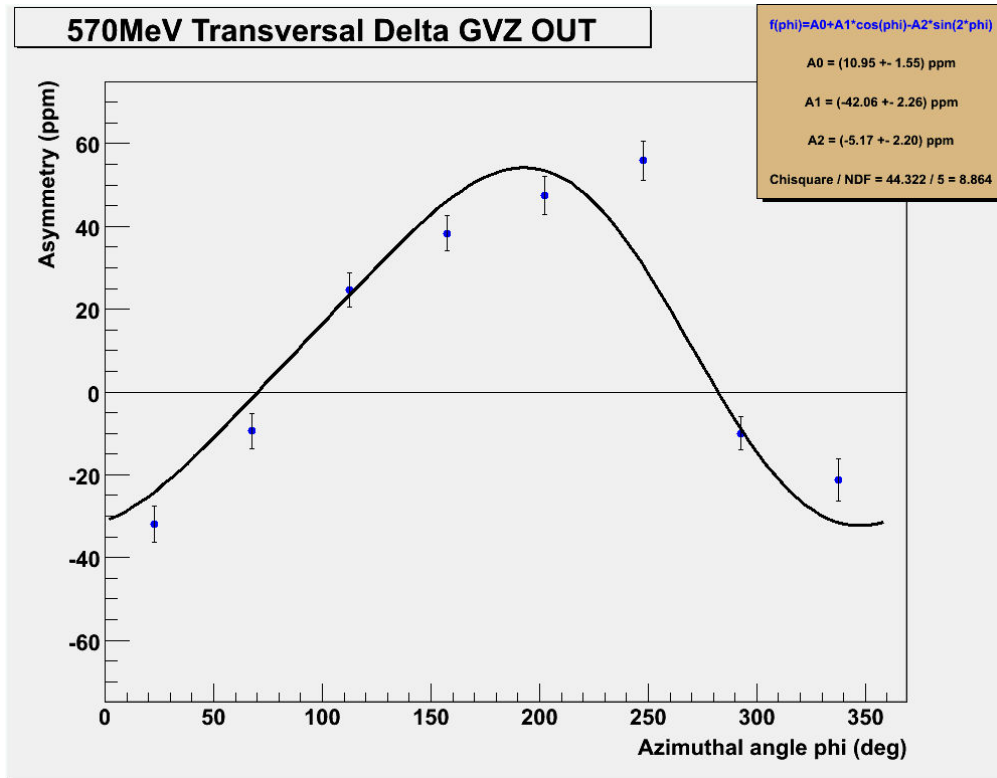
Figure 6.15. Transverse spin asymmetry for the for the Δ (1232) resonance at forward angles and energy of 570 MeV calculated separately for the samples with GVZ=OUT [11].
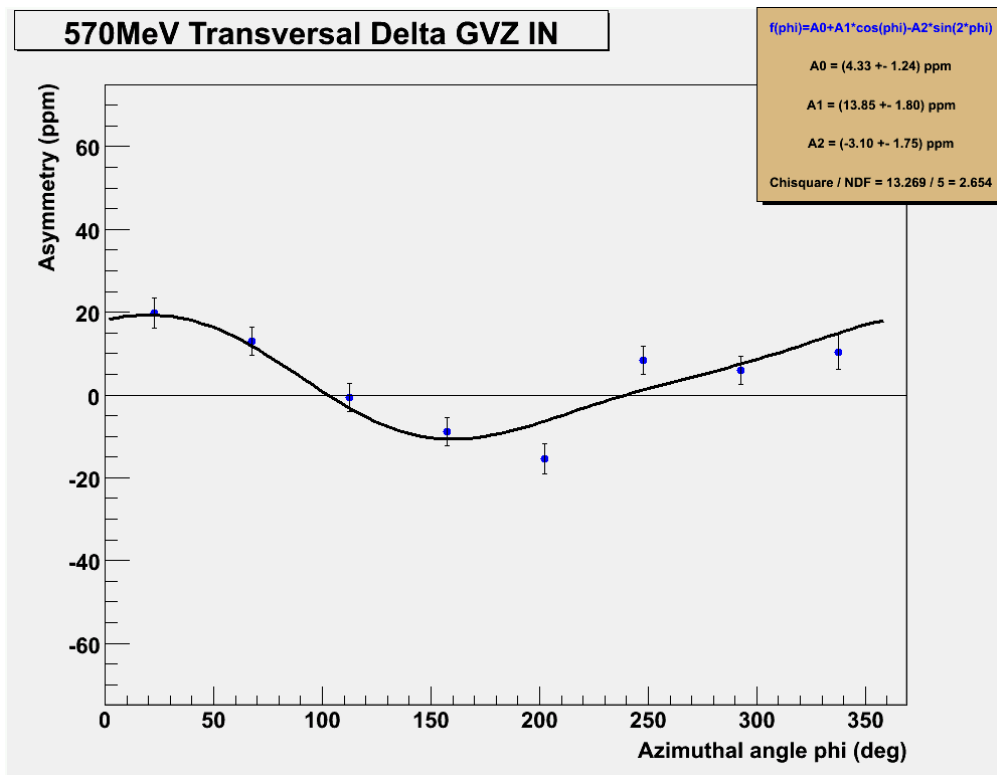
Figure 6.16. Transverse spin asymmetry for the for the Δ (1232) resonance at forward angles and energy of 570 MeV calculated separately for the samples with GVZ=IN [11].

We have observed, though, that only the longitudinal component of the spin is reversed with the introduction of the GVZ while, on the other hand, the transverse component of the spin is not reversed.

We can suspect, therefore, that the GVZ half-wave plate is not reversing the spin direction as it is supposed to do. Even we can wonder if any azimuthal modulation can arise from a fail of the Pockel cell in the fast reversing of the spin direction.

Nevertheless this effects would lead to a damping effect of the asymmetry but we can not see how these deviations can lead to azimuthal modulations. This hypothesis can not explain, though, why there is no effect in the signal of the calorimeter detector or in the luminosity monitors.

The azimuthal modulation for the separated GVZ samples in the signal is very small. The modulation do not disappear if we add the coincidence spectrum and the noncoincidence spectrum, that is, if we consider the energy spectrum provided by the calorimeter without intervention of the scintillators. This fact eliminates the hypothesis of a systematic effect originated in the plastic scintillators.

The turn corresponds to the theory to investigate with detail the azimuthal dependences in the electroproduction of pions or in the excitation of the $\Delta(1232)$ resonance. We must keep in mind, though, that we are searching for azimuthal dependences in spin asymmetries. Some experimental tests are also planned for the next beamtimes. One idea is making the slow reversing of the spin, not using the GVZ half-wave plate as usual, but by means of a shift in the energy of the beam, since the spin direction, if the Wien filter is untouched, changes with the energy of the beam an approximate amount of $45°$ per each MeV.

Chapter 7

Transverse spin asymmetry in the luminosity monitors

In the A4 collaboration experiment the luminosity is measured by means of eight luminosity monitors placed at small forward angles, covering the range $4° - 10°$ of the scattering angle. They are optimized to detect the electrons that suffer Møller scattering. This process, the scattering of a beam electron off an atomic electron, presents also, if the beam is transversely polarized, a transverse spin asymmetry due to the two photon exchange at leading order. This asymmetry can be calculated completely in the frame of QED and it is expected to be of the order of tens of ppm, that is, comparable to the transverse spin asymmetry of the elastic scattering off nucleons. This transverse spin asymmetry in the Møller scattering exhibits also a modulation in the azimuthal angle given by $\cos\phi$. In this chapter we will use the asymmetry in the luminosity to measure the transverse spin asymmetry in the cross section of the Møller scattering. Comparison of the observed asymmetry in the Møller scattering with the value predicted by the QED calculations can be used as a systematic check. This is useful for the PbF_2 data analysis since the count rates are corrected from false asymmetries in the luminosity. The measurement of the asymmetry in the Møller scattering cross section through the luminosity signal is possible because the beam current asymmetry can be separated and the target density fluctuations are strongly suppressed as we will discuss below. The luminosity monitors measure the luminosity for both opposite polarization states, L^+ and L^-, the asymmetry in the luminosity is then:

$$A_L = \frac{L^+ - L^-}{L^+ + L^-} \tag{7.1}$$

The asymmetry in the luminosity is originated by the asymmetry in the beam current intensity and the helicity correlated asymmetries in the target density fluctuations. Moreover for transverse spin data the asymmetry in the Møller scat-

tering, proportional to $\cos\phi$, also contributes to the asymmetry in the luminosity signal.

The asymmetry in the beam current, measured by the beam current intensity monitor PIMO27, can be separated from the asymmetry in the luminosity signal. For that purpose, instead of using the asymmetry in the measured luminosity the asymmetry in the luminosity normalized to the beam current will be used

$$A_{L/I} = \frac{L^+/I^+ - L^-/I^-}{L^+/I^+ + L^-/I^-} \tag{7.2}$$

This expression can be separated into the asymmetry of the measured luminosity and the asymmetry of the beam current intensity [3]

$$A_{L/I} = \frac{L^+/I^+ - L^-/I^-}{L^+/I^+ + L^-/I^-} = \frac{A_L - A_I}{1 - A_L \cdot A_I} \tag{7.3}$$

If both asymmetries are small this expression can be approximated by

$$A_{L/I} \approx A_L - A_I \tag{7.4}$$

On the other hand the target density fluctuations have been reduced with the target cooling system used by the A4 collaboration [22]. The fluctuations in the luminosity signal follow basically the fluctuations of the beam current intensity, that is, the current fluctuations are the dominant and the influence of the target density fluctuations is negligible. This suppression of the target density fluctuations allows a reliable measurement of the asymmetry in the cross section of the Møller scattering by using the asymmetry in the measured luminosity.

The helicity correlated differences in the beam parameters lead also to false asymmetries that distort and shift the asymmetry in the Møller scattering. The multilinear regression method, explained in 5.5.2 and the appendix A, to correct for the false asymmetries is also applied to correct the asymmetry in the luminosity from the false asymmetries. We expect the fit parameters, that is, the false asymmetries per unit X_i, to be different because they are trivial asymmetries in the cross section of a different physical process, the Møller scattering, and they correspond to different kinematic conditions, that is, small forward angles.

We applied first the multilinear regression method to the eight monitors separately. In the table below we can see the results for the fit parameters for one monitor.

X^j	$a_j \pm \sigma(a_j)$
A_I (ppm)	-0.35 ± 0.05
Δx (μm)	31 ± 18
Δy (μm)	15 ± 62
$\Delta\alpha$ (μdeg)	-4.6 ± 2.7
$\Delta\beta$ (μdeg)	-0.42 ± 5.72
ΔE (eV)	0.012 ± 0.047

The fit parameters of the current asymmetry is known with quite high precision. The errors of the fit parameters corresponding to the beam position and angle differences are large as these beam parameters present large correlations. The most remarkable result is the fit parameter associated to the beam current asymmetry. From the equation 7.4 we expect a beam current coefficient around -1. The experimentally observed fit parameter has the correct sign but is smaller in magnitude than expected. Similar results are obtained for the other monitors.

The table below shows the luminosity asymmetry normalized to the beam current intensity and corrected from the false asymmetries. The asymmetries in the luminosity signal for the eight luminosity monitors calculated for the separate GVZ samples are shown in the figures 7.2 and 7.3.

Sector	$A^{Ph}_{correct}(10^{-6})$
1	-21.73 ± 0.20
2	-8.54 ± 0.38
3	7.84 ± 0.65
4	18.06 ± 0.51
5	17.63 ± 0.35
6	8.28 ± 0.19
7	-9.10 ± 0.74
8	-19.65 ± 0.11

The analysis has been also performed for the asymmetry in the luminosity averaged over the eight sectors. This asymmetry should average out. Moreover we expect the fit parameters corresponding to the beam position and angle differences to average out when the eight luminosity monitors, and therefore the whole azimuthal angle, are considered. In the table below we show the results of the multilinear regression analysis applied to the average of the asymmetry in the luminosity over the eight monitors.

X^j	$a_j \pm \sigma(a_j)$
A_I (ppm)	-0.44 ± 0.07
Δx (μm)	-8 ± 23
Δy (μm)	-47 ± 79
$\Delta\alpha$ (μdeg)	-0.4 ± 3.4
$\Delta\beta$ (μdeg)	4 ± 7
ΔE (eV)	-0.09 ± 0.06

The fit parameters associated with the beam position and angle differences are compatible with zero as it is expected. Again the fit parameter of the beam current asymmetry is about one half of the expected value.

Below we show the result of the asymmetry averaged: the raw asymmetry at the left, the corrected asymmetry in the middle. We see in both cases that the

averaged asymmetry in the luminosity is not compatible with zero. The average asymmetry is small though.

$A_{raw}^{Ph}(10^{-6})$	$A_{correct}^{Ph}(10^{-6})$	δ_A^{syst}
0.67 ± 0.13	0.88 ± 0.14	0.04

The discrepancy of the fit parameter associated to the beam current asymmetry with respect to the expected value of about -1 is probably explained by the nonlinearity of the luminosity measurement. We know how to correct the nonlinearity in the luminosity signal [22]. The luminosity signal is plotted versus the rate of the PbF_2 calorimeter because both detectors see the same luminosity and the calorimeter answer is assumed to be linear because dead time losses are very small. A tanh fit functions turns out to be useful to correct the nonlinearity in the luminosity signal (see figure 7.1). Nevertheless the correction of the luminosity has not been performed yet for the backward data. Since the nonlinearities of the individual monitors are different, the lack of correction might also explain why in the averaged luminosity there is still an asymmetry not compatible with zero. This fact might also introduce a false asymmetry to the data from the PbF_2 calorimeter when the count rates are normalized to the luminosity. But, as we can see here, the impact is rather small, 0.88 ppm, compared to 40 ppm.

The asymmetry in the luminosity monitors when GVZ samples are combined and corrected from the false asymmetries is given by:

$$A_{\perp}^{LuMo} = (-20.81 \pm 0.12_{stat} \pm 0.05_{syst})\text{ppm}$$

We now present the result of the calculation of the two photon exchange asymmetry in the Møller scattering for the energy 315.1 MeV. The value calculated is the average over the angle range $4° - 10°$. The details of the calculation can be found in [3]. The calculated value of the asymmetry is:

$$A_{\perp}^{Møller} = -56.89\text{ppm}$$

We observe a discrepancy between the measured and the calculated values of the Møller asymmetry that is about a factor of 2.7. The most probable cause of this discrepancy is the nonlinearity of the luminosity signal which has not been corrected yet. The factor 2.7 of difference between the calculated and the measured values of the Møller asymmetry is consistent with the factor 2 of discrepancy we have found between the expected value of the beam current false asymmetry ~ -1 and the value obtained in the regression ~ -0.5.
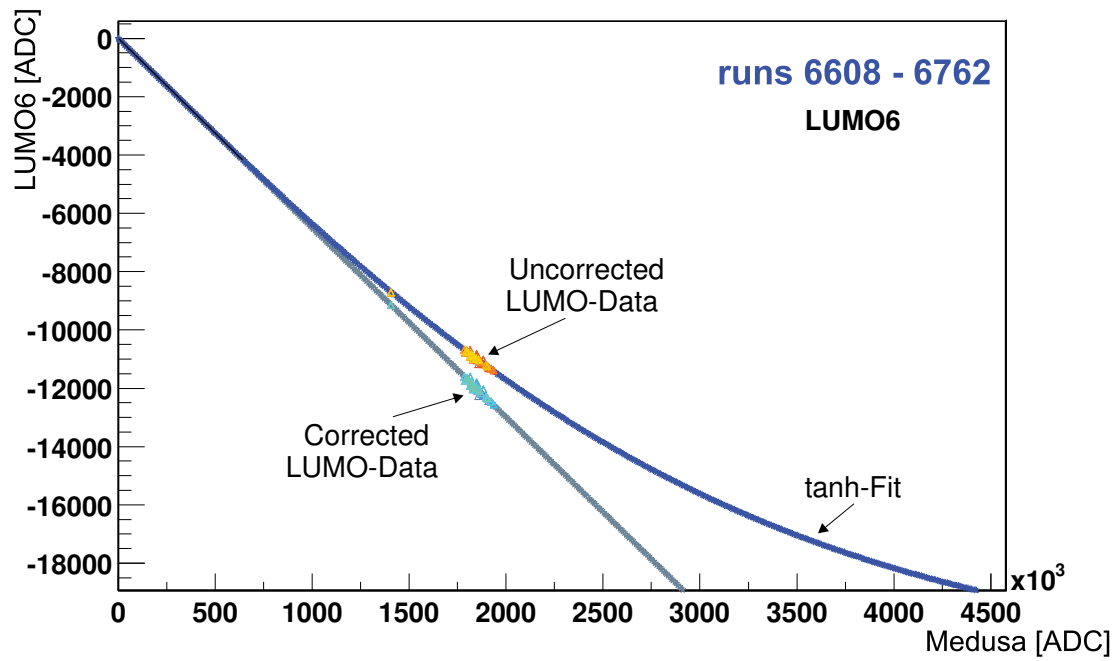
Figure 7.1. The figure taken from [22] shows the plot of the luminosity signal versus the Medusa rate as both detectors see the same luminosity and the calorimeter is assumed to be linear. The nonlinearity in the luminosity signal can be corrected through a hyperbolic tangent.
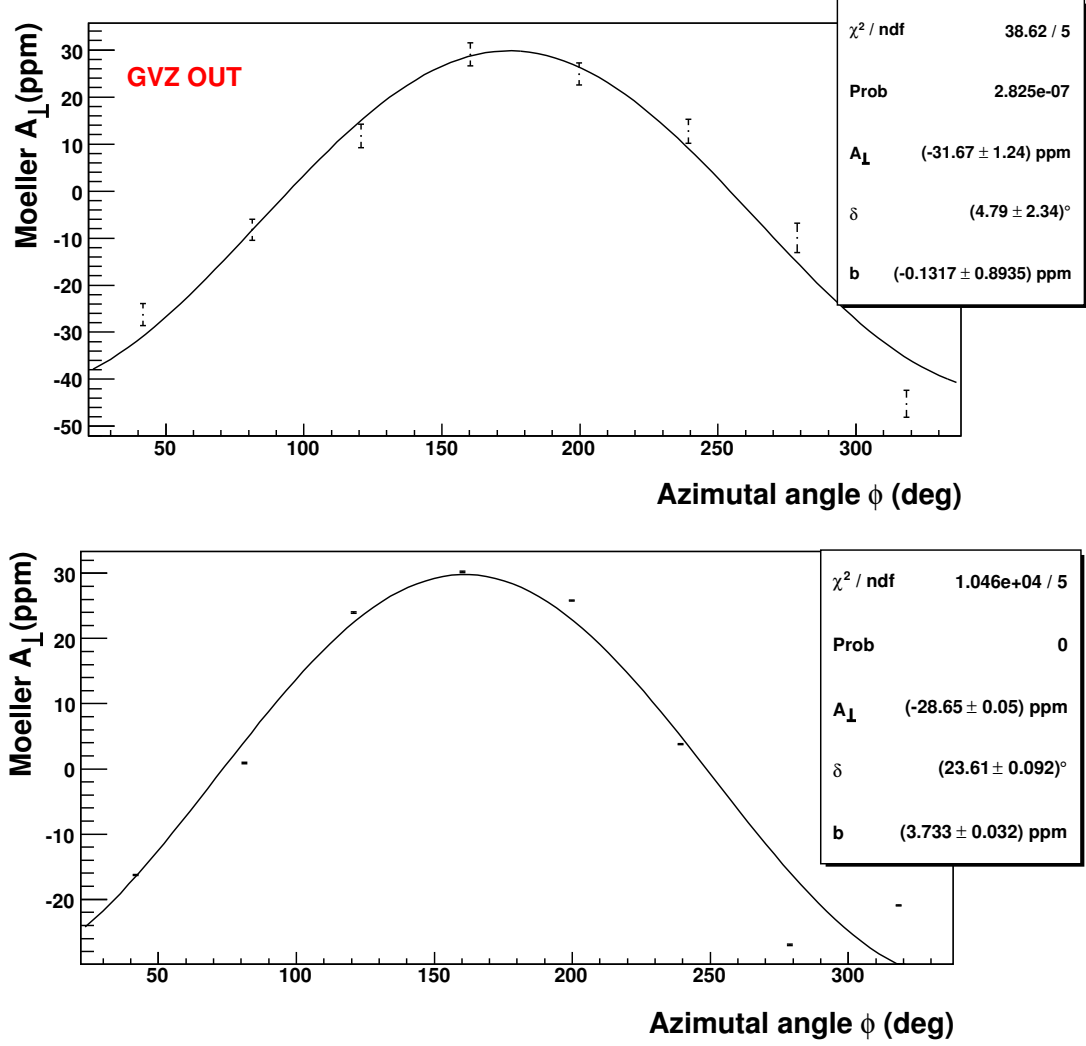
Fit function: $A(\phi) = A_\perp \cos(\phi + \delta) + \mathfrak{b}$

(7.5)

Figure 7.2. The upper figure shows the asymmetry in the luminosity corrected from the false asymmetries and the lower figure shows the raw data. This data corresponds to the samples with the GVZ half-wave plate OUT. The sign of the asymmetries is the correct one. We observe the following features: the asymmetry in the luminosity is very sensitive to the helicity correlated changes of the beam parameters. It is remarkable that the fit to the raw data presents a very large phase. The phase of the corrected data is smaller but not compatible with zero.

Fit function: $A(\phi) = A_\perp \cos(\phi + \delta) + \mathfrak{b}$

(7.6)

χ^2 / ndf	12.49 / 5
Prob	0.02866
$A_\perp$	(32.11 ± 1.94) ppm
δ	$(4.38 \pm 3.36)°$
b	(-5.885 ± 1.363)

GVZ IN

χ^2 / ndf	1.444e+04 / 5
Prob	0
$A_\perp$	(19.31 ± 0.05) ppm
δ	$-40.80 \pm 0.17)°$
b	(3.625 ± 0.039) ppm
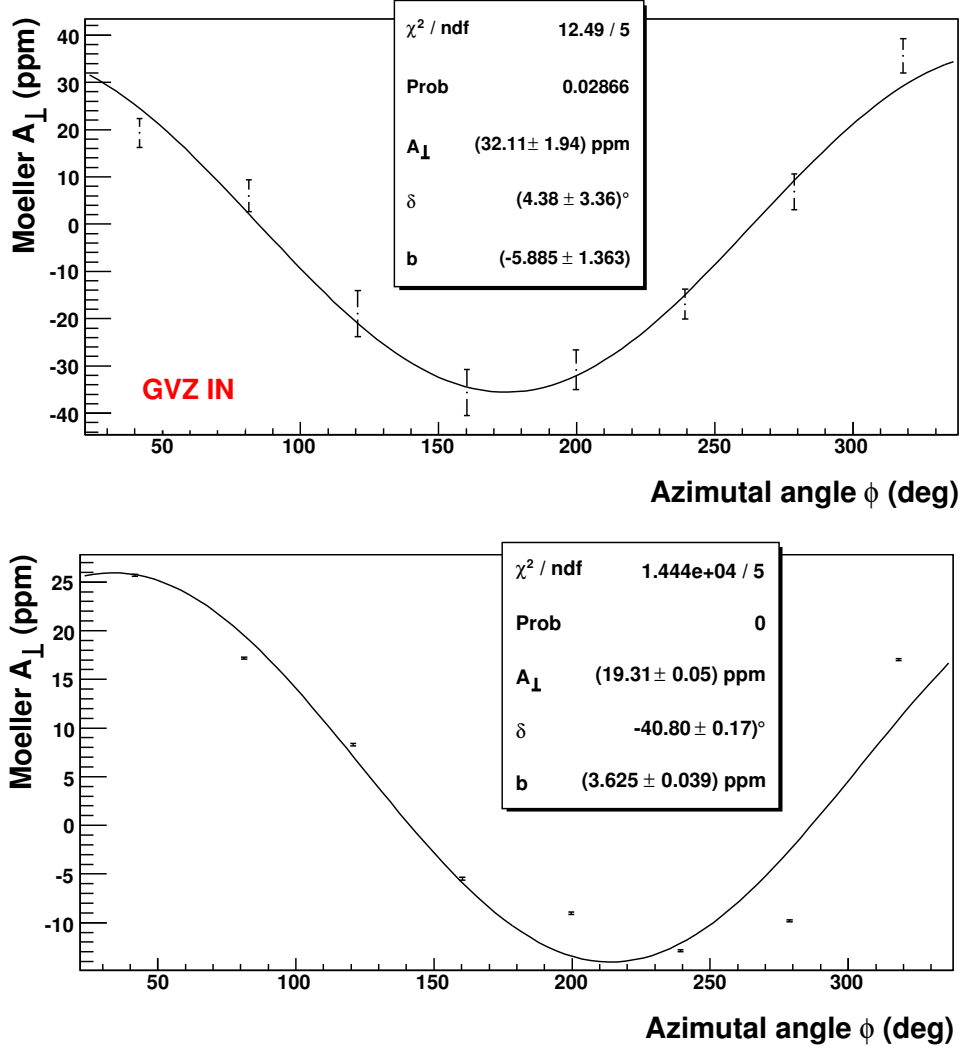
Figure 7.3. The upper figure shows the asymmetry in the luminosity normalized to the beam current and corrected from the false asymmetries. The lower figure shows the raw data. These data correspond to the samples with the GVZ half-wave plate IN. The data presents the correct sign, the opposite to the OUT samples. The most remarkable is that the fit to the raw data presents a large phase that is of similar magnitude to that exhibited by the OUT data but with opposite sign.

Chapter 8

Conclusion and outlook

We have seen throughout this work that one of the most important challenges of the analysis at backward angles is how to cope with the neutral background present in the coincidence spectrum. This difficulty is especially acute for the deuterium data because the amount of background is larger. The Monte Carlo simulations of the experimentally observed energy spectra is the tool used by the A4 collaboration to separate the true quasielastic events from the background. The objective of this work has been testing a simple model based in the simulation of the response of the detectors to the neutral background, since the simulation for the deuterium at backward angles is not yet available. This simple model allows an understanding of the source of the systematic errors of the asymmetry. We have learnt from the model that the statistical error of the asymmetry is not any more given by $1/\sqrt{N_{true}}$, where N_{true} is the number of true events, because to calculate the asymmetry in the quasielastic scattering we must do a subtraction of the number of counts of two different histograms and the errors are additive. Another dominant source of the systematic error is the dependence of the noncoincidence asymmetry on the lower cut in energy. Of the two parameters of the model, the scaling factor ϵ and the shift in energy δ, the error in the asymmetry is much more sensitive to uncertainties in the δ.

We have tested two procedures for the application of the model: (1) The applying cut method and (2) the weighted procedure. With the second method we have obtained a slightly smaller statistical error for the mean asymmetry. The first method has taught us that there is an optimum lower cut that leads to a relative minimum in the asymmetry error. Nevertheless we have faced also the insufficiency of the model because there is a systematic drifting of the asymmetry depending on the lower cut that is larger than the error bars.

We have applied the multilinear regression method to correct the false asymmetries due to the beam parameters. It is evident that the corrections from the false asymmetries are rather small. The quality of the beam has substantially improved

with respect to past beamtimes so that the false asymmetries are smaller than before but at the same time the knowledge of the false asymmetries is worse. The multilinear regression method is, though, still useful to estimate the systematic error due to the false asymmetries.

On the other hand, the analysis of the asymmetry in the noncoincidence spectrums has led to the discovery of unexplained azimuthal modulations of the asymmetry in the background that arise when GVZ samples are analysed separately and cancel out if the GVZ samples are combined. A function of the azimuthal angle that includes not only the ever expected $\cos\phi$ but also a $\sin 2\phi$ fits quite well to the data. Nevertheless the analysis of the fit of this function to the asymmetry in function of the lower cut reveals even more unknowns. The unexpected modulations are present only in the asymmetry of the background, not in the asymmetry of the signal and these modulations are not exclusive of the deuterium data or the transverse spin data but they belong as well to the hydrogen data and to the longitudinal asymmetries. Efforts to find an explanation of the unexpected modulations is nowadays a priority of the A4 collaboration.

We have presented also the analysis of the transverse spin asymmetry in the luminosity monitors. The asymmetry exhibits the expected cosine azimuthal modulation. There is no evidence of the modulations that we observe at the asymmetry in the noncoincidence spectrum in the calorimeter. We have observed, though, a non-zero phase in the fit of the cosine that we interpret as a deviation of the spin orientation of the beam electrons from the plane of the accelerator. In addition, the discrepancy between the measured value of the asymmetry in the Møller scattering and the theoretically calculated with the two photon exchange is probably due to the lack of correction for the nonlinearity in the luminosity signal. The lack of correction of the nonlinearity has, though, a no important effect on the asymmetry measurement at the calorimeter.

An open question for the deuterium data is how to combine the information extracted with the deuterium and that extracted with the hydrogen to isolate the relevant information for the neutron. A model calculation [10] provides theoretical predictions of the two photon exchange contribution to the transverse spin asymmetry for both the proton and the neutron. However there is no yet a model calculation that takes into account the nuclear models for the deuteron. If we use the static approximation and combine the predictions for the free proton and neutron we arrive to a clear contradiction between the asymmetry predicted by the model and the measured asymmetry. As both the neutron and proton asymmetries given by the model are of similar magnitude but opposite sign we expect, according to the static approximation, a cancellation in the deuterium. Nevertheless the asymmetry measured is in the order of $40-50$ ppm while the asymmetry measured with the hydrogen for the free proton is of about 100 ppm.

In the future the task of the theory should be to unravel the information for the neutron from the deuterium transverse spin asymmetry with a careful inspection on the nuclear model dependencies. The A4 collaboration continues with the program of measurements of the transverse spin asymmetry with both deuterium and hydrogen since the experimental information concerning the two photon exchange amplitudes is still scarce [1]. Data taking for the measurement of the transverse spin asymmetry with hydrogen target at backward angles has been already carried out at the energy of 420 MeV. A beamtime for the transverse spin at the same configuration and energy and with deuterium is programmed for June. In the future it is programmed to rearrange the detector to perform forward measurements again. The measurement of the transverse spin asymmetry with both hydrogen and deuterium at higher energies is included in the program.

Appendix A

Multilinear regression method

The relation 5.52 holds actually for the true values of the asymmetries. The measured asymmetries in each single run present fluctuations with respect to some mean value. The single asymmetry measurements follow a Gauss distribution whose mean belongs to the straight line defined by 5.52. Therefore the particular measurements of the asymmetry can be expressed as the sum of the corresponding mean and some deviation that is gaussian distributed, that is:

$$X_0^j = P \cdot A_0 + \sum_{i=1}^{6} a_i X_i^j + \epsilon^j \tag{A.1}$$

where X_0^j is a single measurement of the raw asymmetry for the run j, the first two terms of the right side represent the mean and the ϵ^j is the deviation of the raw measurement X_0^j with respect to the mean located in the straight line.

As the beam parameter differences X_i in each single run are spread out over some wide range the multilinear regression analysis is applied to obtain an estimation of the straight line coefficients a_i that give the false asymmetry per unit X_i. Then we can extrapolate the value of the measured asymmetry to the origin of coordinates where the beam parameter differences would be zero. This point corresponds to zero false asymmetries and therefore gives the physical asymmetry (times the degree of polarization).

Let us rewrite A.1 in a more convenient way. If the mean of the raw asymmetries corresponding to different beam conditions is taken and also the mean of the beam parameters the mean of the deviations $\bar{\epsilon}$ should be zero, as the deviations ϵ^j are assumed to be symmetrically distributed around the straight line.

$$\overline{X}_0 = P \cdot A_0 + \sum_{i=1}^{N} a_i \overline{X}_i + \overline{\epsilon} \tag{A.2}$$

where $\bar{\epsilon} = 0$. Subtracting the equation A.2 from A.1 it is obtained

$$X_0^j - \overline{X}_0 = \sum_{i=1}^{i=N} a_i(X_i^j - \overline{X}_i) + \epsilon^j \tag{A.3}$$

Least squares method   According to the maximum likelihood method the best estimates of the straight line coefficients a_i for a particular sample of measurements are those that maximize the probability of obtaining that set of measurements.

The probability of obtaining a particular value of the asymmetry X_0^j in one measurement is given by the Gauss probability distribution function

$$P(X_0^i) = \frac{1}{\sqrt{2\pi}\sigma} \exp\left\{ -\frac{\epsilon_i^2}{2\sigma_i^2} \right\} \tag{A.4}$$

As the measurements are independent the probability to obtain a particular set of measurements equals the product of the individual probabilities.

$$P(X_0^1, X_0^2, \ldots, X_0^N) = \prod_{i=1}^{N} \frac{1}{\sqrt{2\pi}\sigma_i} \exp\left\{ -\frac{\epsilon_i^2}{2\sigma_i^2} \right\} \tag{A.5}$$

The maximization of the probability is equivalent to the minimization of the exponent.

$$\chi^2 = \sum_{i=1}^{N} \frac{1}{\sigma_i^2} \left[(X_0^i - \overline{X_0}) - \sum_{j=1}^{6} a_j(X_j^i - \overline{X}_j) \right]^2 \tag{A.6}$$

The particular values of the fit parameters a_i^0 that minimize the χ^2 are those such that the partial derivatives of χ^2 with respect to the fit parameters a_i are zero:

$$\left.\frac{\partial \chi^2}{\partial a_i}\right|_{a_i^0} = 0 \qquad i = 1, \ldots, 6 \tag{A.7}$$

System of linear equations   This methods leads finally to a system of 6 linear equations with 6 unknowns (the fit parameters) and whose coefficients are the correlations between the beam parameters.

$$s_{j0}^2 = \sum_{k=1}^{6} a^k s_{jk}^2 \tag{A.8}$$

where

$$s_{jk}^2 = \frac{1}{N-1} \sum_{i=1}^{N} \left[(X_i^j - \overline{X}^j)(X_i^k - \overline{X}^k) \right] \tag{A.9}$$

With the definitions

$$r_{jk} = \frac{s_{jk}^2}{s_{jj}s_{kk}} \tag{A.10}$$

$$b_j = a_j \frac{s_{jj}}{s_{00}} \tag{A.11}$$

where r_{jk} are the covariances between the beam parameters defined in terms of the correlations,

the system of equations A.9 can be written in terms of the covariances r_{jk}

$$r_{j0} = \sum_{k=1}^{6} b^k r_{jk} \tag{A.12}$$

Physical asymmetry The fit parameters can be obtained solving the equation A.12 by inverting the covariances matrix

$$b^k = \sum_{k=1}^{6} r_{jk}^{-1} r_{j0} \tag{A.13}$$

$$a_j = b_j \frac{s_{00}}{s_{jj}} \tag{A.14}$$

The fit parameters are used to subtract the false asymmetries from the measured asymmetry.

$$P \cdot A_{ph} = \frac{1}{N} \sum_{i=1}^{N} \left(X_i^0 - \sum_{j=1}^{6} a_j X_i^j \right) \tag{A.15}$$

List of Figures

Bibliography

[1] MAAS, F. et al.: *Measurement of the transverse beam spin asymmetry in the elastic electron proton scattering and the inelastic contribution to the imaginary part of the two photon exchange amplitude* arXiv:nucl-ex/0410013 (2004)

[2] MARTIN, Alan D.: *Quarks and Leptons: An Introductory Course in Modern Particle Physics* John Wiley and Sons, New York, 1984

[3] BAUNACK, S.: *Einzelspin-Asymmetrien in der elastischen Elektron-Proton-Streuung und die Beitrge der Strange-Quarks zu den Formfaktoren des Nukleons* Mainz, Joh. Gutenberg-Universitt, Institut fr Kernphysik, Doctoral Thesis, January 2005

[4] BAUNACK, S.: *Private comunication*

[5] GUICHON, P.A.M. and Vanderhaeghen, M.: *How to reconcile the Rosenbluth and the polarization transfer methods in the measurement of the proton form factors* arXiv:hep-ph/0306007 (2003)

[6] GUICHON, P.A.M. and Vanderhaeghen, M.: *Beam normal spin asymmetry in elastic lepton-nucleon scattering* Phys. Rev. Lett. 91, 142303 (2003)

[7] BLUNDEN, P.G. et al.: *Two-photon exchange and elastic electron-proton scattering* arXiv:nucl-th/0306076 (2003)

[8] DE RÚJULA, A. et all: *Elastic scattering of electron from polarized protons and inelastic electron scattering experiments* Nucl.Phys.B35, 365-389 (1971)

[9] SÁNCHEZ LORENTE, A.: *Messung der Asymmetrie in der elastischen Streuung transversal polarisierter Elelektronen an unpolarisierten Protonen* Mainz, Joh. Gutenberg-Universitt, Institut fr Kernphysik, Diploma Thesis, Januar 2003

[10] PASQUINI, B. and Vanderhaeghen, M.: *Resonance estimates for single spin asymmetries in elastic electron-nucleon scattering* Physical Review C 70, 045206 (2004)

[11] MAMI/A4 Baunack, S. et al.   (unpublished).

[12] Benhar, O. et all: *Quasi-elastic electron-nucleus scattering*   arXiv:nucl-ex/0603029 (2006)

[13] von Harrach, D.:   *Kinematics of Electron-Deuteron Scattering.* Private comunication, May 31, 2007

[14] Taber de Forest, JR.:   *Off-shell electron-nucleon cross sections. The impulse approximation* Nuclear Physics A392 232-248 (1983)

[15] Hadjimichael, E. et al.: *Parity-violating asymmetry in the quasielastic $e-d$ scattering* Physical Review C, volume 45, number 6 (june 1992)

[16] Aulenbacher, K.: *Helicity correlated asymmetres caused by optical imperfections* Eur. Phys. J. A 32, (2007) 543-547

[17] Backe, H et al: *Prospekt des Instituts für Kernphysik.* Review of particle physics(2006)

[18] Blunden, V. et al.: *Precession of the polarization of particles moving in a homogeneus electromagnetic field* Physical Review Letters 2, (1959) p.455

[19] Tioukine, V. and Aulenbacher, K.: *Operation of the MAMI accelerator with a Wien filter based spin rotator system* Nucl. Intr. and Meth A, 568 (2006) 537-542

[20] Particle Data Group: *Reviews, Tables, and Plots.* Review of particle physics(2006)

[21] Altarev, I. and Schilling, E. et al.: *A high power liquid hydrogen target for the Mainz A4 parity violation experiment* arXiv:nucl-ex/0504024, (2005)

[22] Hammel, T. et al.: *A luminosity monitor for the A4 parity violation experiment at Mainz.* Joh. Gutenberg-Universitt, Institut fr Kernphysik, Doctoral Thesis in preparation.

[23] Boris, G.: *A luminosity monitor for the A4 parity violation experiment at Mainz.* Nucl. Instrum. Meth. A564:1-12 (2006)

[24] Achenbach, P.:   *Aufbau eines Bleifluorid-Kalorimeters zur Messung der Parittsverletzung in der elastischen Elektronenstreuung*   Mainz, Joh. Gutenberg-Universitt, Institut fr Kernphysik, Doctoral Thesis, January 2001

[25] KOTHE, R.: *Aufbau und Betrieb einer schnellen Kalorimeterelektronik fr ein Experiment zur Messung der Parittsverletzung in der elastischen Elektronenstreuung* Mainz, Joh. Gutenberg-Universitt, Institut fr Kernphysik, Doctoral Thesis, January 2008

[26] LUIGI, C.: *Investigations on the response of the A4 calorimeter in the region of the $\Delta(1232)$ resonance using Monte Carlo simulations.* Mainz, Joh. Gutenberg-Universitt, Institut fr Kernphysik, Dissertation, Januar 2005

[27] CAPOZZA, L.: *Simulation der experimentellen Spektren zur Messung der Parittsverletzung in der elastischen Elektronenstreuung.* Mainz, Joh. Gutenberg-Universitt, Institut fr Kernphysik, Doctoral Thesis in preparation.

[28] LEO, William R.: *Techniques for nuclear and particle physics experiments* Springer-Verlag, Heidelberg, 1987

[29] LUIGI: . Private comunication

[30] NIST: National Institutes of Standards and Technology *ESTAR program: stopping-power and range tables for electrons* http://physics.nist.gov/PhysRefData/Star/Text/ESTAR.html (accesed April 15,2008)

[31] FRIEDRICH, J. and Walcher, TH.: *A coherent interpretation of the form factors of the nucleon in terms of a pion cloud and constituent quarks* arXiv:hep-ph/0303054 (2003)

[32] BEVINGTON, P.: *Data reduction and error analysis for the physical sciences* McGraw-Hill, New York, 1960

Acknowledgments

I appreciate the opportunity Prof. v. Harrach gave me to work in the A4 experiment. It has been truly a pleasure to work in this group among so pleasant people, acquiring valuable knowledge about this fascinating world of the nuclear physics experiments. I thank my supervisor Sebastian Baunack for the wise guidance he has gave me during this year, for his human quality and his great sense of humor. Thanks to Luigi I have understood a lot of aspects of the experiment and the theory. I owe him a great fraction of what I have learnt. Yoshio, Jürgen and Jeonghan have been kind, helpful, nobles and a very good company. I really appreciate the time you spend in solving our problems with computers. An especial mention deserves the friendly conversations with Jeonghan during the work at night and the valuable gift. Boris, Rainer, Mamen, Cristoph Frank and Ernst have been kind, helpful and patient with me.

Thank you very much A4.

Hhhhhhhh